FEASIBILITY STUDY OF ELECTRON INJECTION FOR TOKAMAK PLASMA TRANSPORT CONTROL

Wonho Choe

June 1996

FEASIBILITY STUDY OF ELECTRON INJECTION FOR TOKAMAK PLASMA TRANSPORT CONTROL

Wonho Choe

A DISSERTATION
PRESENTED TO THE FACULTY
OF PRINCETON UNIVERSITY
IN CANDIDACY FOR THE DEGREE
OF DOCTOR OF PHILOSOPHY

RECOMMENDED FOR ACCEPTANCE
BY THE DEPARTMENT OF ASTROPHYSICAL
SCIENCES

June 1996

©Copyright by Wonho Choe, 1995. All rights reserved.

To Sekyung, Daray, and my parents

Abstract

Recent experimental and theoretical research has revealed that radial electric fields (E_r) play a crucial role in the tokamak plasma transition into an improved confinement regime. Motivated by these results, two novel techniques utilizing injection of hot electrons were developed and tested in this research. The objective is to control the transition to H-modes in large scale future devices by inducing E_r via external means.

The electron ripple injection (ERI) technique has been developed on CDX-U to fulfill this in a non-intrusive way. This technique utilizes externally provided local magnetic field ripple and electron cyclotron resonance heating (ECRH) to trap edge electrons and to cause them to drift towards the plasma center so that they charge up flux surfaces negatively. The temperature anisotropy of resonant electrons in a tokamak plasma was calculated to study the effects of ECRH on electrons. The behavior of energetic electrons and the generation of E_r in the presence of ripple fields were investigated using a guiding-center electron orbit code. Examples for CDX-U and ITER parameters are given.

Preliminary experiments have been performed on CDX-U. The results show the existence of drifts, and combined effects of electron trapping and heating. The electron temperature anisotropy produced by ECRH was also measured. Since both modeling and preliminary experiments gave encouraging results, further experiments are warranted.

Another novel approach has been successfully taken using electron injection: an emissive limiter biasing experiment on CCT involving an injection of hot electrons at the plasma edge from the limiter. The emissive capability appears to be important for operating at lower bias voltage ($V_{bias} \leq -150\,V$) compared to biasing a cold limiter ($V_{bias} \leq -450\,V$) for inducing H-mode transition. The results shown in this experiment suggest that the performance of the limiter or divertor bias experiments can be significantly improved by simply adding emissive capability.

Contents

Abstract iii

List of Figures ix

1 Introduction 1

1.1 Various Confinement Regimes of a Tokamak Plasma 2

1.1.1 Ohmic regime 2

1.1.2 L-mode 3

1.1.3 H-mode 3

1.1.4 Supershot regime on TFTR 4

1.1.5 PEP H-mode on JET 4

1.1.6 VH-mode on DIII-D 5

1.1.7 CH-mode on PBX-M 5

1.1.8 Internal Transport Barrier on JT-60U 5

1.2 Observation of H-mode 6

1.3 Importance of H-mode for Future Devices 9

1.4 Thesis Motivation 9

1.5 Thesis Organization and Overview 11

2 Principle of Electron Ripple Injector 13

3 Calculation of Temperature Anisotropy 27

3.1 Kinetic Calculation of Temperature Anisotropy 27

3.1.1 Coulomb collision term 32

3.1.2 Wave heating term 38

3.1.3 Loss and source terms 39

3.1.4 Evaluation of the temperature anisotropy 42

3.2 Summary 46

4 Simulation of Energetic Electron Orbits and E_r Generation 53

4.1 Energetic Electron Orbit Calculation 53

4.2 Radial Electric Field Generation 60

4.3 Summary 69

5 CDX-U Device 73

5.1 The CDX-U Device 74

5.2 2.45 *GHz* Microwave System 76

5.3 Diagnostics for Routine Plasma Parameters 81

5.4 Timing and Data Acquisition 81

6 ERI Experiment on CDX-U 83

6.1 Particle Drifts 83

6.2 Topology of a Magnetic Field Line 86

6.3 ECH and Ripple Trapping 92

6.3.1 Observation of Limiter Currents in two regions 92

6.3.2 Density in terms of temperature anisotropy and ripple strength 95

6.3.3 Experimental determination of temperature anisotropy 98

6.4 Summary 108

7 Emissive Limiter Bias Experiment on CCT 109

7.1 Description of the Experimental Setup 111

7.2 Limiter Biasing and H-mode Transition 111

7.3 Results with Emissive Limiter 116

7.4 Summary 123

8 Summary of the Thesis and Future Work 127

8.1 Summary of the Thesis 127

8.1.1 Electron Ripple Injection 127

8.1.2 Emissive Limiter Biasing 129

8.2 Suggestions for Future Work 130

Bibliography 133

Figures

2.1 Schematic of the electron ripple injector (1) 14

2.2 Schematic of the electron ripple injector (2) 15

2.3 Various ripple coil configurations considered in GOLDSTON *et al.*, 1977 18

2.4 Magnetic field lines at different radial positions ($Z = 33\,cm$) 19

2.5 3-dimensional plot of magnetic field strength (*TypeI*) 20

2.6 Contour plot of field ripple strength (*TypeI*) 21

2.7 Toroidal field coils and *TypeII* ripple coils 23

2.8 Magnetic field lines with vertically global ripple fields (*TypeII*) 24

2.9 3-dimensional plot of magnetic field strength (*TypeII*) 25

3.1 Plot of smoothed functions of bounced-averaged quantities 36

3.2 Region of λ for ripple trapping 40

3.3 Fraction of trapped electrons in the magnetic ripple fields 41

3.4 Perpendicular and parallel temperatures as a function of ν_L/ν_0 47

3.5 Temperature anisotropy with different ripple strength 48

3.6 Z_{eff} dependence of temperature anisotropy 49

3.7 Z_{eff} dependence of perpendicular and parallel temperature 50

3.8 Warm electron temperature anisotropy with various Z_{eff} 51

4.1 $n_e(r)$, $T_e(r)$, and $q(r)$ of CDX-U assumed in the numerical simulation 55

4.2 Effects of Coulomb scattering in the orbit calculation 56

4.3 Time trace of an energetic electron orbits in the presence of ripple fields (Cross-sectional view) - - - 57
4.4 Time trace of an energetic electron orbits in the presence of ripple fields (Top view) - - - 58
4.5 Radial penetration depth controlled by ripple strength and electron energy - - - 59
4.6 Algorithm for calculating E_r generated by ripple-injected electrons - - - 62
4.7 Temporal plot of E_r and rotation speed - - - 63
4.8 Saturation of E_r - - - 65
4.9 Effect of E_r on particle orbits. - - - 66
4.10 Electron orbits and E_r - - - 67
4.11 E_r with various ripple strength - - - 68
4.12 E_r with various initial electron energy - - - 71
4.13 E_r generation for ITER case - - - 72

5.1 CDX-U vessel - - - 77
5.2 CDX-U assembly - - - 78
5.3 Location of CDX-U ripple coil *TypeII* - - - 79
5.4 Schematic of ECH system - - - 80

6.1 20 *cm* cubic resonant cavity to see vertical drifts - - - 84
6.2 Vertical profile of strip currents showing the existence of vertical drifts - 85
6.3 Radial scan of Langmuir probe signal with a tungsten filament electron source. - - - 88
6.4 Vertical distribution of strip currents - - - 89
6.5 A topology of a magnetic field line - - - 90
6.6 Radial distribution of Langmuir probe signal - - - 91
6.7 Experimental setup to study ripple trapping and ECH - - - 93
6.8 Difference of limiter currents in regions *1* and *2* - - - 94

6.9 Major radial scan of electron density in *region 1* 100
6.10 Total density ratio in two regions at various ripple strengths 101
6.11 Plot of Eq. (6.12) at R = 39 *cm* 102
6.12 Ionization source rate versus drift loss rate of electrons 104
6.13 Warm electron temperature anisotropy 105
6.14 Plot of Eq. (6.12) at R = 43 *cm* 106
6.15 Plot of Eq. (6.12) at R = 48 *cm* 107

7.1 CDX plasma potential and the corresponding poloidal rotation speed 112
7.2 Cross-sectional view of CCT and the cathode limiter assembly 113
7.3 Evolution of plasma parameters with $V_{bias} = -450\,V$ and $I_{heater} = 0\,A$ 115
7.4 Contour plot of electron density from the multi-tip Langmuir probe 118
7.5 Evolution of plasma parameters of a typical H-mode with $V_{bias} = -250\,V$ and $I_{heater} = 300\,A$ 119
7.6 Time delay to reach H-mode after biasing begins 120
7.7 Evolution of (a) V_f and (b) the corresponding E_r 122
7.8 Radial profile of V_f inside and outside cathode 124
7.9 Radial profile of typical V_f in the H-mode inside and outside cathode 125
7.10 Maximum E_r as a function of V_{bias} after transition 126

Acknowledgements

First of all, I would like to thank my advisor, Dr. Masayuki Ono, for guiding me to this point with continual encouragement and support. He has showed me how to do physics with his "gut-felt" insights and intuitive formulae. My theory adviser, Dr. Choong-Seock Chang also deverves my sincere acknowledgement for his patience and understanding. He let me realize again the importance of the theoretical aspect of plasma physics and its complementary nature with experiments. Drs. Cynthia Phillips and Randy Wilson were excellent readers of this thesis, and their careful reading and many valuable suggestions made this thesis much improved and readable.

The faculty at PPPL/PU deserve my thanks for their world-class courses over my graduate years. Those wonderful moments spent in discussions with my second year theory project advisers, Drs. Russell Kulsrud and Taik Soo Hahm were certainly enjoyable. Russell always surprised me with his insights, and he helped me a lot in understanding the experimental results during my final phase of writing. Many thanks are due to all the CDX-U group members. In particular, much credit goes to Dr. Yong-Seok Hwang for his help in preparing experiments and for exciting discussions. Friendship with his family was fun. Special thanks go to Jim Taylor and Bill Kineyko not only for their technical help but also for their patience and kindness. They never complained over my incredible demand and occasional mistakes. My first year experimental project co-adviser and good friend, Dr. Douglass Darrow provided constant encouragement and support during my "ordeal". His help was a big driving force for me to press on when I was at difficult times. Thank you Doug. Discussions with my old officemate Ted Jones who works at NRL now were fun. His pride and commitment towards what he was working on always impressed me. I thank Jaeyoung Park for helping me to estimate the "rates" even if he sometimes confiscated half of my lunch. Dr. Richard Armstrong who was visiting from the University of Tromsϕ in Norway was another big help to me during my last hours of struggle with data.

I would like to acknowledge Drs. Bob Taylor, Pat Pribyl, John Liberati, and the rest of the CCT group for their kind hospitality during my stay at UCLA for the emissive limiter biasing experiment (Chapter 7).

Barbara Sarfaty had been invaluable in providing administrative assistance and helped us students to solve bureaucratic obstacles. She deserves my deep gratitude.

Learning physics was fun during several years of my stay here in Princeton, but I wouldn't say that life was always simple and easy. There were certainly happy moments and difficult times. During the time when things didn't go smoothly, lots of people provided me with encouragement. Many thanks go to all of them. I would like to thank Weonjong Lee and his family for their good friendship. My Taichi sabunim, Dr. Wonchull Park introduced me to an invaluable activity to "loosen" myself up. Learning from him was another of my good fortune. Chatting with my classmate Gordon Chiu was always fun. We talked a lot about life, religion, Bach, Lindsay String Qt, Bill Evans, physics, movie, and so on and so forth. I will miss the time that we went to the chamber music series and that we played tennis together. The friendship with many people at Kwan Um Sa Buddhist Temple in Philadelphia was unforgettable. I especially appreciate Jung-Su Sunim for his encouragement. He offered me peace in my mind during the trying period when an end to this ordeal could hardly be seen.

Finally, immeasurable thanks go to my wonderful wife, Sekyung Kim for her understanding, love, and constant encouragement throughout these years. I dare say she has as great a part as I in finishing this thesis. My family and family-in-law always showed me understanding and support throughout this work and I owe a lot to them.

Life is a never-ending DIY process as someone has said, and in this regard, I think I am very fortunate to spend a big chunk of my life in such an intellectual environment as Princeton.

Wonho Choe

December, 1995 [1]

[1] This work supported by DoE contract No. DE–AC02–76–CHO–3073.

Chapter 1

Introduction

THE MAINTENANCE OF OUR CIVILIZATION is fundamentally based on the fossil fuels because the fraction that fossil fuels take in the world's energy needs is nearly 90 % [Fulkerson *et al.*, 1990]. Even though there are large reserves of these fuels available to support the mankind for a period of time, it may not be a good strategy to rely on fossil fuel energy sources due to the various problems such as pollution, acid rain, and the risk of global warming. In this context, it would be important to have an alternative method of energy production in the next century which is environmentally safe and economically competitive without involving the combustion of conventional fossil fuels.

Nuclear fusion offers the potential of the best long-term energy supply for the world for the following reasons [DoE, 1992]: first, a fuel supply that is virtually unlimited (deuterium from ordinary sea water) and exists in sufficient quantities for millions of years; second, safety and environmental advantages in the areas of radiological hazards and nuclear materials proliferation when compared to long-term fission energy systems; advantages with respect to emissions to the atmosphere, when compared with medium-term fossil fuel options; and advantages with respect to impacts on ecological and geophysical processes when compared to renewable energy forms; third, monetary costs comparable to those of other medium-term and long-term energy options.

For the successful operation of a fusion reactor, one of the key issues to be addressed is how well the energy, particle, and momentum of a plasma is confined. Particle transport is important for energy transport, impurity effects, fueling,

plasma profile determination, and helium ash removal. Momentum confinement is an issue primarily due to the non-inductive current drive. Adequate energy confinement is essential for reactor plasmas to guarantee the production of high levels of fusion power. A widely used measure for the energy confinement is the global energy confinement time τ_E,

$$\tau_E = \frac{W_{total}}{P_{in}},$$

where W_{total} is the total stored energy of a plasma (often including beam or fast particle component) and P_{in} is the total heating input power. The actually observed energy confinement is unfortunately worse than that would be expected based on the plasma transport induced by Coulomb collisions and there is as yet no generally accepted theoretical model of turbulent transport that could account for the anomalously poor thermal insulation. Because of these reasons, much efforts have been made to obtain empirical scaling laws for the energy confinement time on the basis of statistical fitting to the available experimental data base. Here, this thesis will start by briefly reviewing a few steps of global energy confinement improvements in recent tokamak history.

1.1 Various Confinement Regimes of a Tokamak Plasma

1.1.1 Ohmic regime

From the early days of tokamak research, ohmically heated plasmas have demonstrated encouraging energy confinement scaling properties. In particular, its most important feature is that the confinement time improves linearly with plasma density ($\tau_E \propto n$) [Equipe TFR, 1979; Gaudreau *et al.*, 1977; Klüber and Murmann, 1982]. This suggests that $n\tau_E$ is proportional to n^2, and accordingly, the required $n\tau_E$ values for breakeven can be obtained in the fusion relevant high density regimes. A few among a large number of proposed empirical scaling laws are INTOR, Merezhkin-Mukhovatov, Neo-Alcator, and Goldston scalings. Unfortunately, however, the confinement improvement with density was lost and the confinement was observed to saturate at high densities [Murakami *et al.*, 1979]. A few years

later, an enhanced confinement regime characterized by peaked density profiles, at high density, has been obtained in ASDEX ohmic plasmas [Söldner *et al.*, 1988] by wall conditioning and reduction of gas influx. In this experiment, they observed an unsaturated linear rise of the energy confinement time with density up to the density limit, and it was termed as the improved ohmic confinement (IOC) regime. There is another exception: recent transport experiments in Alcator-C-Mod showed that ohmic τ_E had no scaling with density and reached values of 2-3 times of neo-Alcator. Their conclusion is that Alcator-C-Mod ohmic confinement follows an L-mode-like scaling which is for low densities.

1.1.2 L-mode

Since it is difficult to reach the ignition with ohmic heating alone, a variety of auxiliary heating methods have been utilized. During the early phase of tokamak heating experiments, the plasma confinement was observed to improve with increasing current but degrade from the ohmic value with increasing additional heating power (L-mode). This may be a serious disadvantage for applying this confinement regime for large size reactor grade future devices such as ITER. Other characteristics of L-mode are weak dependence of density and toroidal field, and the lack of any clear macroscopic phenomena to which to ascribe the degradation of confinement with increasing power [Stambaugh *et al.*, 1990]. Goldston's L-mode power scaling is a typical empirical scaling for this confinement regime, and considering different heating methods and plasma configuration, there have a number of other scalings been proposed in the framework of ITER activities. ITER L-mode power scaling has a form:

$$\tau_E^{\mathrm{ITER89-P}} \propto I_p^{0.85} R^{1.20}\, P_{in}^{-0.50},$$

where I_p, R, P_{in} are plasma current, major radius, and input heating power, respectively.

1.1.3 H-mode

At the 1982 IAEA meeting held at Baltimore, the discovery of a new improved confinement compared to conventional L-mode in diverted ASDEX plasmas was

reported [Wagner *et al.*, 1982]. Since then, the so-called H-mode or H-regime has been observed in many tokamaks worldwide first in diverted plasmas and later also in limiter discharges. It is typically characterized by the flat density profile. At any rate, H-mode is a promising regime for fusion reactors and it is essential to be able to predict its operational window in future devices. A more detailed review of H-mode characteristics and investigations will be given in Section 1.2. The most recent estimation for the thermal energy confinement [Kaye *et al.*, 1995] is

$$\tau_E^{\mathrm{ELMy}} = 0.022\, I_p^{0.76} R^{2.60} \epsilon^{0.30} \kappa^{1.05}\, \overline{n}^{0.42}\, B_T^{0.15} A_i^{0.30} P_{in}^{-0.70},$$
$$\tau_E^{\mathrm{ELM-free}} = 0.036\, I_p^{1.06} R^{1.79} \epsilon^{-0.11} \kappa^{0.66}\, \overline{n}^{0.17}\, B_T^{0.32} A_i^{0.41} P_{in}^{-0.67}.$$

All units are in [sec, MA, m, $10^{19} m^{-3}$, T, AMU, MW].

1.1.4 Supershot regime on TFTR

On TFTR, an improved confinement regime that is quite different from H-mode was observed [Strachan *et al.*, 1987]. It is achieved in a low density target plasma which is heated and fueled centrally by high power deuterium neutral beam injection. A necessary condition for this regime is a very low edge recycling which can be accomplished by substantial discharge preparation via wall cleaning. As a result, it is characterized by very peaked density and temperature profiles and it has yield the largest neutron production thus far on TFTR. Enhancement of τ_E correlates with the peaking of density profile and T_i/T_e (Hot Ion mode), and both the central and global confinement improve by up to a factor of three of L-mode scaling. The energy confinement time is weakly dependent on plasma current and neutral beam power.

1.1.5 PEP H-mode on JET

The main feature of the Pellet Enhanced Plasma (PEP) H-modes [JET Team, 1993] achieved on JET is a dense plasma core ($r/a < 0.3 - 0.4$) created by the injection of $4 - 6\, mm$ pellets just prior to the application of strong additional heating (NBI or ICRH) when the current profile is still approaching equilibrium and sawteeth are not yet developed. The peaked density profiles of the PEP have been

combined with the edge related confinement enhancement obtained in the H-mode regime. The duration of the PEP H-mode phase is typically $0.5 - 1.0\,sec$, which is $\sim (50 - 100)\,\%$ of the energy confinement time. Some of the discharges have global confinement enhancement relative to Goldston L-mode value of ~ 3.

1.1.6 VH-mode on DIII-D

It was observed on DIII-D [Greenfield *et al.*, 1992] that confinement in the H-mode continued to rise during the discharge after boronization of the vessel wall or after the vessel was fully covered with graphite tiles. The improvement is related to spreading of radial electric field toward plasma center, i.e., increased thickness of E-layer, faster toroidal plasma rotation speed, and the increase of the ion pressure gradient. Braking experiments of toroidal rotation with $n = 1$ magnetic error field [LaHaye *et al.*, 1993] revealed the degradation of additional confinement improvement when the toroidal rotation was reduced. Another observation on a VH-mode plasma is the increase of scrape-off layer thickness at the separatrix suggesting that impurity influx can be reduced and thus the discharge may be cleaner.

1.1.7 CH-mode on PBX-M

Application of low power Ion Bernstein Wave heating on PBX-M device brought about an improvement of H-mode confinement [Ono *et al.*, 1995a]. Consequently, a significant increase in the particle, ion energy, and toroidal momentum confinement in the core region was observed. The strong toroidal plasma rotational shear was also seen. The inferred diffusivities reach neoclassical values inside the IBW induced transport barrier region [Ono *et al.*, 1995b].

1.1.8 Internal Transport Barrier on JT-60U

Spontaneous formation of an internal transport barrier was observed associated with improved confinement in the high β_p discharges in the JT-60U tokamak [Koide *et al.*, 1994]. The radial location of the transport barrier appeared to be on the $q = 3$ surface. The energy confinement factor, $\tau_E/\tau_E^{\mathrm{ITER89-P}}$ increased up to 3.6. A high plasma poloidal rotation ($\sim 50\,km/s$) was also observed at $r/a = 0.8$.

1.2 Observation of H-mode

The so-called H-mode was discovered in ASDEX [Wagner *et al.*, 1982] in 1982. Compared to L-type discharges, they termed 'H-type discharges' for ones that showed a sudden density increase without modifications from the external controls (the density continued to rise and exceeded the value obtained during the plateau of the Ohmic phase even though the gas valve was closed) and the increase of T_e above that of the L-type discharge despite the increase of electron density. The increase in density is caused by a sudden improvement in particle confinement which was indicated by the drop of $H_\alpha - D_\alpha$ and hard x-ray radiation at the transition. Poloidal beta increased by a factor of 2 compared to L-type, although the neutral beam injection power was only 18 % larger. The global energy confinement time τ_E increased from $20 - 30\,msec$ (L-type) to $40 - 50\,msec$ (H-type). According to their observations, H-type could be observed only with the neutral beam injection power larger than $1.9\,MW$ suggesting the existence of auxiliary heating power threshold. H-type discharges were not observed for cylindrical $q(a)$ less than 2.6. The observed transition back into the L regimes occurred simultaneously with, or was triggered, by a short burst (named later as 'Edge Localized Mode') detected by Mirnov coils and soft x-ray signals, which lead to periodic density and temperature reductions in the outer plasma zones. Another interesting thing they observed was that they could transition to the H regime only from diverted discharges, never from discharges with limiters. They attributed this to the higher impurity content coming from limiters, thus, larger radiation at the plasma edge suppressing the formation of very broad temperature and density profiles which are characteristics of H-type discharges. Interestingly, however, H-mode was obtained a few years later in many limiter experiments [Matsumoto *et al.*, 1987a; Matsumoto *et al.*, 1987b; Odajima *et al.*, 1987; Sengoku *et al.*, 1987; Schissel *et al.*, 1989; Toi *et al.*, 1989; Burrell *et al.*, 1989; Bush *et al.*, 1990; Bush *et al.*, 1991; Bush *et al.*, 1994].

Since the discovery of H-modes in ASDEX, many devices have reproduced this improved confinement regime by various different methods. H-mode plasmas can be categorized according to how they are triggered. First, 'spontaneous H-modes' develop from L-mode discharges with sufficient heating power via neutral beam heating [Wagner *et al.*, 1984; Kaye *et al.*, 1984; Tanga *et al.*, 1987; Bur-

RELL *et al.*, 1987; SENGOKU *et al.*, 1987; KIKUCHI *et al.*, 1993], ion cyclotron resonance heating [KEILHACKER *et al.*, 1986; STEINMETZ *et al.*, 1987; MATSUMOTO *et al.*, 1987a; TUBBING *et al.*, 1989], electron cyclotron resonance heating [LOHR *et al.*, 1988; HOSHINO *et al.*, 1989; ERCKMANN *et al.*, 1993a; ERCKMANN *et al.*, 1993b], lower hybrid heating [TSUJI *et al.*, 1990], and the combination of neutral beam heating and electron cyclotron resonance heating [HOSHINO *et al.*, 1988]. H-mode was observed also in the ohmically heated plasmas [OSBORNE *et al.*, 1990; KAUFMANN *et al.*, 1993; RYTER *et al.*, 1993; CAROLAN *et al.*, 1994; SNIPES *et al.*, 1994]. Second, 'biased H-modes' are obtained by biasing plasmas utilizing inserted probes or electrodes [TAYLOR *et al.*, 1989; TAYLOR *et al.*, 1991; WEYNANTS *et al.*, 1990; NIEUWENHOVE *et al.*, 1991; ASKINAZI *et al.*, 1992], divertor plates [MIURA *et al.*, 1991; MAHDAVI *et al.*, 1991; COUTURE *et al.*, 1992], limiters [SHIMADA *et al.*, 1985; CONN *et al.*, 1987; PHILLIPS *et al.*, 1987; SHIMADA *et al.*, 1990; COUTURE *et al.*, 1990; SAKAI *et al.*, 1993]. It is interesting to note that even though H-modes are triggered by different means, the resulting phenomenology is very similar, suggesting that the underlying physics may also be similar.

As was noted in the previous paragraph, one of the most important characteristics of H-mode is that the global energy confinement time is two or three times longer than that in conventional L-mode plasmas [SCHISSEL *et al.*, 1991]. The global particle confinement time in H-mode is also significantly increased. Based on observations from many different devices, a few common signatures of the transition to H-mode at the plasma edge are described as an abrupt reduction of H_α or D_α emission indicating a significant reduction of gas recycling, increase in ∇n and ∇T, decrease of edge fluctuation levels [LEHACKA *et al.*, 1989; HOLZHAUER and DODEL, 1990; MANSO *et al.*, 1991; HOLZHAUER *et al.*, 1994; TYNAN *et al.*, 1994], occasional appearance of edge localized modes (ELM), and increase in $|E_r|$. During the ELM-free phase, the rise and flattening of density profile was observed and rise of core temperature, and thus, of stored energy was also seen [LAZARUS *et al.*, 1992].

One of the findings in ASDEX experiments was that the neutral beam power was required to be larger than a certain value for the H-mode to appear. The existence of this threshold power for spontaneous H-mode is also a common feature observed in various devices. The power threshold may be a function of many pa-

rameters including plasma density, toroidal field, cleanness of wall, and so on. There is extensive evidence that the power threshold is a requirement for the edge temperature to exceed a critical value. Not only in spontaneous H-modes but also in biased H-modes, a threshold exists. As an example in Chapter 7 will show, the bias voltage of a biased limiter (or any other biasing tools such as a probe or a divertor plate) should be larger than a certain value for triggering H-modes, which suggests that there exists a threshold in radial currents.

The onset of H-mode can also be identified by the formation of a transport barrier [Wagner *et al.*, 1984; Tynan *et al.*, 1994] just inside the last closed flux surface where density and temperature gradients steepen after the transition. This is usually accompanied by a formation of a velocity shear layer at the edge. When there is a barrier formation, a radial electric field with a steep gradient is also known to develop at the plasma edge [Taylor *et al.*, 1989; Groebner *et al.*, 1990b; Groebner *et al.*, 1990a; Groebner *et al.*, 1991; Ida *et al.*, 1990; Nieuwenhove *et al.*, 1991; Ida *et al.*, 1992; Field *et al.*, 1992; Hawkes, 1993]. This electric field, related to plasma rotation [Burrell *et al.*, 1994; Kim *et al.*, 1994b; Kim *et al.*, 1994a], is believed to play a crucial role in the L- to H-mode and further to the VH-mode transition.

The improved confinement mode is not a unique feature of a tokamak. Similar observations have been made in a stellarator [Wagner *et al.*, 1994], in a Heliotron/Torsatron [Toi *et al.*, 1993; Toi *et al.*, 1994], and in a linear tandem mirror [Sakai *et al.*, 1993]. Since the observed phenomena linked to H-modes are very similar even though the improved modes are produced in many different configurations by various different means, there have been a lot of theoretical efforts to find out a possible generalized mechanism explaining the observations for years. The prevailing hypothesis for the L-H and H-VH mode transition to date is the stabilization of turbulence due to sheared $\mathbf{E} \times \mathbf{B}$ flow [Biglari *et al.*, 1990; Shaing *et al.*, 1990]. In other words, the confinement with a transport barrier is improved due to a reduction in turbulence-driven transport that is caused by an increase of shear in v_E $(= \mathbf{E} \times \mathbf{B}/B^2)$. According to this hypothesis of decorrelation of turbulence by sheared flow, a turbulent eddy flows at v_E, and its shear dv_E/dr tilts, stretches and rips an eddy apart. This theory has been supported by many experiments [ASDEX Team, 1989; Ida *et al.*, 1992; Lohr *et al.*, 1993; Rettig *et al.*,

1993; Burrell *et al.*, 1994; Coda and Porkolab, 1995] in which it has been observed that transport barrier, fluctuation suppression, and high velocity shear occur in the same radial region.

1.3 Importance of H-mode for Future Devices

In addition to the enhancement of energy and particle confinement, there are several other important aspects of H-mode for future devices [Wagner, 1994]. According to the ITER EDA concept, the required plasma size and plasma current for an ignition device are more modest in H-mode than in L-mode to generate the same amount of fusion power. The broader density and temperature profiles compared to L-mode give a larger stored energy. Therefore, H-modes can provide high β discharges, which is related to plasma stability and the economics of a fusion reactor. H-mode plasmas have larger bootstrap current contribution than L-mode plasmas and it is also possible to have H-mode plasmas without sawteeth. Another important aspect of H-mode in conjunction with fusion reactors lies in the possibility of providing a helium ash removal with the help of ELMs. The particle transport rates for helium exhaust in ELMing H-mode appear to be fast enough to remove helium ash from a reactor [Hillis *et al.*, 1993; Hillis *et al.*, 1994].

1.4 Thesis Motivation

Based on the experimental findings of L-H and H-VH mode transition that are summarized in the previous sections, one of potential problems of H-mode in tokamak plasmas is that a large amount of auxiliary power would be required for high density, high temperature reactor-grade future devices to produce H-mode discharges according to the current threshold power scaling [Kaye *et al.*, 1995]:

$$P_{th} = 0.025\, n_e^{0.75} B_T\, S,$$

or

$$P_{th} = 0.4\, n_e B_T R^{2.5},$$

where $n_e(10^{20}\,m^{-3})$, $B_T(T)$, $S(m^2)$, and $R(m)$ are electron density, toroidal magnetic field, plasma surface area, and major radius, respectively. These types of scaling suggest that $P_{th} > 100\,MW$ for ITER. Therefore, it is important to think of any way to lower this threshold power in large scale future devices. In order to fulfill this, the first question we can ask ourselves is what exactly triggers those improved modes. Recent experiments on DIII-D have confirmed the correlation between H-mode and VH-mode transitions and increased radial electric field and plasma rotation near the plasma edge as was discussed in the previous section. Along with the observations, the prevailing hypothesis for the L-H and H-VH mode transition to date is the stabilization of turbulence due to sheared $\mathbf{E} \times \mathbf{B}$ flow [Biglari *et al.*, 1990; Shaing *et al.*, 1990; Hahm and Burrell, 1995] (the reasons why $\mathbf{E}\times\mathbf{B}$ shear is considered as the fundamental quantity are addressed in Ref. [Burrell *et al.*, 1994]). Therefore, if the radial electric field is the main cause of the transition, as found in many devices and provided by theories, it would be quite natural to ask next whether it is possible to generate radial electric fields by external means and thereby to develop more efficient ways to achieve improved confinement in large scale future devices. Some efforts to accomplish this goal have already been attempted. Experiments on CCT [Taylor *et al.*, 1989; Taylor *et al.*, 1991] demonstrated that it is possible to produce an H-mode plasma by imposing an edge radial electric field to a tokamak discharge, i.e. an externally-injected radial current from a biased electrode inserted into the plasma. Similar experiments has been attempted elsewhere [Askinazi *et al.*, 1992; Weynants *et al.*, 1990]. These experimental observations are consistent with plasma bifurcation theories. On CCT, the radial current required for inducing H-mode was only $20\,A$ and theoretical estimates for larger plasmas also suggest a similar order of radial current is needed. This implies that the actual power necessary to support such a radial electric field could be relatively modest even for large devices.

The motivation of this thesis research is to develop concepts for controlling tokamak plasma transport (or improving plasma confinement) by utilizing injection of hot electrons, i.e. to develop a versatile 'knob' to control the plasma transport. This would be of great importance because it could help the optimization of tokamak plasma performance, eventually making tokamak reactors more economical. Keeping the motivation in mind, two novel concepts (that have not been tested elsewhere) have been introduced and tested in this research: the electron ripple injection tech-

nique and tokamak edge plasma biasing with an electron emitting limiter. The first method, the electron ripple injection (ERI) method has been developed to induce radial electric fields in a less intrusive way without introducing any material to a plasma [Ono *et al.*, 1990; Choe *et al.*, 1993b; Choe *et al.*, 1995b; Choe *et al.*, 1995c]. The second method, the emissive limiter biasing experiment was performed in the Continuous Current Tokamak (CCT) device at UCLA [Choe *et al.*, 1993a]. It involves a simple injection of hot electrons at the plasma edge from the limiter. The detailed descriptions and discussions will be found in the following chapters.

1.5 Thesis Organization and Overview

A detailed discussion of the electron ripple injection concept is presented in Chapter 2. A computer code was developed to study the 3-dimensional complex magnetic field structure and to help the design and fabrication of ripple coils. In Chapter 3, a kinetic calculation was done to investigate the resonant electron temperature anisotropy generated by electron cyclotron resonance heating. The perpendicular and parallel energy moments of the Fokker-Planck equation including ripple transport was solved analytically. In order to understand the behavior of energetic electrons and the generation of a radial electric field in the presence of ripple fields, a Monte-Carlo guiding-center electron orbit code was developed, and is described in Chapter 4. Chapter 5 gives a brief description of the CDX-U device where a prototype electron ripple injector was installed. Results from the preliminary electron ripple injection experiments on CDX-U are presented in Chapter 6. Chapter 7 discusses the second approach, namely, the improvement of tokamak plasma confinement utilizing a limiter which is capable of emitting electrons, i.e., negatively-biased emissive limiter. This experiment was done as a collaborative work between the UCLA CCT group and the PPPL CDX-U group. Finally, major findings are summarized and recommendations for future studies are made in Chapter 8.

Chapter 2

Principle of Electron Ripple Injector

OVER THE YEARS, there have been several excellent plasma biasing experiments to get H-mode using an inserted electrode or a probe. However, it is desirable to develop an alternative method which is compatible with and extendable to high density and temperature plasmas in future devices. In particular, material electrodes placed in reactor-relevant plasmas would be rapidly destroyed and could easily cause other problems with the plasmas. This is the motivation for developing the electron ripple injection (ERI) method [Ono *et al.*, 1990; Choe *et al.*, 1993b; Choe *et al.*, 1995b; Choe *et al.*, 1995c], i.e., to induce radial electric fields at the plasma edge in a non-intrusive way by injecting electrons into the plasma interior. This technique has the advantages that the physics is relatively simple, it is non-intrusive, easily controllable, and therefore applicable to larger size fusion devices with a high level of confidence.

The principle of the concept is as follows: a pair of magnets are used to provide bending of poloidal magnetic fields (referred to as 'magnetic field ripple'), resulting in the creation of a magnetic well which is localized toroidally and poloidally (see Fig. 2.1 and Fig. 2.2). As they follow magnetic field lines, some electrons at the plasma edge which have larger perpendicular energy than parallel energy brought about by electron cyclotron resonance heating (ECRH) feel the magnetic well and can be trapped in the ripple region. While being trapped, these electrons will move toward the plasma center via ∇B and curvature drifts by placing the ripple

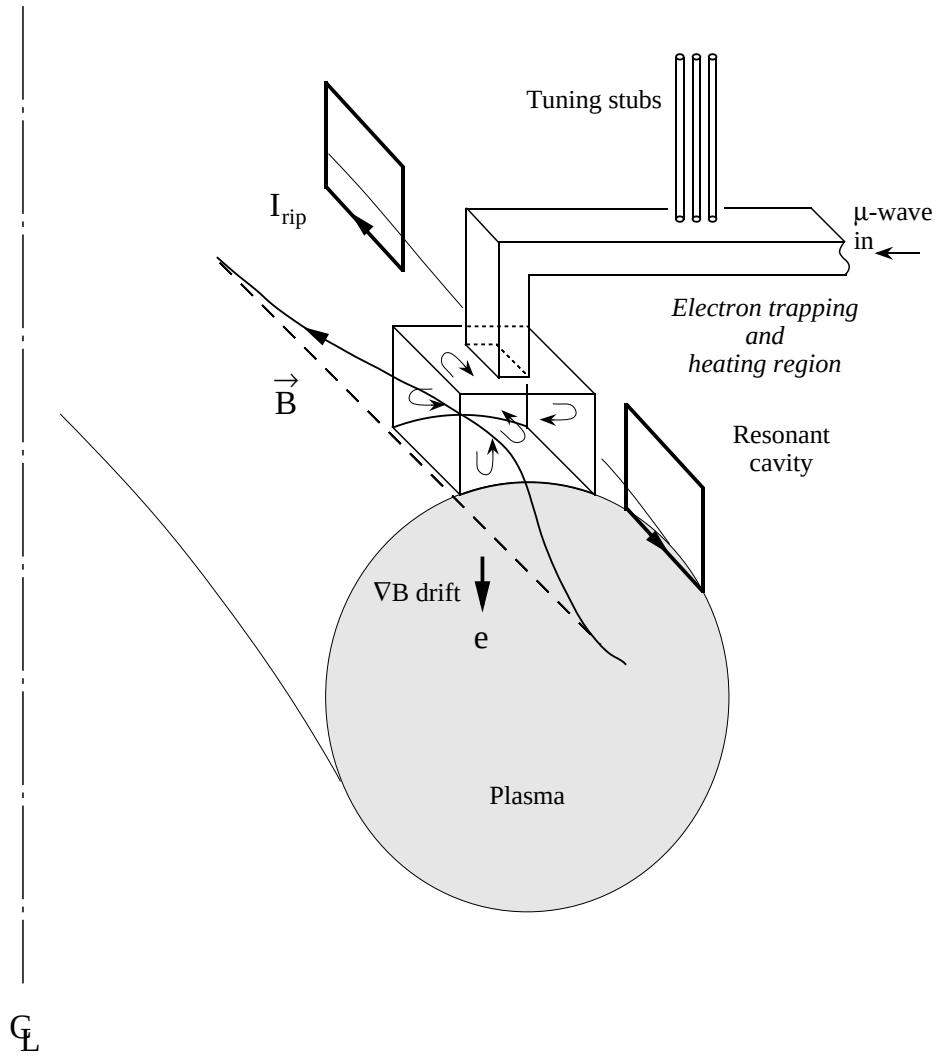

Figure 2.1: Schematic of the electron ripple injector

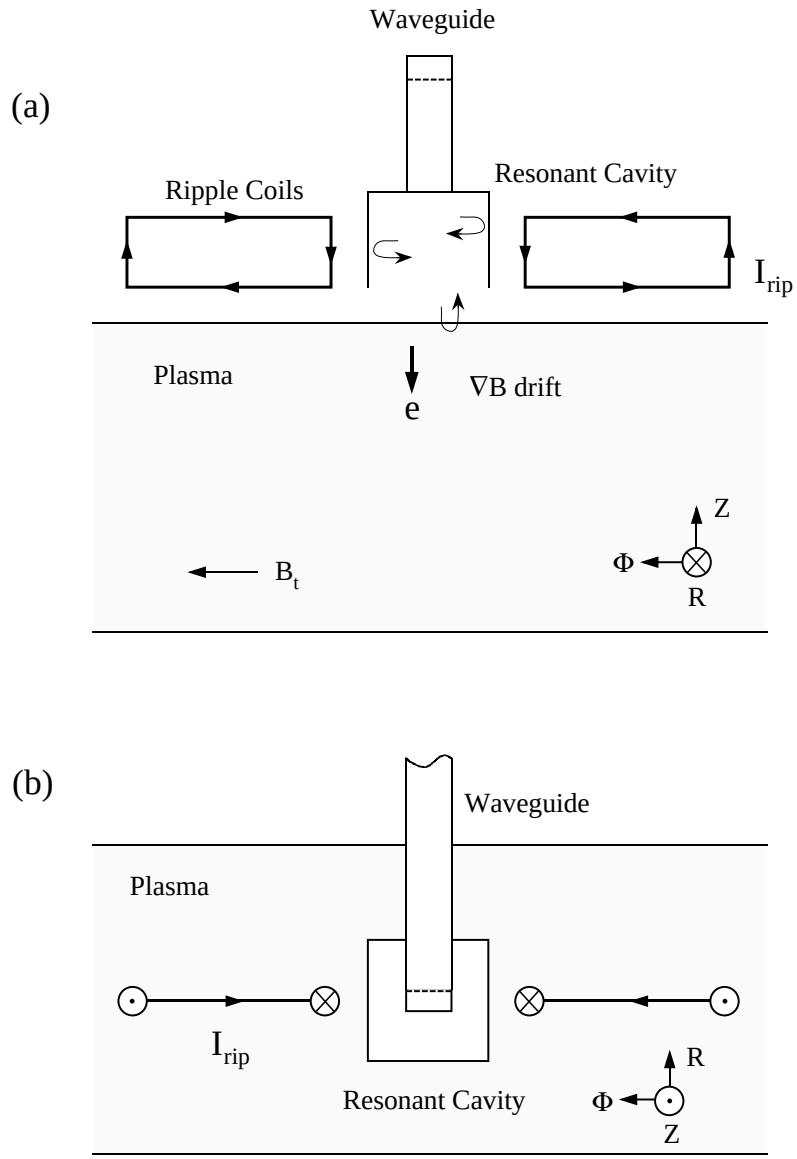

Figure 2.2: Schematic of the electron ripple injector (a) seen from the major axis, and (b) viewed from the top of a tokamak plasma.

region appropriately. Since the direction of the ∇B drift depends upon the toroidal field direction, the electron injector should be placed either at the top or bottom of a torus in order for the the drift direction to point toward the plasma center. The ripple-trapped electrons will eventually be detrapped due to collisions between the particles and due to the decrease of the field ripple strength away from the ripple source. Since these penetrated electrons accumulate at the flux surfaces where they are detrapped from the ripple region, the net effect is to charge the plasma negatively, resulting in a build-up of electrostatic potentials, i.e., radial electric fields (E_r) from the edge toward the plasma center with a scale length of the penetration distance.

The ripple strength is defined as,

$$\delta(\%) = \frac{B_{max} - B_{min}}{B_{max} + B_{min}} \times 100, \tag{2.1}$$

where B_{max} and B_{min} are maximum and minimum fields in the ripple region. If δ is 5 %, then the trapping condition would be

$$\frac{v_\perp}{v_\parallel} \geq \left(\frac{2\delta}{1-\delta}\right)^{-1/2} \simeq 3.$$

Therefore, it is important to have electrons which have predominantly perpendicular energy. The temperature anisotropy will be provided by ECRH.

In the design of ripple coils, a few requirements should be satisfied. First, as discussed earlier, the coils should be positioned appropriately to provide drift of the ripple-trapped electrons toward the plasma center before detrapping takes place. Second, the ripple strength must be high enough in the ripple region, but the radial variation of the ripple strength must be sufficiently rapid in order for drifting electrons to become detrapped after drifting a desired radial distance. Third, the ripple strength should be kept minimum to prevent serious plasma perturbation. According to the experimental results in DIII-D [Groebner *et al.*, 1990b], the thickness of the electric field layer during H-mode transition appears to be $(1-3)$ *cm* inside the last closed flux surface. This suggests that the radial penetration distance of injected electrons, which is determined by ripple strength and electron energy, needs to be at least of this order. Considering all these requirements, δ would be

typically a few percent for the electron ripple injection experiments as will be shown in Chapter 4.

Several different configurations of ripple coils were studied for ripple-assisted neutral beam injection [Goldston *et al.*, 1977] (Fig. 2.3). For our purposes, we consider two different types of ripple coil configuration. The first type is shown in Fig. 2.1 and Fig. 2.2 (this will be called as *TypeI* hereafter) where a pair of rectangular-shaped ripple coils are vertically aligned toroidally to provide a desired amount of field ripple. A numerical code was developed in order to visualize the generation of local magnetic well out of these coils. In the code, the magnetic field line equations with the Biot-Savart law were solved to trace each field line in cylindrical coordinates (R, ϕ, Z) where R, ϕ, Z are major radial, toroidal, and vertical coordinates, respectively:

$$\frac{dR}{B_R} = R\frac{d\phi}{B_\phi} = \frac{dZ}{B_Z} = \frac{d\ell}{B}, \tag{2.2}$$

where $d\ell = [(dR)^2 + (d\phi)^2 + (dZ)^2]^{1/2}$ is the arc length and B is the total magnetic field. In the present work, the radial direction always means the direction of increasing major radius unless otherwise specified. The ripple field is calculated by modeling the ripple coils with filamentary currents. For the calculation, ripple coils are assumed to be located at $R = 35\,cm$, $Z = 42\,cm$ on CDX-U device. Figure 2.4 depicts several different magnetic field lines with $B_0 = 1\,kG$, $R_0 = 35\,cm$, and the ripple coil current $I_{rip} = 10\,kA{\cdot}turn$. The figure shows radially-outward field line bending and the generation of a local magnetic well around ripple coils. With this value of ripple coil currents, a ripple strength of 5.8 % can be obtained. The poloidal field is not included for the calculation and the addition of poloidal field simply makes field lines oblique. Figure 2.5 shows a different view of the total field strength. This figure clearly shows the generation of toroidally localized magnetic well that arises from the $1/R$-dependent toroidal field. Figure 2.6 is a contour plot of ripple strength and the localization of the field ripple is seen around the ripple coils. We should note that this localized ripple field is inherently different from the ripple fields of toroidal magnets. Here, the effective 'ripple' is produced without introducing the regular toroidal field ripple structures.

For the electron ripple injection experiments on CDX-U, we used a slightly different configuration (*TypeII*) in order to produce more prominent effects of ripple

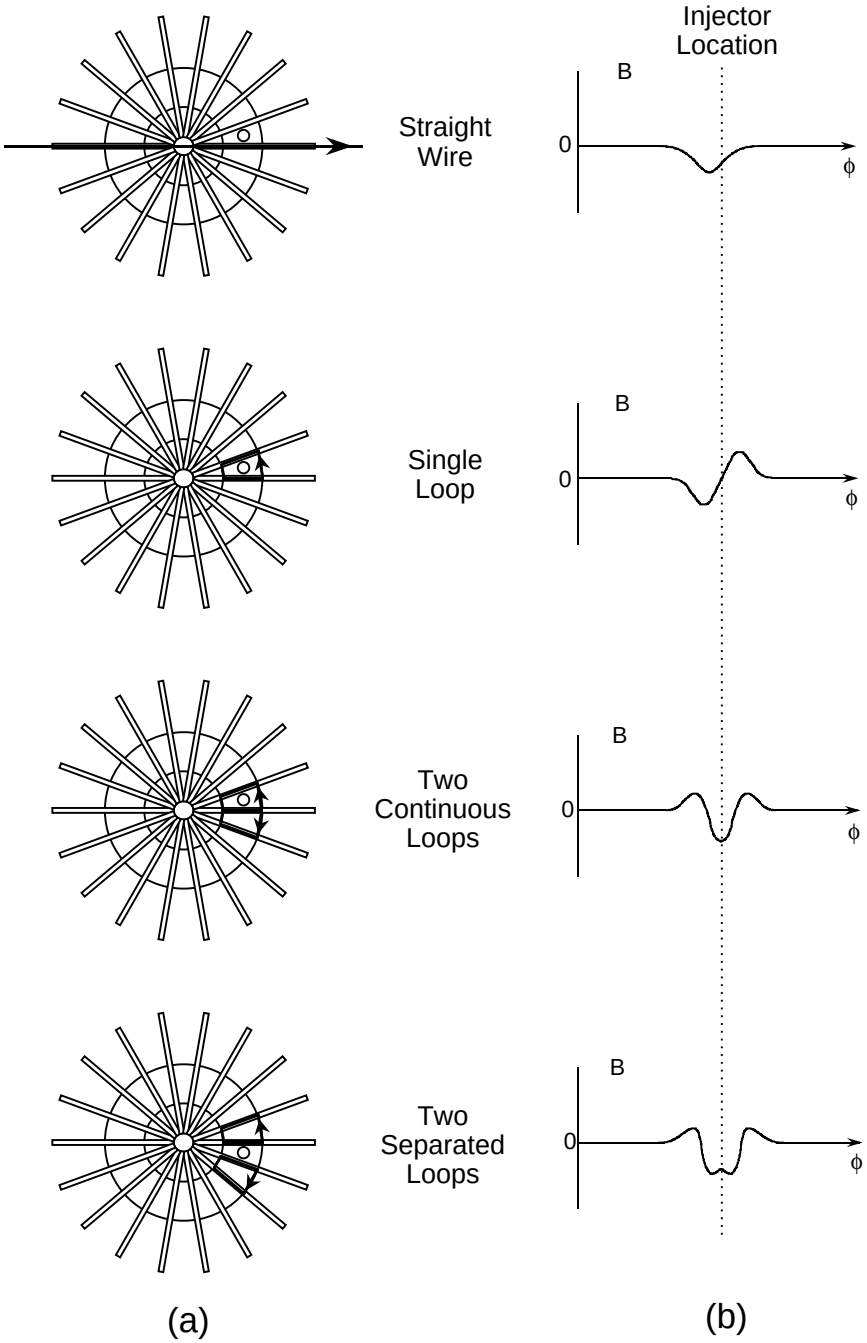

Figure 2.3: (a) Various ripple coil configurations considered in Ref. [Goldston *et al.*, 1977]. The small circle denotes the beam injector port. (b) Variation in magnetic field along a field line.

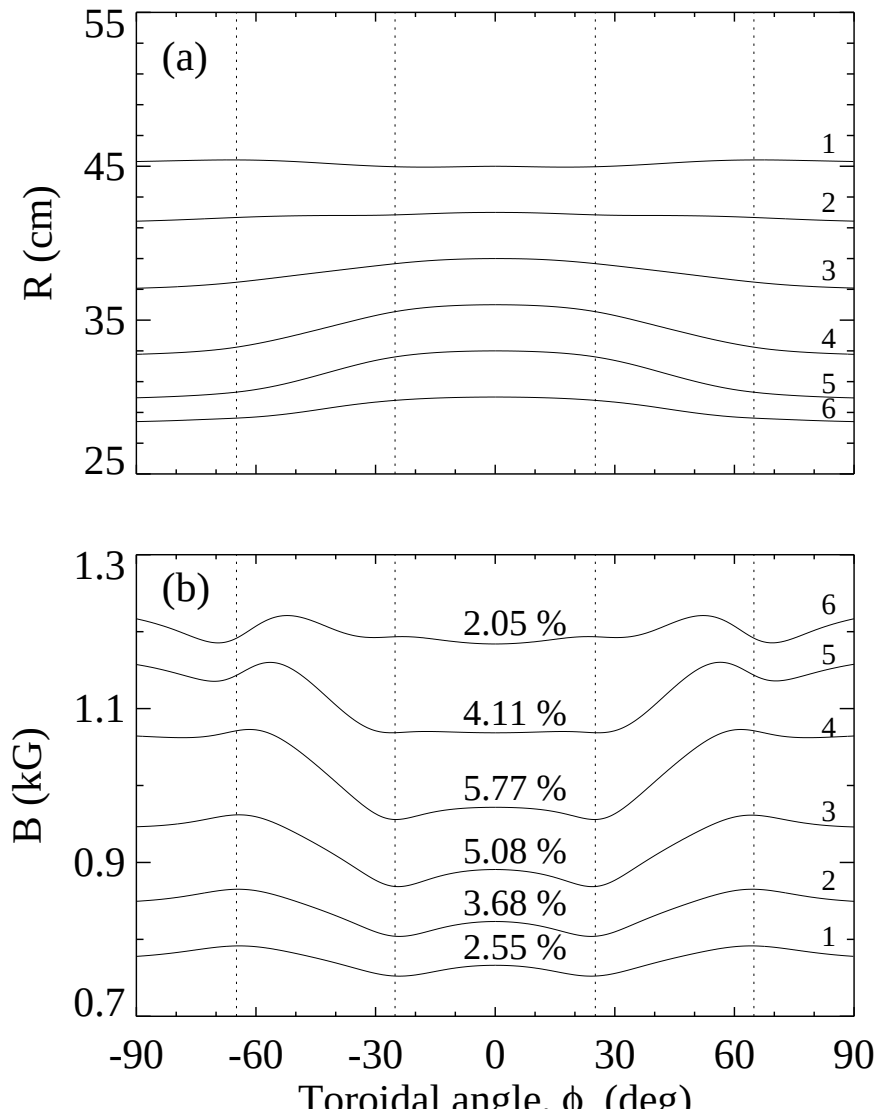

Figure 2.4: Magnetic field lines at different radial positions but at $Z = 33\,cm$ where $\mathbf{B} = \mathbf{B}_{TF} + \mathbf{B}_{rip}$. Ripple coils are aligned as in Fig. 2.1 and are assumed to be located at $R = 35\,cm$, $Z = 42\,cm$. $I_{rip} = 10\,kA{\cdot}turn$. Shown in the middle of (b) is magnetic field ripple strength of each field line. Dotted lines indicate the toroidal location of ripple coils.

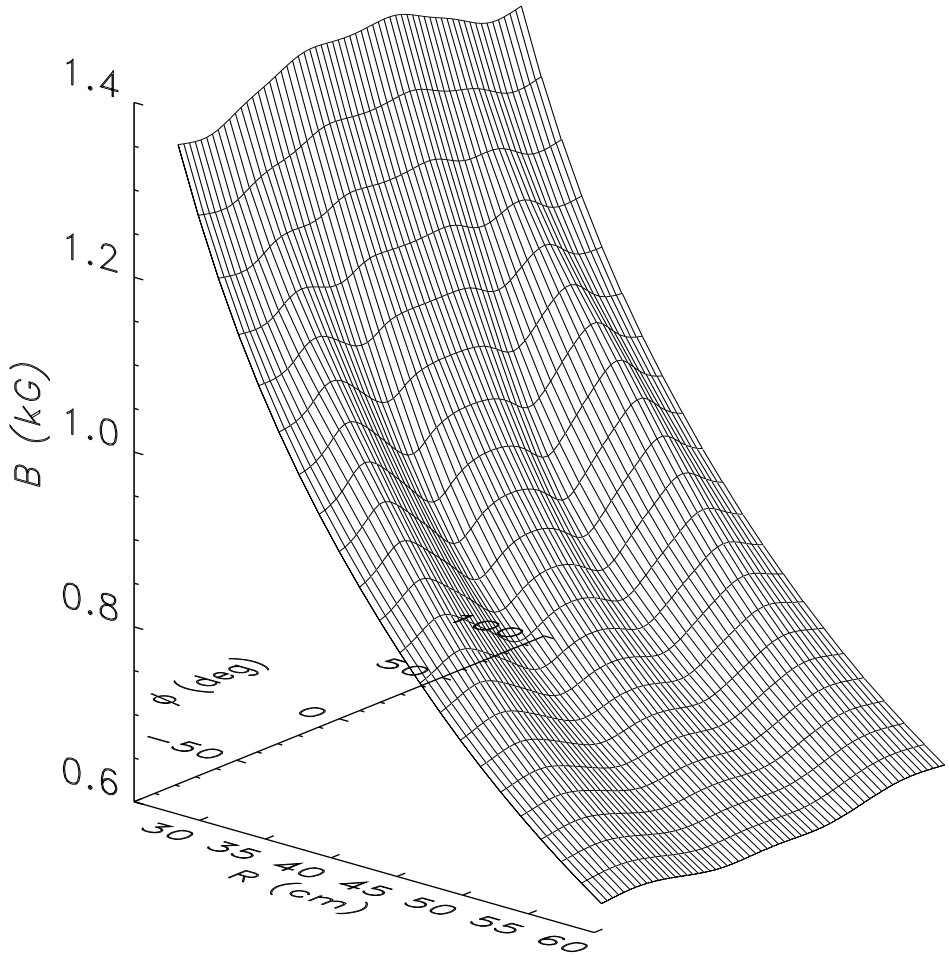

Figure 2.5: 3-dimensional plot of magnetic field strength (*Type I*). $1/R$-dependence by toroidal field is seen and local magnetic well is created by ripple coils.

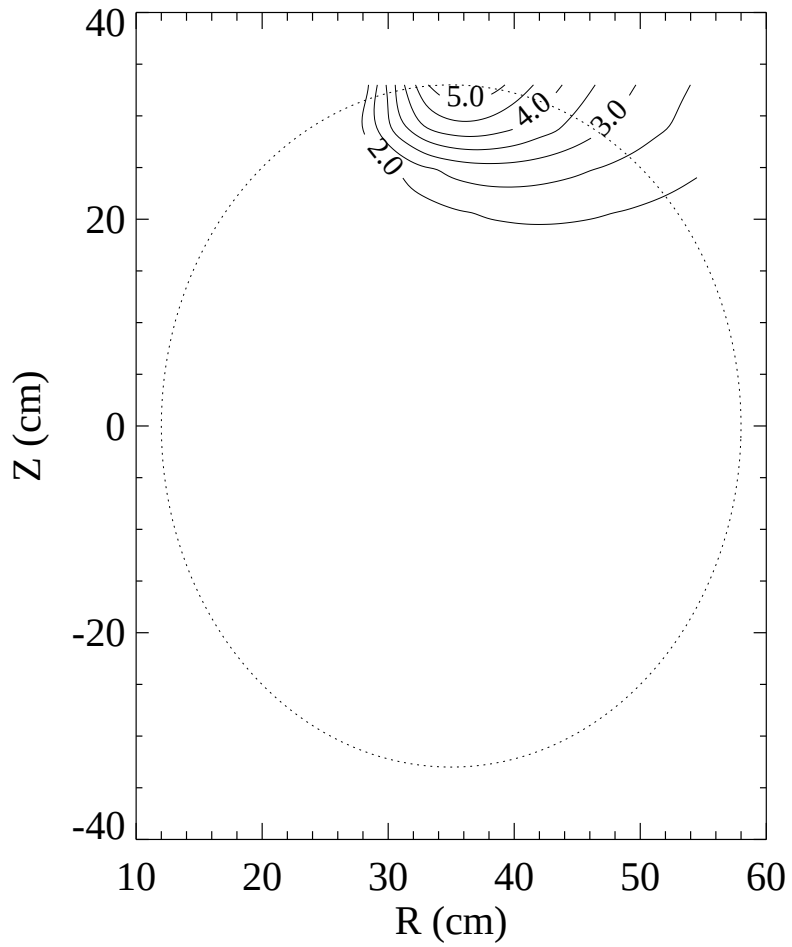

Figure 2.6: Contour plot of field ripple strength with toroidal angle of 25° from the center of ripple coils. Dotted line depicts the plasma region.

fields on the electron behavior. In this particular configuration, the field ripple is local in the toroidal sense but global in the vertical direction as depicted in Fig. 2.7. Several field lines with ripple strengths in this setup are shown in Fig. 2.8. Since the ripple source is located at the outboard side where toroidal field is low, the strength of the ripple decreases toward the major axis. 3-dimensional plot of magnetic field strength is also plotted in Fig. 2.9. The radial distance which electrons can penetrate can be adjusted by controlling the injected electron energy and the ripple strength, as discussed in Chapter 4 in more detail.

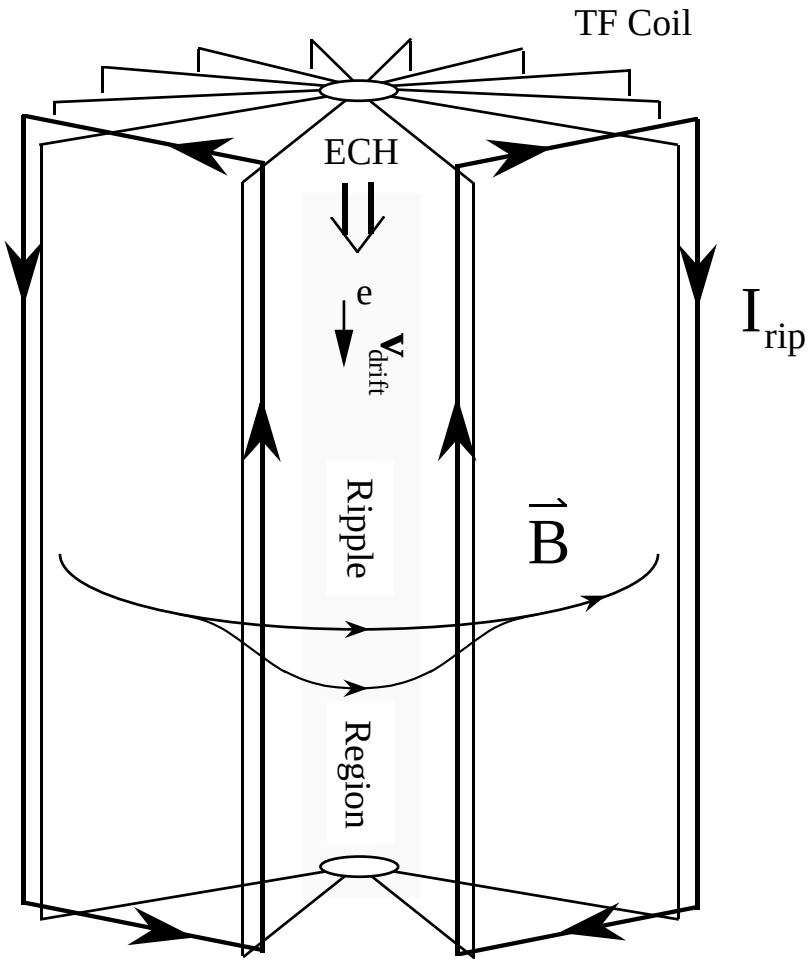

Figure 2.7: A pair of ripple coils (*TypeII*) with rectangular-shaped CDX-U toroidal field coils. Ripple effect can be expected global in the vertical direction.

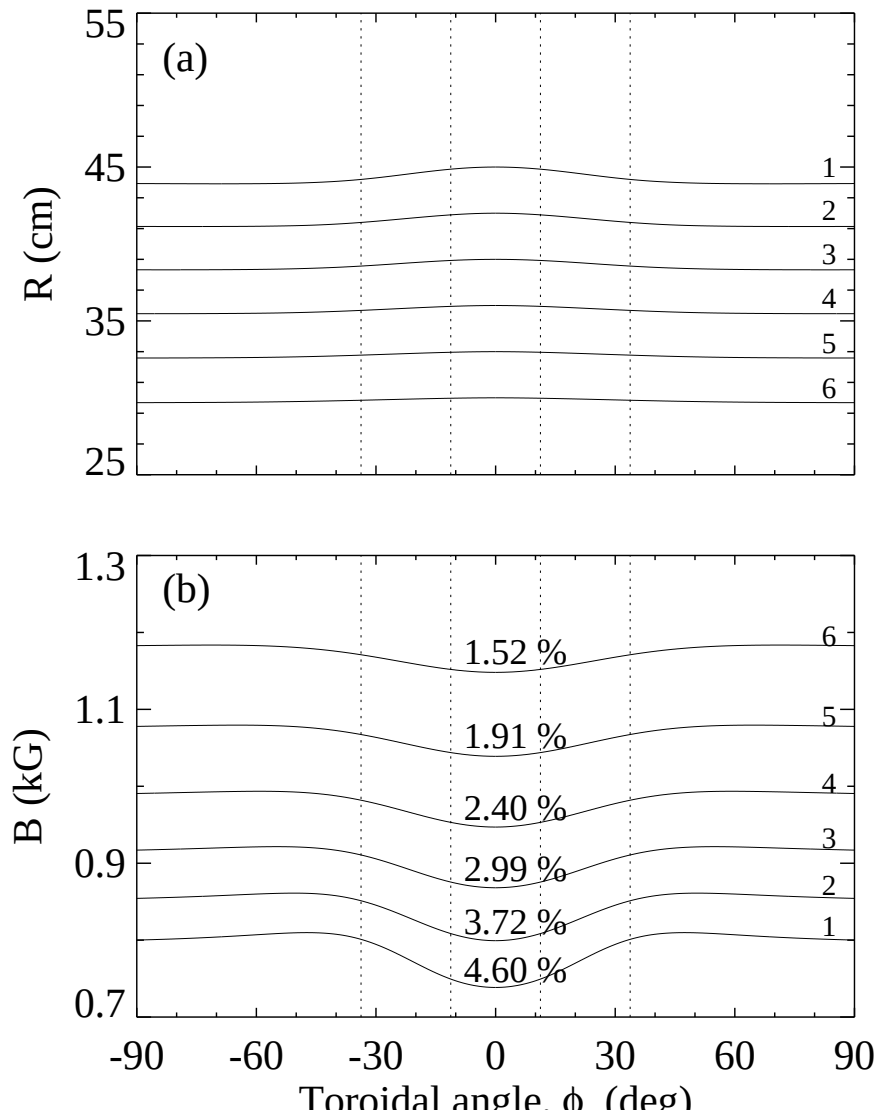

Figure 2.8: Magnetic field lines in Fig. 2.7 with $B_0 = 1\,kG$, $R_0 = 35\,cm$, $I_{rip} = 5\,kA\cdot turn$. The numbering is for indicating each field line.

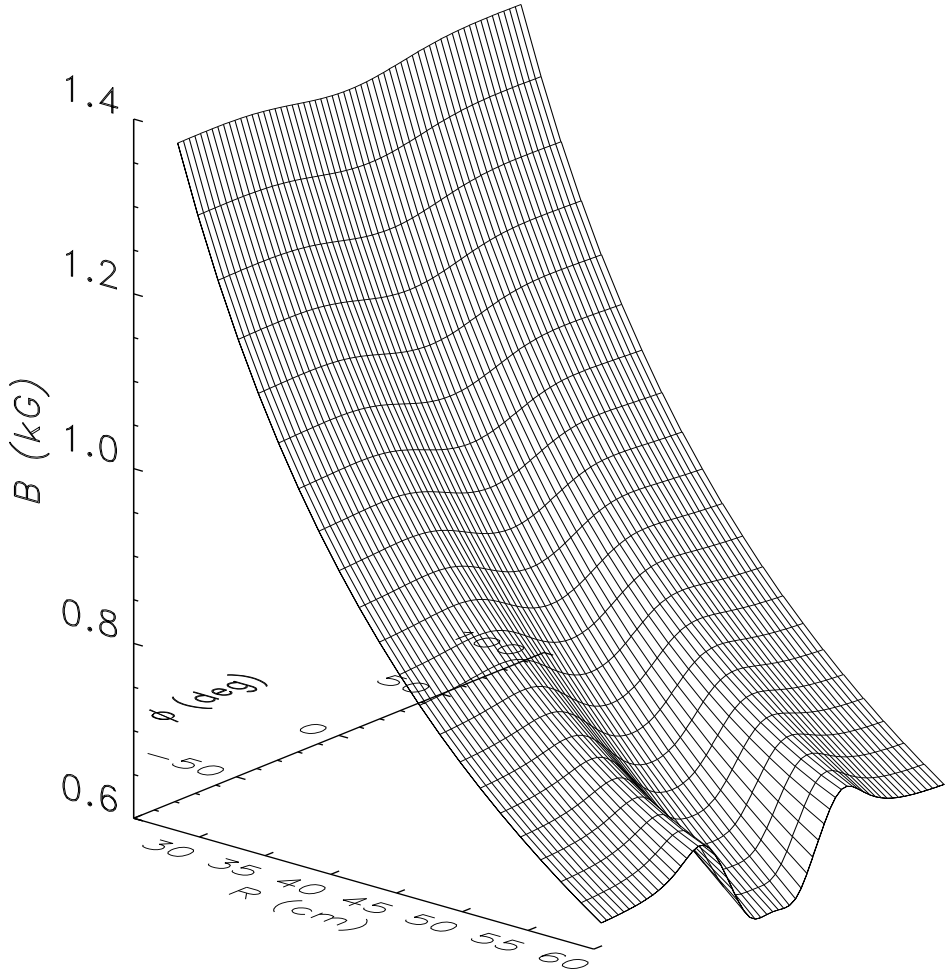

Figure 2.9: 3-dimensional plot of magnetic field strength at midplane with ripple coil *TypeII*. $I_{rip} = 5\,kA \cdot turn$.

Chapter 3

Calculation of Temperature Anisotropy

IN ORDER TO INCREASE the collisionless trapped electron population in the ripple region and to provide larger drifts, electrons must have large perpendicular speed compared to parallel speed, as discussed in Chapter 2. For this purpose, electron cyclotron resonance heating is appropriate. Preferential heating in the perpendicular direction means that the distribution function of resonant electrons is no longer isotropic. In this chapter, a quantitative calculation of temperature anisotropy driven by electron cyclotron resonance heating [1] is presented for a tokamak plasma in the presence of ripple transport of electrons. For the calculation of anisotropic temperatures of resonant (and thus, warm) electrons, the energy moments of bounce-averaged Fokker-Planck equation are solved assuming a moderate wave power and a constant quasilinear diffusion coefficient. The warm electron distribution function is assumed to be bi-Maxwellian, i.e., Maxwellian in perpendicular and parallel direction, respectively.

3.1 Kinetic Calculation of Temperature Anisotropy

For the sake of simplicity, the present analysis is confined to the cases with small inverse aspect ratio ($\epsilon = r/R_0$) and circular magnetic flux surfaces. Relativistic

[1] This work was done in collaboration with Dr. C.S. Chang.

and Doppler shift effects in the wave-particle interaction are neglected. We assume that the background particles are characterized by a Maxwellian distribution, and that the density of the warm particles is small compared to those of the background particles. We neglect Coulomb self-collisions between the warm particles when compared to the collisions of the warm particles against background particles. Plasma particles are divided into four different species; background cold electron (e) and ion (i) species, cold impurity species (I), and warm electron species (w) heated by the waves.

We write a model Fokker-Planck equation for the warm electrons in the form

$$\frac{\partial f}{\partial t} = \mathcal{C}(f) + \mathcal{Q}(f) + \mathcal{L}(f) + \mathcal{S}, \tag{3.1}$$

where $\mathcal{C}$ is the Coulomb collision operator, $\mathcal{Q}$ is the wave heating operator, $\mathcal{L}(f)$ represents the rapid loss of particles due to drift of ripple-trapped electrons, and $\mathcal{S}$ is the source of the warm electrons. If we use $\mathbf{v}_L$ to denote the vertical drift velocity

$$\mathbf{v}_L = \frac{m_e(v_\perp^2 + 2v_\parallel^2)}{2e} \frac{\nabla B \times \mathbf{B}}{B^3}, \tag{3.2}$$

then the ripple loss operator can be modeled as

$$\mathcal{L}(f) = -\chi \nabla \cdot (\mathbf{v}_L f),$$

where χ is the fraction of the ripple-trapped electrons. If we define a characteristic scale length L,

$$L^{-1} \equiv \frac{\nabla \cdot (\mathbf{v}_L f)}{v_L f},$$

we can write a characteristic drift loss rate due to ripple-trapping as

$$\nu_L = \frac{T_e}{e} \frac{1}{RB} \frac{1}{L}. \tag{3.3}$$

Then, the ripple loss operator can be expressed in the form

$$\mathcal{L}(f) = -\chi \, \frac{\nu_L}{v_e^2} \left(v_\perp^2 + 2v_\parallel^2\right) f. \tag{3.4}$$

The warm electrons are lost by the ripple-trapping effect, but they are continuously replenished from the cold background electrons by wave heating. We model the warm electron source term as

$$\mathcal{S} = \eta\, f_M, \tag{3.5}$$

where f_M is the Maxwellian distribution function for the background electrons and η is a source coefficient. In steady-state, the loss and source will have to balance.

For efficient ripple-trapping, the electron collision frequency needs to be low. By requiring the effective Coulomb scattering rate ν_c/δ from the ripple well to be smaller than ν_L, we have

$$\frac{\nu_c R}{v_e} < \delta\, \frac{\rho_e}{L},$$

as shown in Ref. [Stringer, 1972] where ρ_e is the electron gyroradius. By rearranging the above equation, the critical warm electron energy above which the collisionless radial loss model holds can be obtained as

$$\begin{aligned} T_w &> T_{crit}\,, \\ T_{crit}(eV) &= \left[\frac{3.5\times 10^{11}}{\delta(\%)}\, L(m)\, R(m)\, n_e(10^{20}\, m^{-3})\, B(T)\right]^{2/5}. \end{aligned} \tag{3.6}$$

With typical CDX-U parameters ($n_e = 2\times 10^{18}\, m^{-3}$, $R = 0.35\, m$, $B = 0.1\, T$, and $\delta = 5\,\%$), the critical energy is $360\, eV$ if we take $L = 0.05\, m$.

Since electron cyclotron heating discriminates the perpendicular from the parallel direction, we need to consider the perpendicular and parallel energy separately. Energy conservation in steady-state then gives us two equations

$$\left\langle \int d^3v\, v_\perp^2 \left[\mathcal{C} - \chi\, \frac{\nu_L}{v_e^2}\left(v_\perp^2 + 2v_\parallel^2\right) f + \eta\, f_M + \mathcal{Q}\right](f)\right\rangle = 0, \tag{3.7}$$

$$\left\langle \int d^3v\, v_\parallel^2 \left[\mathcal{C} - \chi\, \frac{\nu_L}{v_e^2}\left(v_\perp^2 + 2v_\parallel^2\right) f + \eta\, f_M \qquad\right](f)\right\rangle = 0. \tag{3.8}$$

The parallel energy moment equation does not have a wave heating term. This is because we assume that the parallel wave number in the quasilinear operator is

small so that the particles are heated only in the perpendicular direction [Kennel and Engelmann, 1966].

The procedure to obtain solutions from Eqs. (3.7) and (3.8) when there is no ripple field has been shown in Ref. [Choe *et al.*, 1995a], and the same procedure will also be adopted here. In the present analysis, the (v, λ) coordinate system is chosen for particle velocity in which λ is a constant of motion and defined as

$$\lambda \equiv \frac{B_m}{B}\frac{v_\perp^2}{v^2},$$

where B_m is the magnetic field at the minimum Mod-B point. The Jacobian in these velocity coordinates is calculated to be

$$\int d^3v = \sum_\sigma \int \frac{\pi v^3}{|v_\parallel|}\frac{B}{B_m} d\lambda\, dv,$$

where $\sigma = v_\parallel/|v_\parallel|$.

In flux coordinates (ψ, θ, ζ), where ψ, θ, ζ are radial, poloidal, and toroidal coordinates, respectively, the flux surface average of a physical quantity g can be written as

$$\langle g \rangle = \frac{\int d\theta\, \mathcal{J}\, g}{\int d\theta\, \mathcal{J}}, \tag{3.9}$$

where the Jacobian for the flux coordinates is expressed as

$$\mathcal{J} = (\boldsymbol{\nabla}\psi \times \boldsymbol{\nabla}\theta \cdot \boldsymbol{\nabla}\zeta)^{-1}.$$

The bounce average is defined as

$$\{g\} = \frac{1}{\tau_b}\int \frac{\mathcal{J}B}{|v_\parallel|}\, d\theta\, g, \tag{3.10}$$

$$\tau_b = \int \frac{\mathcal{J}B\, d\theta}{|v_\parallel|}. \tag{3.11}$$

The bounce integral is taken between $-\pi \leq \theta \leq \pi$ for passing particles and $-\theta_t \leq \theta \leq \theta_t$ for trapped particles where θ_t is the poloidal angle of banana tips.

The integration in Eq. (3.7) and Eq. (3.8) involves a three-dimensional integral which can be reduced to a two-dimensional one by changing the order of integration and using the definitions for flux surface average and bounce average. In general, the flux surface average of a velocity integration of a physical quantity g in a strong B field can be reduced to a velocity integral if the bounce-averaged value of g is known [Chang *et al.*, 1991]:

$$\left\langle \int d^3v\, g \right\rangle = \frac{\pi}{B_m \int \mathcal{J} d\theta} \sum_{\sigma} \int d\lambda\, dv\, v^3\, \tau_b\, \{g\}. \tag{3.12}$$

In addition, since the integrand for a bounce time, τ_b, is proportional to $1/v_\parallel$, $\hat{\tau}_b\,(\equiv v\,\tau_b)$ is independent of v, but dependent on λ.

Using Eq. (3.12), Eqs. (3.7) and (3.8) can be expressed as

$$\int_0^1 d\lambda \int_0^\infty dv\, v^2\, \hat{\tau}_b \left\{ v_\perp^2\, \mathcal{C} \right\} (f) \;\; - (Loss)_\perp + (Source)_\perp + (Heating)_\perp = 0, \tag{3.13}$$

$$\int_0^1 d\lambda \int_0^\infty dv\, v^2\, \hat{\tau}_b \left\{ v_\parallel^2\, \mathcal{C} \right\} (f) \;\; - (Loss)_\parallel + (Source)_\parallel = 0, \tag{3.14}$$

where

$$(Heating)_\perp = \left(\frac{\pi}{B_m \int \mathcal{J} d\theta} \right)^{-1} \left\langle \int d^3v\, v_\perp^2\, \mathcal{Q}\,(f) \right\rangle, \tag{3.15}$$

$$(Loss)_\parallel^\perp = \frac{\nu_L}{v_e^2}\, \chi \int_0^1 d\lambda \int_0^\infty dv\, v^2\, \hat{\tau}_b \begin{bmatrix} \left\{ v_\perp^2 \left(v^2 + v_\parallel^2 \right) \right\} f \\ \left\{ v_\parallel^2 \left(v^2 + v_\parallel^2 \right) \right\} f \end{bmatrix}, \tag{3.16}$$

$$(Source)_\parallel^\perp = \eta \int_0^1 d\lambda\, \hat{\tau}_b \begin{bmatrix} \{ v_\perp^2 \} \\ \left\{ v_\parallel^2 \right\} \end{bmatrix} \int_0^\infty dv\, v^2 f_M. \tag{3.17}$$

The upper (lower) part in the loss and the source terms indicates the perpendicular (parallel) term. The above two equations (3.13) and (3.14) show the appropriate path of energy flow from the input wave to the resonant particles. The wave heating term, Eq. (3.15) represents the energy input from the wave and it is positive definite. The Coulomb scattering part represents transfer of energy to the background species by energy scattering and redistribution of it within the warm species by pitch angle scattering.

To estimate the anisotropic temperatures from Eqs. (3.13) and (3.14), a bi-Maxwellian distribution function (which is constant along field lines) is used for the warm particles:

$$f = f_N\left(\alpha_\perp^2, \alpha_\parallel^2\right) \cdot e^{-v^2\left(\frac{\lambda}{\alpha_\perp^2}+\frac{1-\lambda}{\alpha_\parallel^2}\right)} = f_N\, e^{-b\,(c-\lambda)\,\frac{v^2}{v_e^2}}, \tag{3.18}$$

where

$$b = \frac{s-1}{\alpha_\perp^2/v_e^2}, \qquad c = \frac{s}{s-1}, \qquad s = \frac{\alpha_\perp^2}{\alpha_\parallel^2} = \frac{T_\perp}{T_\parallel}.$$

Here, $kT_\perp (= m_e\alpha_\perp^2/2)$ and $kT_\parallel (= m_e\alpha_\parallel^2/2)$ are effective temperatures perpendicular and parallel to magnetic field lines, v_e is background electron thermal speed, and f_N is the normalization factor. We now evaluate each term in Eqs. (3.13) and (3.14) separately.

3.1.1 Coulomb collision term

The Coulomb collision operator for warm electrons is a combination of pitch angle operator ($\mathcal{C}_\xi$) and energy scattering operator ($\mathcal{C}_\epsilon$) [Hinton, 1983]:

$$\mathcal{C}(f) = \mathcal{C}_\xi(f) + \mathcal{C}_\epsilon(f),$$

where

$$\mathcal{C}_\xi(f) = \frac{1}{2}\,\nu_\xi^{w/b}\,\frac{\partial}{\partial\xi}\left(1-\xi^2\right)\frac{\partial}{\partial\xi}\,f, \tag{3.19}$$

$$\mathcal{C}_\epsilon(f) = \frac{1}{v^2}\,\frac{\partial}{\partial v}\,v^2\,\nu_\epsilon^{w/b}\left(vf + \frac{kT_b}{m_w}\frac{\partial f}{\partial v}\right), \tag{3.20}$$

$$\nu_\xi^{w/b} = \nu_{\xi 0}\left(\frac{v_b}{v}\right)^3 \phi_1\left(\frac{v}{v_b}\right),$$

$$\nu_\epsilon^{w/b} = \nu_{\epsilon 0}\left(\frac{v_b}{v}\right)^3 \phi_2\left(\frac{v}{v_b}\right),$$

$$\nu_{\xi 0} = \frac{3\sqrt{\pi}}{4}\left(\frac{m_b}{m_w}\right)^2 \frac{1}{\tau_{c,b}},$$

$$\nu_{\epsilon 0} = \frac{3\sqrt{\pi}}{4}\,\frac{m_b}{m_w}\,\frac{1}{\tau_{c,b}},$$

$$
\begin{aligned}
\frac{1}{\tau_{c,b}} &= \frac{4\sqrt{2\pi}\, n_b\, Z_b^2\, Z_w^2\, e^4\, ln\Lambda}{3\sqrt{m_b}\,(kT_b)^{3/2}}, \\
\phi_1(u) &= \left(1 - \frac{1}{2u^2}\right) Erf(u) + \frac{e^{-u^2}}{\sqrt{\pi}\, u}, \\
\phi_2(u) &= Erf(u) - \frac{2}{\sqrt{\pi}} u e^{-u^2}, \\
Erf(u) &= \frac{2}{\sqrt{\pi}} \int_0^u e^{-y^2}\, dy.
\end{aligned}
$$

Here, super/subscripts w and b denote warm and background particles ($b = e, i, I$); v_b is the thermal velocity of the background particles; T_b is the background particle temperature; Z_w and Z_b are the charge numbers of warm and background particles; m_w and m_b are masses of warm and background particles respectively; $\xi = v_\parallel / v$; and $\tau_{c,b}$ is the Coulomb collision time at background temperature. The functions, $\phi_1(u)$ and $\phi_2(u)$ become unity when $u \gg 1$, and their asymptotic forms for $u \ll 1$ are

$$
\begin{aligned}
\phi_1(u) &\approx \frac{4}{3\sqrt{\pi}}\, u, \\
\phi_2(u) &\approx \frac{4}{3\sqrt{\pi}}\, u^3.
\end{aligned}
$$

Since the resonant particles are electrons ($m_w = m_e$), the pitch angle scattering of the warm electrons by background electrons is comparable to that by cold ions unless Z_{eff} is very large:

$$
\frac{\nu_\xi^{w/e}}{\nu_\xi^{w/i} + \nu_\xi^{w/I}} \approx \frac{1}{Z_{eff}}\, \phi_1\left(\frac{v}{v_e}\right) \sim \frac{1}{Z_{eff}},
$$

and $\phi_1(u)$ is in the range of $0.6 \leq \phi_1(u) \leq 1$ for $u = \dfrac{v}{v_e} \geq 1$. Thus, the two contributions should be considered equally in calculating the pitch angle scattering. For the energy scattering operator, the contribution from the background electrons is dominant over that from the cold ions by the ion-electron mass ratio,

$$
\frac{\nu_\epsilon^{w/e}}{\nu_\epsilon^{w/i}} \approx \frac{1}{Z_{eff}} \left(\frac{m_i}{m_e}\right) \phi_2\left(\frac{v}{v_e}\right) \gg 1.
$$

since $\phi_2(u) \sim \mathcal{O}(1)$. Thus, the ion term can be ignored in the warm electron energy scattering operator.

Therefore, the pitch angle scattering and the energy scattering characteristic frequencies can be simplified to be

$$\begin{aligned} \nu_\xi^{w/b} &\approx \nu_0 \, \frac{1}{u^3} \, (Z_{eff} + \phi_1(u)) \;\equiv\; \nu_\xi, \\ \nu_\epsilon^{w/b} &\approx \nu_0 \, \frac{1}{u^3} \, \phi_2(u) \;\equiv\; \nu_\epsilon, \end{aligned}$$

where

$$\nu_0 = \frac{\sqrt{2}\pi \, n_e \, e^4 \, ln\Lambda}{\sqrt{m_e} \, (kT_e)^{3/2}}. \tag{3.21}$$

The first term in ν_ξ (which contains Z_{eff}) is from the scattering of warm electrons on background ions, and the second term is from scattering on background electrons.

The bounced-averaged Coulomb collision terms in Eq. (3.13) and Eq. (3.14) can be written as

$$\begin{aligned} \{v_\perp^2 \, \mathcal{C}\}\,(f) &= \{v_\perp^2 \, \mathcal{C}_\xi\}\,(f) + \{v_\perp^2 \, \mathcal{C}_\epsilon\}\,(f), \\ \left\{v_\parallel^2 \, \mathcal{C}\right\}(f) &= \left\{v_\parallel^2 \, \mathcal{C}_\xi\right\}(f) + \left\{v_\parallel^2 \, \mathcal{C}_\epsilon\right\}(f). \end{aligned}$$

The energy scattering operator $\mathcal{C}_\epsilon(f)$ can be taken out of the bounce integral since it is a function of v only and, thus, constant of motion,

$$\left\{v_\perp^2 \, \mathcal{C}_\epsilon\right\}(f) \;=\; \left\{v_\perp^2\right\} \mathcal{C}_\epsilon(f), \tag{3.22}$$

$$\left\{v_\parallel^2 \, \mathcal{C}_\epsilon\right\}(f) \;=\; \left\{v_\parallel^2\right\} \mathcal{C}_\epsilon(f). \tag{3.23}$$

The pitch angle scattering operator, Eq. (3.19), can be expressed in terms of the new coordinates (v, λ) as

$$\mathcal{C}_\xi = 2 \, \nu_\xi \frac{B_m}{B} \, \xi \, \frac{\partial}{\partial \lambda} \, \lambda \, \xi \, \frac{\partial}{\partial \lambda},$$

where $\xi = \sigma \sqrt{1 - \frac{B}{B_m} \lambda}$ and the 90° Coulomb collision frequency ν_ξ is a function of v only. Using the relationships,

$$\frac{v_\parallel^2}{v^2} = \xi^2 = 1 - \frac{B}{B_m} \lambda, \qquad \text{and} \qquad \frac{v_\perp^2}{v^2} = 1 - \xi^2 = \frac{B}{B_m} \lambda,$$

we obtain the bounce averages of $v_\perp^2\,\mathcal{C}_\xi(f)$ and $v_\parallel^2\,\mathcal{C}_\xi(f)$ as

$$\hat{\tau}_b\left\{v_\perp^2\,\mathcal{C}_\xi(f)\right\} = 2\,\nu_\xi\,v^2\,\lambda\left[-\hat{\tau}_b\,\frac{1}{2}\,\frac{\partial f}{\partial\lambda} + \frac{\hat{\tau}_b}{v^2}\left\{v_\parallel^2\right\}\left(\frac{\partial}{\partial\lambda}\,\lambda\,\frac{\partial f}{\partial\lambda} + \frac{1}{2}\,\frac{\partial f}{\partial\lambda}\right)\right], \tag{3.24}$$

$$\hat{\tau}_b\left\{v_\parallel^2\,\mathcal{C}_\xi(f)\right\} = 2\,\nu_\xi\,v^2\left[\frac{\hat{\tau}_b}{v^2}\left\{\frac{B_m}{B}v_\parallel^2\right\}\frac{\partial}{\partial\lambda}\,\lambda\,\frac{\partial f}{\partial\lambda} - \frac{\hat{\tau}_b}{v^2}\left\{v_\parallel^2\right\}\,\lambda\left(\frac{\partial}{\partial\lambda}\,\lambda\,\frac{\partial f}{\partial\lambda} + \frac{1}{2}\,\frac{\partial f}{\partial\lambda}\right)\right]. \tag{3.25}$$

In order to continue the calculation, we need to know the quantities, $\hat{\tau}_b$, $\{v_\perp^2\}$, $\left\{v_\parallel^2\right\}$, and $\frac{\hat{\tau}_b}{v^2}\left\{\frac{B_m}{B}v_\parallel^2\right\}$ in Eqs. (3.22) – (3.25). The bounce time (transit time for passing particles) is calculated to be [Chang and Colestock, 1990]

$$\hat{\tau}_b \equiv v\,\tau_b = \begin{cases} \dfrac{2}{\pi}\sqrt{1+2x}\,K(x) & (x<1), \\[2ex] \dfrac{2}{\pi}\sqrt{\dfrac{1+2x}{x}}\,K\left(\dfrac{1}{x}\right) & (x>1), \end{cases} \tag{3.26}$$

where $K(x)$ is the complete elliptic integral of the first kind with modulus x, and the variable x is defined as

$$x = \frac{2\epsilon}{1-\epsilon}\,\frac{\lambda}{1-\lambda}. \tag{3.27}$$

$x=1$ describes the boundary between trapped and passing particles, with $x>1$ describing the trapped particles. For numerical evaluations in this work, we choose $\epsilon=1/5$. As can be seen in Fig. 3.1(a), $\hat{\tau}_b$ has a singularity at the trapped-passing boundary. In order to avoid numerical problems associated with this singularity, we replace $\hat{\tau}_b$ with a well behaved function $V_{tt}(\lambda)$. Using the relationship between x and λ in Eq. (3.27), the smoothed function, $V_{tt}(\lambda)$ is obtained by fitting $\hat{\tau}_b$ based on polynomials of λ and is plotted with dotted line.

The functions $\{v_\perp^2\}$ and $\left\{v_\parallel^2\right\}$ are calculated in a similar manner as calculating $\hat{\tau}_b$ and smoothed in order to avoid singularities:

$$\frac{\hat{\tau}_b}{v^2}\,\left\{v_\parallel^2\right\} = \begin{cases} \dfrac{2}{\pi}\dfrac{1}{\sqrt{1+2x}}\,E(x) & (x<1), \\[2ex] \dfrac{2}{\pi}\sqrt{\dfrac{x}{1+2x}}\left[E\left(\dfrac{1}{x}\right) - \left(1-\dfrac{1}{x}\right)\,K\left(\dfrac{1}{x}\right)\right] & (x>1), \end{cases} \tag{3.28}$$

$$\approx V_{tl}(\lambda),$$

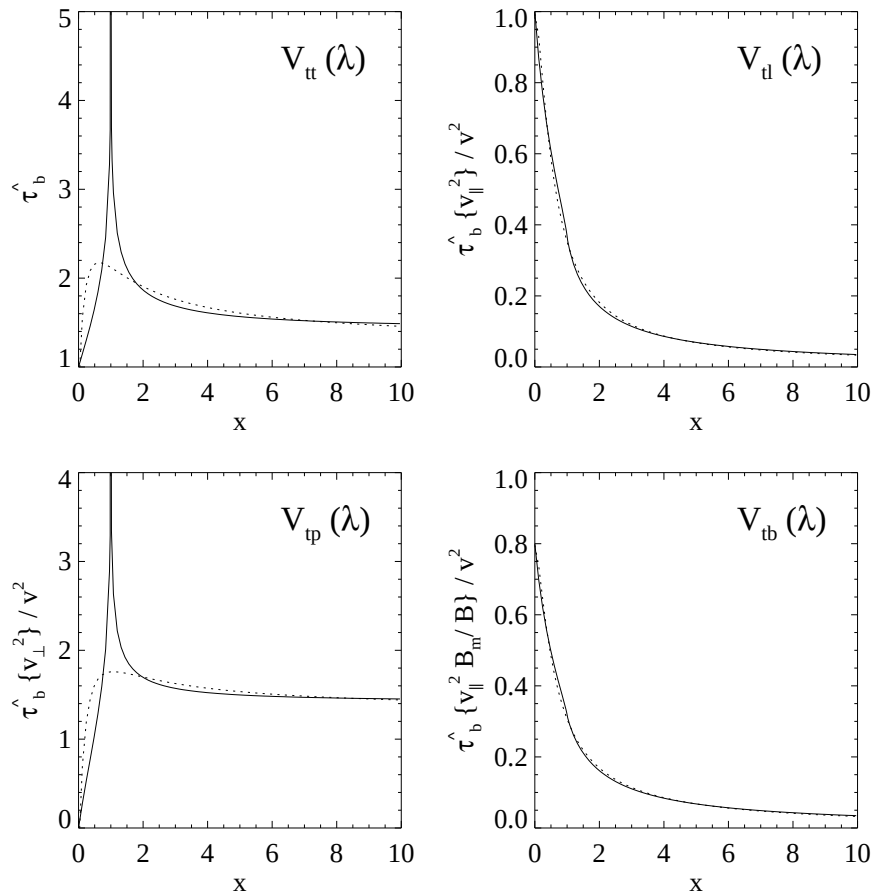

Figure 3.1: Solid lines show the bounce-averaged quantities, $\hat{\tau}_b$, $\frac{\hat{\tau}_b}{v^2}\left\{v_\parallel^2\right\}$, $\frac{\hat{\tau}_b}{v^2}\left\{v_\perp^2\right\}$, $\frac{\hat{\tau}_b}{v^2}\left\{\frac{B_m}{B}v_\parallel^2\right\}$, which are to be integrated over λ. In order to avoid the divergence at the trapped-passing boundary ($x = 1$), the functions are fitted by polynomials of λ.

$$\frac{\hat{\tau}_b}{v^2}\left\{v_\perp^2\right\} = \begin{cases} \dfrac{2}{\pi}\sqrt{1+2x}\,K(x) - \dfrac{2}{\pi}\dfrac{1}{\sqrt{1+2x}}\,E(x) & (x<1), \\ \dfrac{2}{\pi}\sqrt{\dfrac{1+2x}{x}}\,K\left(\dfrac{1}{x}\right) - \dfrac{2}{\pi}\sqrt{\dfrac{x}{1+2x}}\left[E\left(\dfrac{1}{x}\right) - \left(1-\dfrac{1}{x}\right)K\left(\dfrac{1}{x}\right)\right] & (x>1), \end{cases}$$

$$\approx V_{tp}(\lambda), \tag{3.29}$$

where $E(x)$ is the complete elliptic integral of the second kind. By a similar procedure, $\dfrac{\hat{\tau}_b}{v^2}\left\{\dfrac{B_m}{B}v_\parallel^2\right\}$ is obtained, using an ϵ-expansion of $\dfrac{B_m}{B}$ up to the first order in ϵ,

$$\frac{\hat{\tau}_b}{v^2}\left\{\frac{B_m}{B}v_\parallel^2\right\} = \begin{cases} \dfrac{2}{\pi}\dfrac{1}{\sqrt{1+2x}}\left[E(x) - \dfrac{\pi}{10}\,{}_2F_1\left(-\dfrac{1}{2},\dfrac{3}{2},2,x\right)\right] & (x<1), \\ \dfrac{2}{\pi}\sqrt{\dfrac{x}{1+2x}}\left[E\left(\dfrac{1}{x}\right) - \left(1-\dfrac{1}{x}\right)K\left(\dfrac{1}{x}\right) - \dfrac{\pi}{40}\dfrac{1}{x^2}\,{}_2F_1\left(\dfrac{1}{2},\dfrac{3}{2},3,\dfrac{1}{x}\right)\right] & (x>1), \end{cases}$$

$$\approx V_{tb}(\lambda), \tag{3.30}$$

where F is the hypergeometric function. Since the bounce time, $\hat{\tau}_b$, diverges at the trapped-passing boundary, $\left\{v_\parallel^2\right\}$ and $\left\{\dfrac{B_m}{B}v_\parallel^2\right\}$ approach 0 as expected.

The bounce-averaged quantities, Eqs. (3.26), (3.28), (3.29), and (3.30) are depicted in Fig. 3.1 with solid lines. Their fitted functions of the form with constants c_0, c_1, c_2, and c_3,

$$V_{tt},\, V_{tl},\, V_{tp},\, V_{tb} = c_0 + c_1\,\lambda + c_2\,\lambda^2 + c_3\,\lambda^3 \tag{3.31}$$

are also plotted with dotted lines. With the help of these smoothed functions, Eqs. (3.22) – (3.25) become

$$\hat{\tau}_b\left\{v_\perp^2\,\mathcal{C}_\xi(f)\right\} = \frac{2\,\nu_0\,v_e^2}{u}\left(Z_{eff} + \phi_1(u)\right)\lambda\left[-V_{tt}(\lambda)\,\frac{1}{2}\frac{\partial f}{\partial\lambda} + V_{tl}(\lambda)\left(\frac{\partial}{\partial\lambda}\lambda\frac{\partial f}{\partial\lambda} + \frac{1}{2}\frac{\partial f}{\partial\lambda}\right)\right], \tag{3.32}$$

$$\hat{\tau}_b\left\{v_\parallel^2\,\mathcal{C}_\xi(f)\right\} = \frac{2\,\nu_0\,v_e^2}{u}\left(Z_{eff} + \phi_1(u)\right)\left[V_{tb}(\lambda)\,\frac{\partial}{\partial\lambda}\lambda\frac{\partial f}{\partial\lambda} - V_{tl}(\lambda)\,\lambda\left(\frac{\partial}{\partial\lambda}\lambda\frac{\partial f}{\partial\lambda} + \frac{1}{2}\frac{\partial f}{\partial\lambda}\right)\right], \tag{3.33}$$

$$\hat{\tau}_b\left\{v_\perp^2\,\mathcal{C}_\epsilon(f)\right\} = \nu_0\,v_e^2\,V_{tp}(\lambda)\,\frac{\partial}{\partial u}\phi_2(u)\left(f + \frac{1}{2u}\frac{\partial f}{\partial u}\right), \tag{3.34}$$

$$\hat{\tau}_b\left\{v_\parallel^2\,\mathcal{C}_\epsilon(f)\right\} = \nu_0\,v_e^2\,V_{tl}(\lambda)\,\frac{\partial}{\partial u}\phi_2(u)\left(f + \frac{1}{2u}\frac{\partial f}{\partial u}\right). \tag{3.35}$$

where $u = v/v_e$.

3.1.2 Wave heating term

For the quasilinear operator $\mathcal{Q}(f)$, we use

$$\begin{aligned} \mathcal{Q}(f) &= \frac{1}{v_\perp}\frac{\partial}{\partial v_\perp} v_\perp \mathcal{D}\,\frac{\partial f}{\partial v_\perp}, \\ \mathcal{D} &= \sum_l \mathcal{D}_0\ \delta(\omega - l\Omega), \end{aligned} \tag{3.36}$$

where ω is the wave frequency and Ω is the electron cyclotron frequency. Since the Doppler shift effect in $\mathcal{Q}$ is assumed to be negligible ($k_\parallel v_\parallel \simeq 0$), the particle heating is in the perpendicular direction only and, thus, there is no direct resonance heating term in the parallel energy moment equation [Kennel and Engelmann, 1966]. The delta function in the quasilinear diffusion coefficient $\mathcal{D}$ requires that the particles should be resonant somewhere along their orbits to have a nonvanishing $\mathcal{D}$, and its relation to the absorbed wave power will be shown later in this chapter.

Due to conservation of magnetic moment along the guiding center motion in a toroidal system, however, the perpendicular heating at the resonance location appears differently along the magnetic field line, resulting in a varying degree of the temperature anisotropy along the magnetic field line. In the present analysis, the amount of anisotropy is calculated at the resonance point for the sake of simplicity.

In order to manipulate the delta function in $\mathcal{D}$, we follow Ref. [Stix, 1975] and expand the resonance condition $l\Omega - \omega = 0$ near the resonance layer whose poloidal angle is given by θ_R,

$$l\Omega - \omega \simeq l\,\left.\frac{d\Omega}{d\theta}\right|_{\theta=\theta_R} \cdot (\theta - \theta_R) = G\,\cdot(\theta - \theta_R),$$

where the frequency, G, including the geometrical factor is,

$$G = \omega\epsilon\,\frac{sin\,\theta_R}{1 - \epsilon\,cos\,\theta_R},$$

and $B = \dfrac{B_0}{1+\epsilon\, cos\,\theta}$ is used. If $\mathcal{D}_0$ is assumed to be constant [Chang and Colestock, 1990] with respect to v and λ, the velocity integral of $v_\perp^2\,\mathcal{Q}(f)$ becomes

$$\int d^3v\, v_\perp^2\,\mathcal{Q}(f) = \frac{4\mathcal{D}_0}{G}\int d^3v\;\; f|_{\theta=\theta_R}.$$

Then, the heating term, Eq. (3.15), is changed into

$$\left\langle \int d^3v\;\, v_\perp^2\,\mathcal{Q}(f)\right\rangle = \frac{4\mathcal{D}_0}{G}\,\frac{\pi}{B_m\int \mathcal{J}\,d\theta}\int d\lambda\, dv\, v^2\,\hat{\tau}_b\;\; f|_{\theta=\theta_R}, \tag{3.37}$$

and

$$(Heating)_\perp = \frac{4\mathcal{D}_0}{G}\, v_e^3\int_0^1 d\lambda\; V_{tt}(\lambda)\int_0^\infty du\; u^2\, f. \tag{3.38}$$

3.1.3 Loss and source terms

The ripple-trapped particle fraction, χ, with anisotropic distribution function (see Fig. 3.2) is given as

$$\chi = \frac{\left\langle \int_{ripple\ space} d^3v\; f\right\rangle}{\left\langle \int_{whole\ space} d^3v\; f\right\rangle},$$

and it is a function of ripple strength, δ, and temperature ratio, s. The above integrals can be expressed in terms of (v,λ) and by using Eq. (3.18) for f, yielding

$$\chi\,(s,\delta) = \frac{\displaystyle\int_{\lambda_{min}}^{\lambda_{max}} d\lambda\,\frac{\hat{\tau}_b(\lambda)}{\left[s-\lambda(s-1)\right]^{3/2}}}{\displaystyle\int_0^{\lambda_{max}} d\lambda\,\frac{\hat{\tau}_b(\lambda)}{\left[s-\lambda(s-1)\right]^{3/2}}}. \tag{3.39}$$

The upper and lower limit for λ-integral are $\lambda_{max} = B_m/B_{min}$ and $\lambda_{min} = B_m/B_{max}$ where B_{max} and B_{min} are local maximum and minimum magnetic fields provided by external ripple coils. In general, λ_{max} and λ_{min} are functions of inverse aspect ratio, ϵ, and ripple strength, δ. In order to carry out more detailed calculation, we

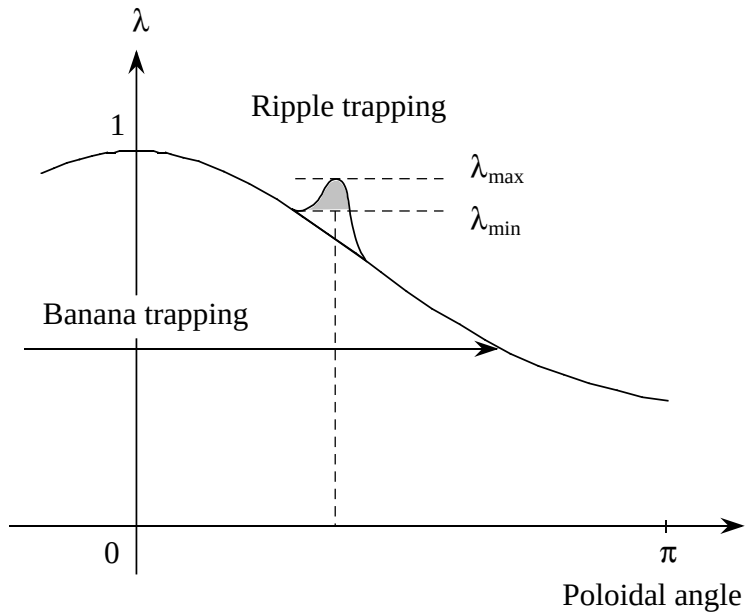

Figure 3.2: Region of λ for ripple trapping.

assume that the field ripple is located on top of the plasma where $R = R_0$, and the ripple fields provide a magnetic well. Then $B_{max} \simeq B_0$, and λ_{max} and λ_{min} become

$$\lambda_{min} \simeq \frac{B_m}{B_0} \simeq (1-\epsilon),$$
$$\lambda_{max} \simeq \frac{B_m}{B_0}\frac{B_{max}}{B_{min}} \simeq (1-\epsilon)\left(\frac{1+\delta}{1-\delta}\right).$$

The evaluated ripple-trapped fraction is plotted in Fig. 3.3 with various values of ripple strength, δ.

To complete the loss term, Eq. (3.16), we use

$$\left\{v_\perp^2 v_\parallel^2\right\} = v^2\left\{v_\parallel^2\right\} - \left\{v_\parallel^4\right\},$$

and $\left\{v_\parallel^4\right\}$ is also smoothed to be a polynomial function of λ as

$$V_{tl4}(\lambda) = \frac{\hat{\tau}_b}{v^4}\left\{v_\parallel^4\right\}.$$

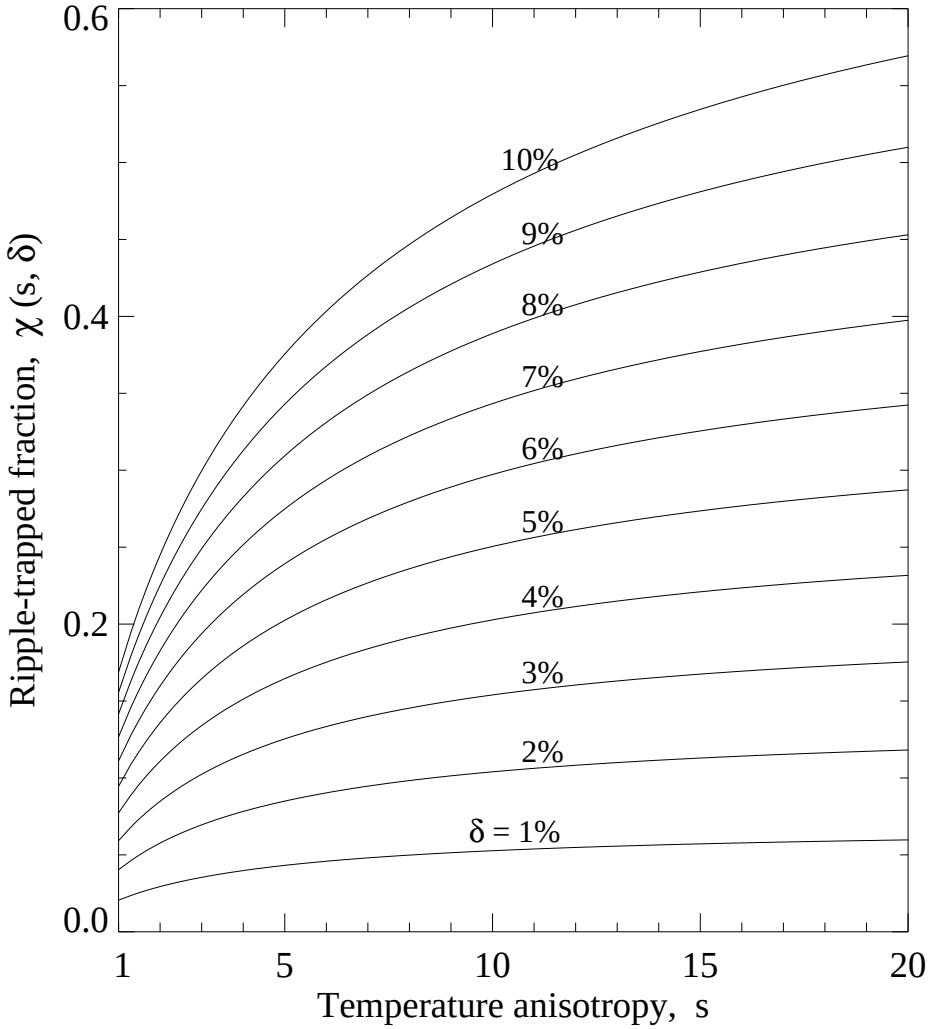

Figure 3.3: The fraction of trapped electrons in the magnetic ripple fields as a function of temperature anisotropy, s, and ripple strength, δ.

Finally, the loss term is expressed as

$$(Loss)_{\parallel}^{\perp} = \nu_L\, v_e^5\ \chi(s,\delta)\ \int_0^1 d\lambda \begin{bmatrix} V_{tp}(\lambda) + V_{tl}(\lambda) - V_{tl4}(\lambda) \\ V_{tl}(\lambda) + V_{tl4}(\lambda) \end{bmatrix} \int_0^\infty du\, u^6 f. \quad (3.40)$$

The particle source coefficient η compensating the drift loss is determined by the density conservation. In steady-state, we obtain

$$\eta = \frac{\nu_L}{n_e v_e^2}\, \chi \left\langle \int d^3v\ \left(v^2 + v_{\parallel}^2\right) f \right\rangle,$$

and by Eq. (3.12), η is given as

$$\eta = \frac{\nu_L}{n_e v_e^2}\, v_e^5\ \chi \int_0^1 d\lambda\, (V_{tt}(\lambda) + V_{tl}(\lambda)) \int_0^\infty du\, u^4 f. \quad (3.41)$$

Using η in the above form, the source term becomes

$$\begin{aligned} (Source)_{\parallel}^{\perp} &= \eta \int_0^1 d\lambda \begin{bmatrix} V_{tp}(\lambda) \\ V_{tl}(\lambda) \end{bmatrix} \int_0^\infty dv\, v^4 f_m, \quad (3.42) \\ &= \nu_L\, v_e^5\ \chi(s,\delta) \cdot \frac{3}{8\pi} \begin{bmatrix} 1.244 \\ 0.556 \end{bmatrix} \int_0^1 d\lambda\, (V_{tt}(\lambda) + V_{tl}(\lambda)) \int_0^\infty du\, u^4 f. \end{aligned}$$

3.1.4 Evaluation of the temperature anisotropy

Now, the various terms obtained [Coulomb collision terms, Eqs. (3.32) - (3.35); wave heating term, Eq. (3.38); loss term, Eq. (3.40); and source term, Eq. (3.42)] are substituted into the two equations (3.13) and (3.14) with the warm electron distribution function given by Eq. (3.18). After rearrangements, we get two simultaneous equations to be solved for two unknowns, the temperature ratio s, and the perpendicular energy $m_e\alpha_\perp^2/2$:

$$-\left(T_{pa,e}^{\perp} + Z_{eff}\, T_{pa,i}^{\perp}\right) + \left(-T_{dr,e}^{\perp} + T_{df,e}^{\perp}\right) + \left(\frac{\nu_L}{\nu_0}\right) \chi(s,\delta)\ \left(-T_L^{\perp} + T_S^{\perp}\right) + \mathcal{H}_\perp = 0, \quad (3.43)$$

$$\left(T_{pa,e}^{\parallel} + Z_{eff}\, T_{pa,i}^{\parallel}\right) + \left(-T_{dr,e}^{\parallel} + T_{df,e}^{\parallel}\right) + \left(\frac{\nu_L}{\nu_0}\right) \chi(s,\delta)\ \left(-T_L^{\parallel} + T_S^{\parallel}\right) = 0. \quad (3.44)$$

where

$$\mathcal{H}_\perp = d_e \int_0^1 d\lambda\, V_{tt}(\lambda) \int_0^\infty du\, u^2\, f, \tag{3.45}$$

$$d_e = \frac{4\mathcal{D}_0}{G}\,\frac{1}{\nu_0 v_e^2}, \tag{3.46}$$

$$T_{pa,e}^\perp = T_{11} - T_{12}, \tag{3.47}$$

$$T_{pa,i}^\perp = T_{13} - T_{14}, \tag{3.48}$$

$$T_{pa,e}^\parallel = T_{21} - T_{22}, \tag{3.49}$$

$$T_{pa,i}^\parallel = T_{23} - T_{24}, \tag{3.50}$$

$$T_{dr,e}^\perp = 2\int_0^1 d\lambda\, V_{tp}(\lambda) \int_0^\infty du\, u\, \phi_2(u)\, f, \tag{3.51}$$

$$T_{df,e}^\perp = 2b\int_0^1 d\lambda\, V_{tp}(\lambda)\,(c-\lambda) \int_0^\infty du\, u\, \phi_2(u)\, f, \tag{3.52}$$

$$T_{dr,e}^\parallel = 2\int_0^1 d\lambda\, V_{tl}(\lambda) \int_0^\infty du\, u\, \phi_2(u)\, f, \tag{3.53}$$

$$T_{df,e}^\parallel = 2b\int_0^1 d\lambda\, V_{tl}(\lambda)\,(c-\lambda) \int_0^\infty du\, u\, \phi_2(u)\, f, \tag{3.54}$$

$$\begin{bmatrix} T_L^\perp \\ T_L^\parallel \end{bmatrix} = \int_0^1 d\lambda \begin{bmatrix} V_{tp}(\lambda) + V_{tl}(\lambda) - V_{tl4}(\lambda) \\ V_{tl}(\lambda) + V_{tl4}(\lambda) \end{bmatrix} \int_0^\infty du\, u^6 f, \tag{3.55}$$

$$\begin{bmatrix} T_S^\perp \\ T_S^\parallel \end{bmatrix} = \frac{3}{8\pi} \begin{bmatrix} 1.244 \\ 0.556 \end{bmatrix} \int_0^1 d\lambda\, (V_{tt}(\lambda) + V_{tl}(\lambda)) \int_0^\infty du\, u^4 f, \tag{3.56}$$

$$\begin{aligned}
T_{11} &= \int_0^1 d\lambda\, \lambda\, V_{tt}(\lambda) \int_0^\infty du\, u\, \phi_1(u)\, \frac{\partial f}{\partial \lambda}, \\
T_{12} &= 2\int_0^1 d\lambda\, \lambda\, V_{tl}(\lambda) \int_0^\infty du\, u\, \phi_1(u) \left(\frac{\partial}{\partial\lambda}\,\lambda\,\frac{\partial f}{\partial\lambda} + \frac{1}{2}\,\frac{\partial f}{\partial\lambda}\right), \\
T_{13} &= \int_0^1 d\lambda\, \lambda\, V_{tt}(\lambda) \int_0^\infty du\, u\, \frac{\partial f}{\partial \lambda}, \\
T_{14} &= 2\int_0^1 d\lambda\, \lambda\, V_{tl}(\lambda) \int_0^\infty du\, u \left(\frac{\partial}{\partial\lambda}\,\lambda\,\frac{\partial f}{\partial\lambda} + \frac{1}{2}\,\frac{\partial f}{\partial\lambda}\right), \\
T_{21} &= 2\int_0^1 d\lambda\, \lambda\, V_{tb}(\lambda) \int_0^\infty du\, u\, \phi_1(u)\, \frac{\partial}{\partial\lambda}\,\lambda\,\frac{\partial f}{\partial\lambda}, \\
T_{22} &= T_{12}, \\
T_{23} &= 2\int_0^1 d\lambda\, \lambda\, V_{tb}(\lambda) \int_0^\infty du\, u\, \frac{\partial}{\partial\lambda}\,\lambda\,\frac{\partial f}{\partial\lambda}, \\
T_{24} &= T_{14},
\end{aligned}$$

$$b = \frac{s-1}{\alpha_\perp^2/v_e^2}, \qquad c = \frac{s}{s-1}, \tag{3.57}$$
$$\nu_0 = \frac{3\sqrt{\pi}}{4}\frac{1}{\tau_e}, \qquad \frac{1}{\tau_e} = \frac{4\sqrt{2\pi}\, n_e\, e^4\, ln\Lambda}{3\sqrt{m_e}\,(kT_e)^{3/2}}.$$

The first subscripts, pa, dr, and df indicate pitch angle, drag, and diffusion, respectively, and the second subscript after a comma denotes the species of background particles with which warm electrons collide. The integrals in Eqs. (3.47) - (3.56) are all positive definite since $b \geq 1$ and $c \geq 1$.

Using the definition of the warm particle density,

$$n_w = \langle\, n(\theta)\,\rangle = \left\langle \int d^3v\, f \right\rangle,$$

the absorbed wave power can be derived from Eq. (3.37),

$$\langle P_\perp \rangle = \frac{1}{2}\, m_e \left\langle \int d^3v\; v_\perp^2\, \mathcal{Q}(f) \right\rangle = \frac{m_e}{2}\,\frac{4\mathcal{D}_0}{G}\, n_w. \tag{3.58}$$

Therefore, the parameter, d_e which is a function of the wave power and warm particle density is expressed as

$$d_e = \frac{\langle P_\perp \rangle}{n_w\, kT_e\, \nu_0}. \tag{3.59}$$

Because of the functions $\phi_1(u)$ and $\phi_2(u)$, it is not straightforward to evaluate the integrals in Eqs. (3.43) and (3.44) by hand. Instead, we use the mathematical software, *Mathematica*^{TM} by *Wolfram Research, Inc.* [Wolfram, 1991] which has the capability of doing symbolic differentiation and integration.

Figure 3.4, obtained by solving Eqs. (3.43) and (3.44), depicts the perpendicular and parallel temperatures and their ratio as a function of d_e with various values of ν_L/ν_0, $Z_{eff} = 1$, and $\epsilon = 1/5$. As shown in Ref. [Choe *et al.*, 1995a], one important observation to point out here is that the warm electron temperatures run-away at $d_e \simeq 0.61$ in the absence of a loss mechanism for the tail electrons ($\nu_L/\nu_0 = 0$). This run-away effect is expected from the fact that the warm particle density, n_w, is kept constant as the wave power is increased. In addition, we used a Maxwellian assumption for the resonant species with no cooling mechanisms other

than collisions with the background electrons. The electron energy scattering rate, however, decreases with increasing energy ($\nu_\epsilon \propto v^{-3}$). Hence, for wave power above the run-away power (with which run-away occurs), the validity of the Maxwellian assumption is in doubt. In the presence of a ripple loss term ($\nu_L/\nu_0 \neq 0$), however, this run-away can be avoided. As ν_L/ν_0 increases, the slope of the temperatures at $d_e \simeq 0.61$ becomes smaller. This is because high energy electrons drift out of the region more quickly and thus warm electrons have less probability of becoming run-away electrons. Keeping ν_L/ν_0 fixed, a similar behavior can be found by increasing δ as in Fig. 3.5.

Figure 3.5 shows the effect of ripple strength on temperature anisotropy. Solid lines are obtained with $\delta = 1\,\%$ and dotted lines are with $\delta = 5\,\%$. As δ increases, more particles are trapped in the ripple region (Fig. 3.3) and thus the drift loss becomes larger, which results in less anisotropy.

Figures 3.6 through 3.8 show the calculated anisotropic temperatures for CDX-U case when $\nu_L/\nu_0 = 0.03$ and $\delta = 5\,\%$ with $Z_{eff} = 1, 2, 3, 4$. In general, the behavior is similar to the ion case in the presence of ion cyclotron resonance heating [Choe *et al.*, 1995a]. From these figures, several comments can be made. First, the greater the impurity level in a plasma (larger Z_{eff}), the higher the $T_\parallel$ (and lower $T_\perp$), and thus less anisotropy is obtained. This is because the pitch angle scattering term increases with Z_{eff}, resulting in a more effective spreading of warm electron energy to the parallel direction. Second, as depicted in Fig. 3.7 (b), the parallel temperature reaches a maximum value and decreases with d_e. This is because when the wave power is large, the power transferred from the perpendicular to the parallel direction decreases:

$$P_\parallel \sim \nu_\xi\, k \left(T_\perp - T_\parallel\right) \propto \frac{1}{\sqrt{kT_\perp}},$$

where ν_ξ is proportional to $1/v^3$. Third, the parameter d_e is

$$d_e \propto \frac{\langle P_\perp \rangle}{n_w} \frac{\sqrt{m_e k T_e}}{n_e},$$

so that higher anisotropy can be expected at higher background temperature or smaller background density. Fourth, the ratio of perpendicular and parallel temperature reaches as high as 15 and no solution can be obtained beyond a certain

value of d_e, which suggest that there exists a critical wave power above which our bi-Maxwellian picture does not hold. In order to extend the present analysis above this critical power, a better description of the distribution for warm species may be necessary.

The present study shows that the temperature anisotropy can be made quite large by putting the electron cyclotron resonance layer in the ripple region. Thus, the ripple-trapped fraction of the warm electrons can be significant. For example, for $\delta = 5\,\%$ and $T_\perp/T_\parallel = 10$, Fig. 3.3 yields $\chi \approx 25\,\%$. A significant number of warm electrons can drift to smaller minor radial positions to create a negative electrostatic potential (ripple injection).

3.2 Summary

Since electron cyclotron resonance heating is utilized in an electron ripple injector, it is desirable to investigate one of the characteristics of this heating, i.e., preferential heating of electrons in the direction perpendicular to the magnetic field. In this chapter, we have derived a method for calculating the temperature anisotropy produced by electron cyclotron resonance heating in the presence of ripple injection. In order to estimate anisotropic temperatures, we solved the perpendicular and parallel energy moments of the Fokker-Planck equation including heat transport due to the electron ripple injection. A bi-Maxwellian model has been used for the warm electron distribution function and a full form of Coulomb collision operator was used. By solving two equations (3.43) and (3.44) simultaneously, the temperature anisotropy of the warm electrons is obtained. According to the results, the anisotropy can be quite large ($T_\perp/T_\parallel \leq 15$ as shown in Fig. 3.8) with a moderate input wave power and a reasonable ripple strength.

As a passing remark, due to the temperature anisotropy in a tokamak plasma, a poloidal electrostatic potential variation can be generated. Since cyclotron resonance heating preferentially increases the perpendicular energy of resonant particles, this leads to more banana trapping at the outboard side where the magnetic field is lower, causing an imbalance of spatial charge on a magnetic flux surface. In order to maintain charge neutrality, an electrostatic potential with an in-out poloidal asymmetry should build-up. As is shown, since the temperature anisotropy can be

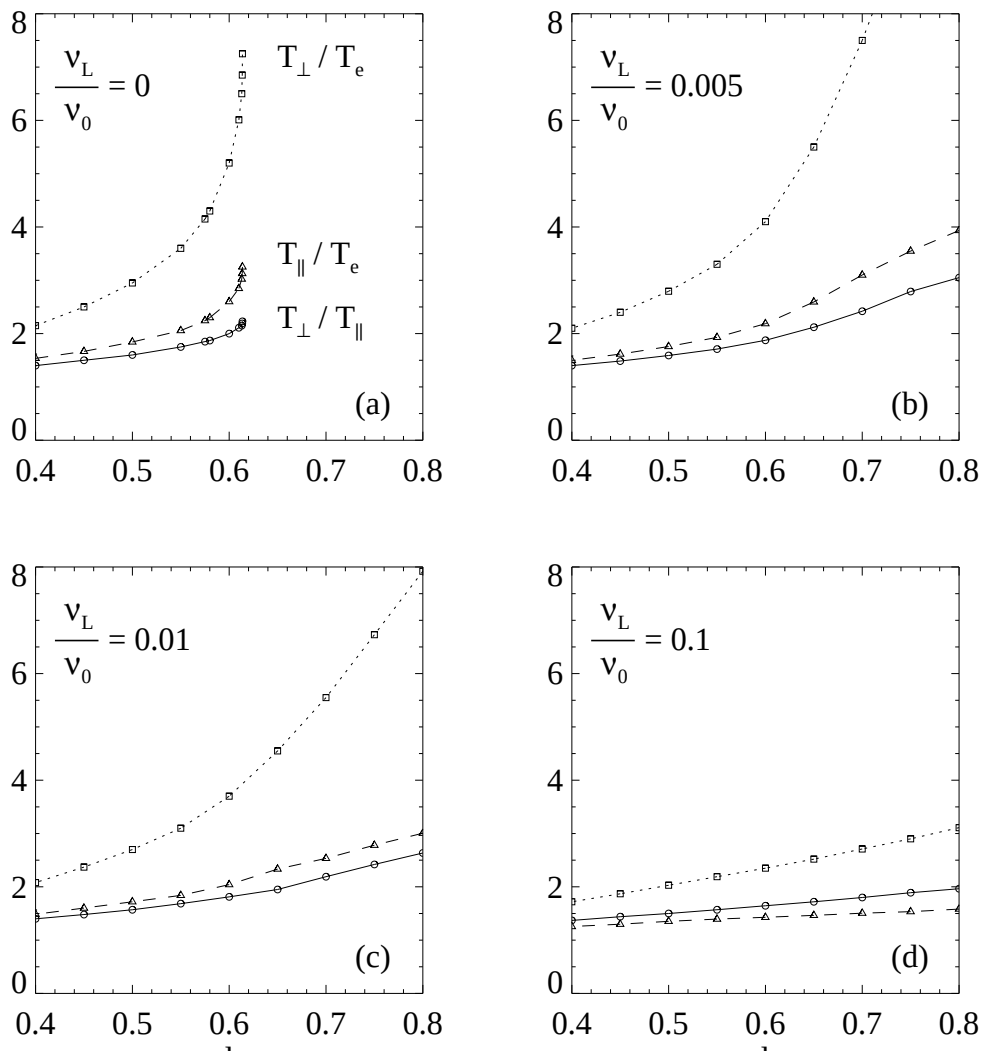

Figure 3.4: Temperatures with various ν_L/ν_0. When $\nu_L/\nu_0 = 0$, temperatures increase very rapidly at $d_e \simeq 0.61$ indicating run-away. $\delta = 5\,\%$ and $Z_{eff} = 1$.

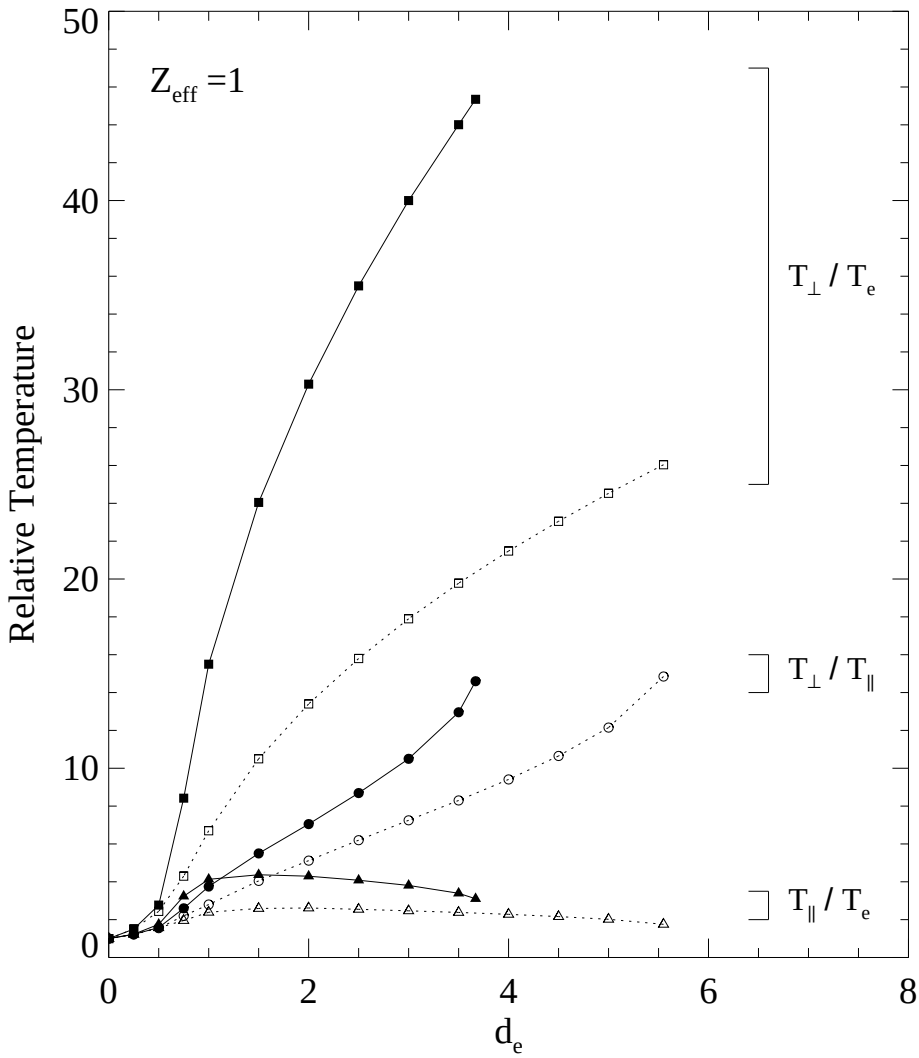

Figure 3.5: Temperature anisotropy with different ripple strength. Solid lines indicate the case with $\delta = 1\,\%$ and dotted lines with $\delta = 5\,\%$. With a larger ripple strength, more particles are trapped and are lost resulting in less temperature anisotropy at fixed d_e. $\nu_L/\nu_0 = 0.03$ and $Z_{eff} = 1$.

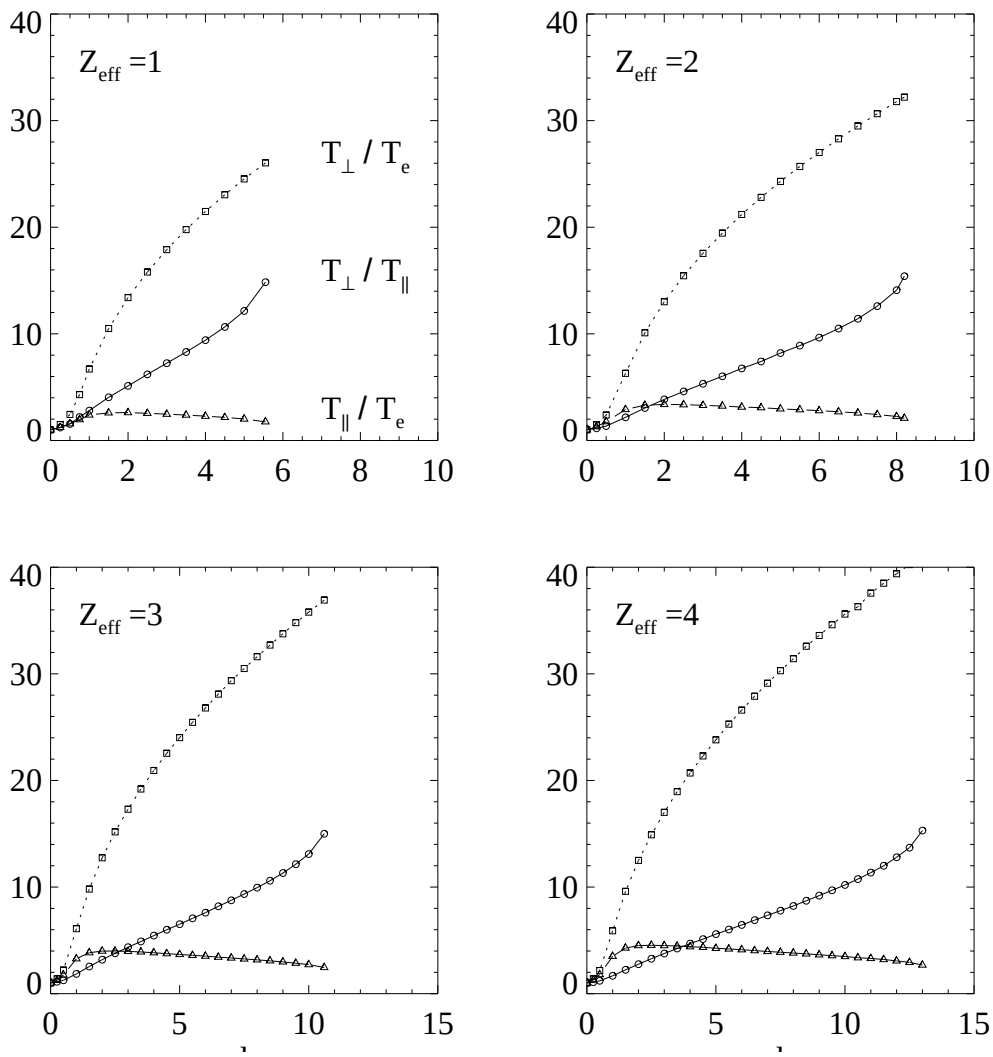

Figure 3.6: Temperature anisotropy with $Z_{eff} = 1, 2, 3, 4$. $\nu_L/\nu_0 = 0.03$ and $\delta = 5\,\%$.

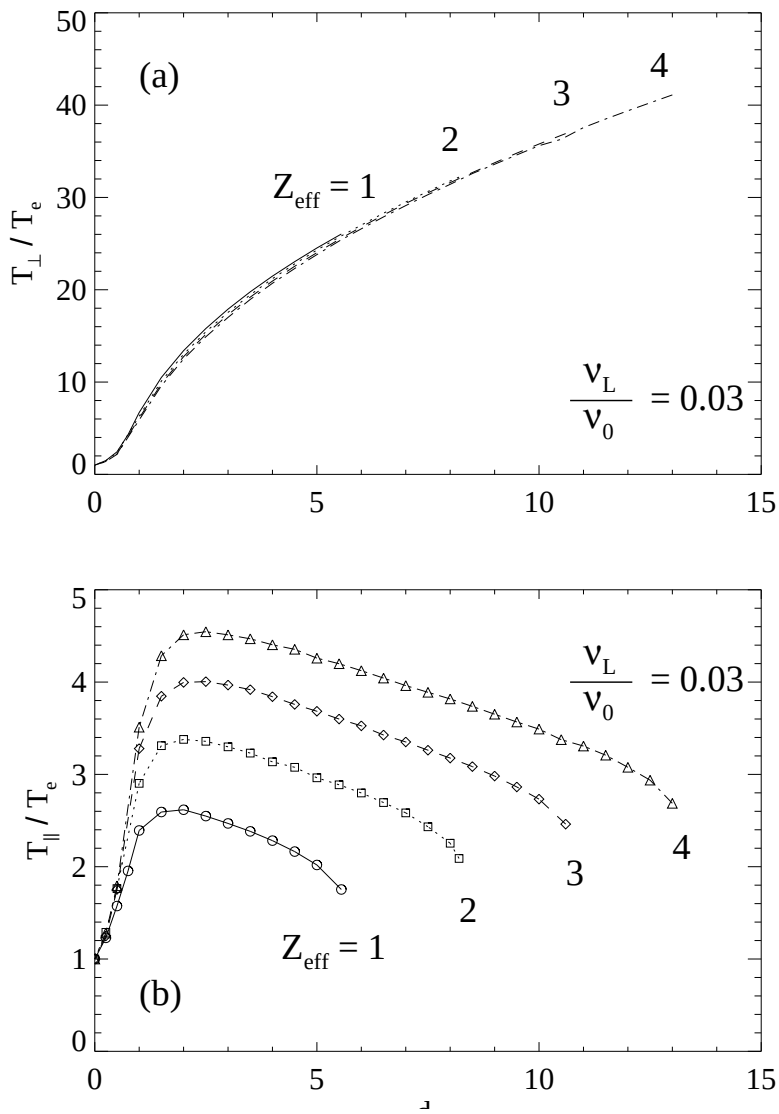

Figure 3.7: Z_{eff} dependence of perpendicular and parallel temperature. With a larger Z_{eff}, $T_\parallel$ is larger and $T_\perp$ is smaller due to more frequent pitch angle scattering. $\delta = 5\,\%$ and $\nu_L/\nu_0 = 0.03$.

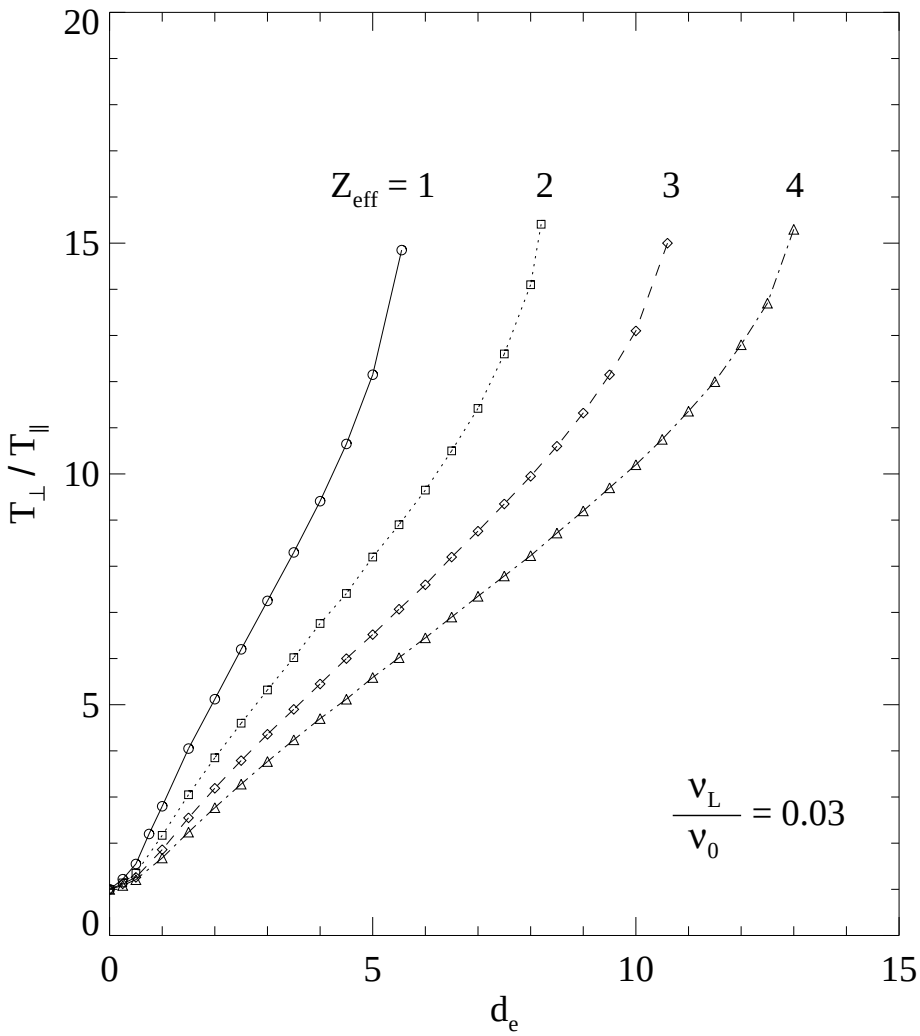

Figure 3.8: Warm electron temperature anisotropy with various values of Z_{eff}. $\delta = 5\,\%$ and $\nu_L/\nu_0 = 0.03$.

as large as 15, the electrostatic potential becomes significant when the density of warm species is more than 10 % of that of the cold background species [Choe *et al.*, 1995a]. If this is the case, it is important to include this potential in transport and stability theories which was usually neglected in the early neoclassical theories.

Chapter 4

Simulation of Energetic Electron Orbits and E_r Generation

IN THE PRESENCE OF LOCAL RIPPLE FIELDS, the magnetic field structure becomes rather complicated. It would therefore be instructive to perform a numerical simulation of the motion of a suprathermal electron having a predominantly perpendicular energy ($v_\perp/v_\parallel \gg 1$) in order to test the feasibility of the electron injection scenario. A Monte-Carlo electron guiding-center orbit code has been developed for this purpose.

4.1 Energetic Electron Orbit Calculation

The computer code numerically integrates four guiding-center equations of motion using the fourth-order Runge-Kutta method in the presence of ripple fields (generated by *TypeI* ripple coils) in a tokamak geometry. Equations of motion to be solved are:

$$\begin{aligned}
\frac{dR}{dt} &= (v_d)_R + v_\parallel \frac{B_R}{B}, \\
R\frac{d\phi}{dt} &= (v_d)_\phi + v_\parallel \frac{B_\phi}{B}, \\
\frac{dZ}{dt} &= (v_d)_Z + v_\parallel \frac{B_Z}{B}, \\
\frac{dv_\parallel}{dt} &= -\frac{\mu}{m_e}\frac{dB}{d\ell},
\end{aligned} \tag{4.1}$$

Input Plasma Parameter	**Value**
Average plasma density, $\overline{n}_e$	$2 \times 10^{18}\, m^{-3}$
Average plasma temperature, $\overline{T}_e$	$100\, eV$
Major radius, R_0	$0.35\, m$
Minor radius, a	$0.22\, m$
Elongation, κ	1.5
Toroidal Field at Axis, B_0	$0.1\, T$
q_0	0.8
q_a	4.0

Table 4.1: Input plasma parameters used in the simulation

where μ is the magnetic moment and (B_R, B_ϕ, B_Z) are components of magnetic fields. The drift velocity, v_d, is a combination of ∇B drift and curvature drift as given in Eq. (3.2), and $\mathbf{E} \times \mathbf{B}$ drift. The Coulomb drag and pitch-angle scattering of an energetic test electron off the background electrons, ions, and impurity ions are included in the calculation [1]. At each time step, the energetic electron's pitch angle is altered by means of random number generator. The simulation assumes concentric flux surfaces for simplicity.

Table 4.1 lists the CDX-U plasma parameters used in the simulation and the assumed radial profiles of plasma density, temperature, and safety factor are found in Fig. 4.1.

Figure 4.2 is a cross-sectional view of energetic electron orbits in the CDX-U plasma which illustrates the effects of collisions on electron orbits. Coulomb collisions, Fig. 4.2 (b), render banana orbits more scattered than in the collisionless case, Fig. 4.2 (a), due to the randomness of pitch-angle scattering while the electron loses its energy to background particles by energy drag.

Figures 4.3 and 4.4 are cross-sectional and top views of an energetic electron orbiting under the influence of ripple fields. For these figures, the ripple coil current is $I_{rip} = 8\, kA{\cdot}turn$, giving a ripple strength of $\delta = 2.82\,\%$ at the starting point ($R = 0.36\, m$, $\phi = 0\,^\circ$, $Z = 0.30\, m$) which is marked by an asterisk. It is assumed

[1] I would like to thank Dr. H. Towner for allowing us use his Fortran subroutine for Coulomb collisions.

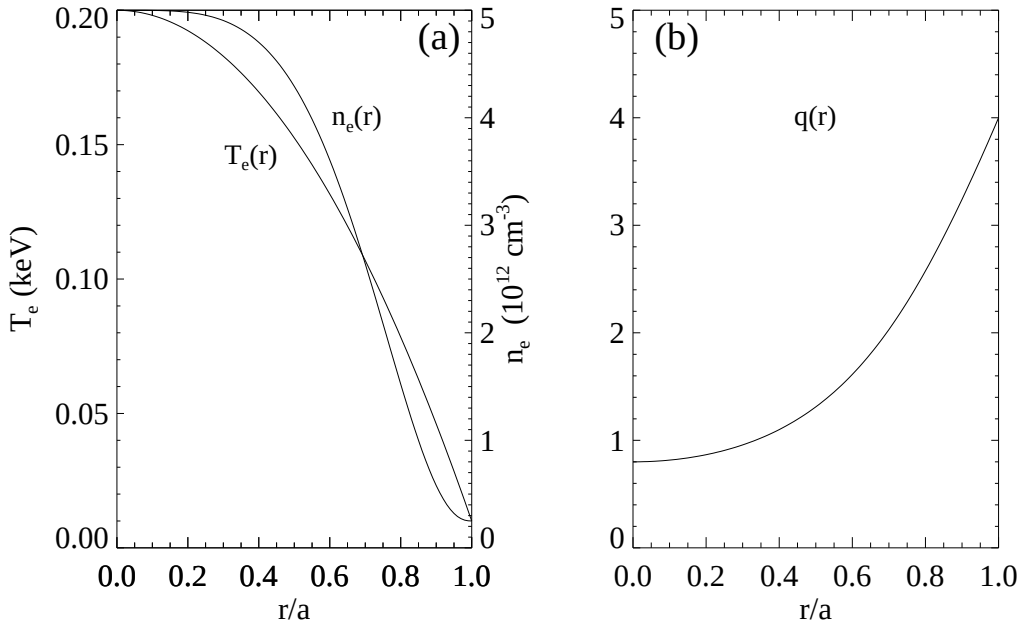

Figure 4.1: Density, temperature, and q profiles assumed in the orbit calculation.

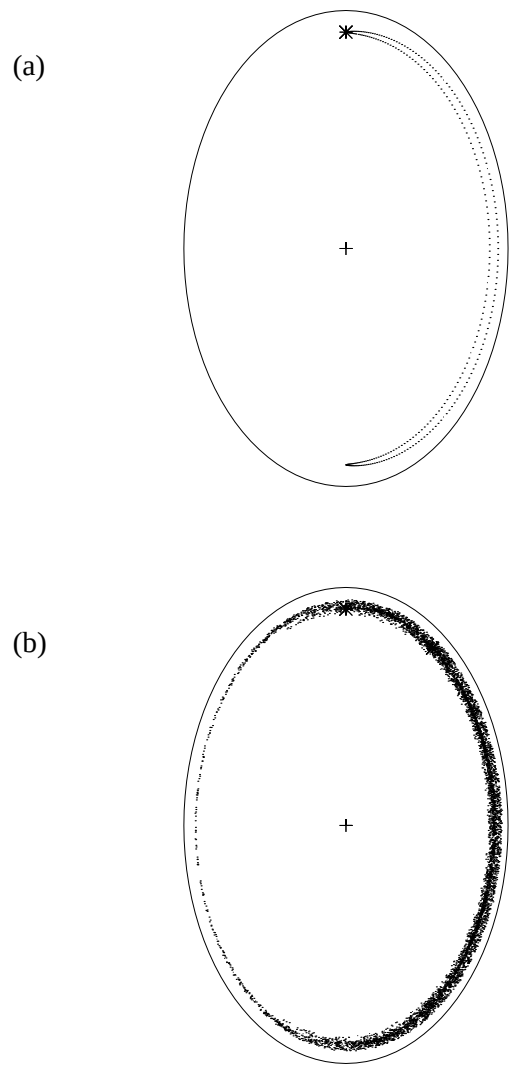

Figure 4.2: Effects of Coulomb scattering in the orbit calculation. (a) Collisionless case, and (b) pitch-angle scattering and energy scattering are included. The initial electron energy is $W_0 = 1.5\,keV$ and the ripple field is not included in both cases.

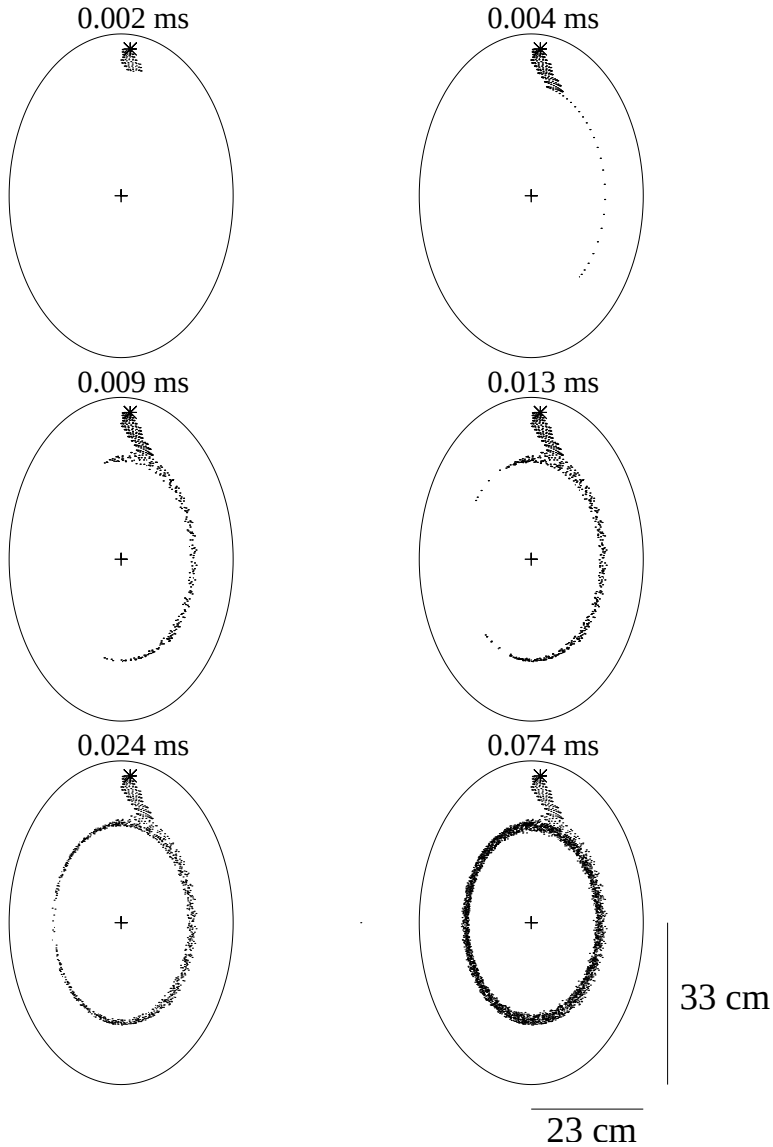

Figure 4.3: Cross-sectional view of the time trace of guiding-center trajectories of a $1.5\,keV$ electron started from the asterisk where $\delta = 2.82\,\%$ ($I_{rip} = 8\,kA\cdot turn$). In the final plot, the electron has slowed down to $0.5\,keV$ in $0.074\,msec$.

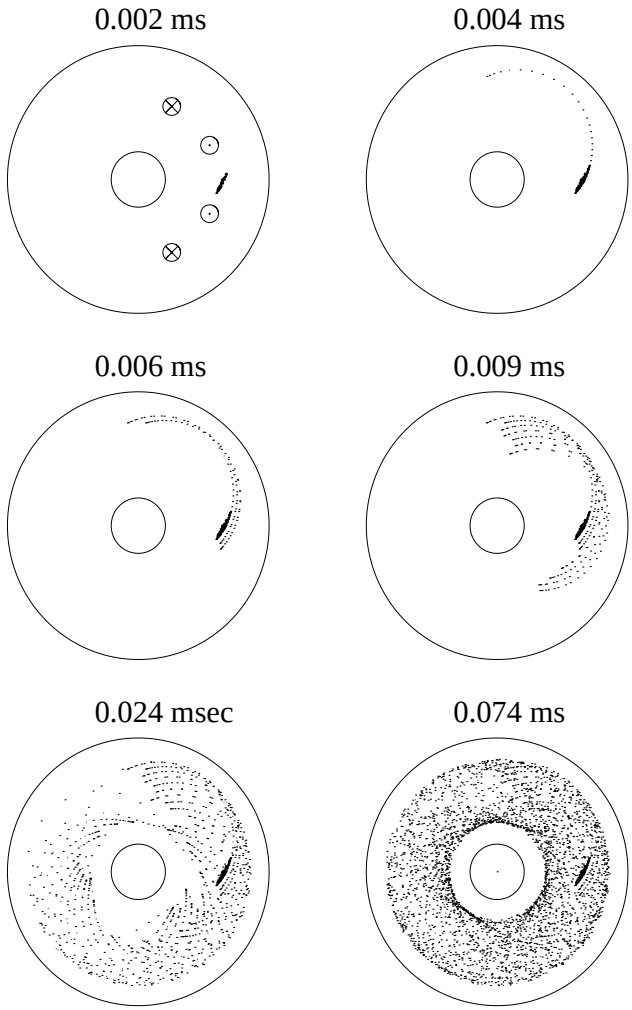

Figure 4.4: Time trace of test electron orbits in the presence of ripple fields. View from the top of the machine. The location of ripple coils are seen in the first plot with directions of current flowing ($W_0 = 1.5\,keV$, $I_{rip} = 8\,kA{\cdot}turn$).

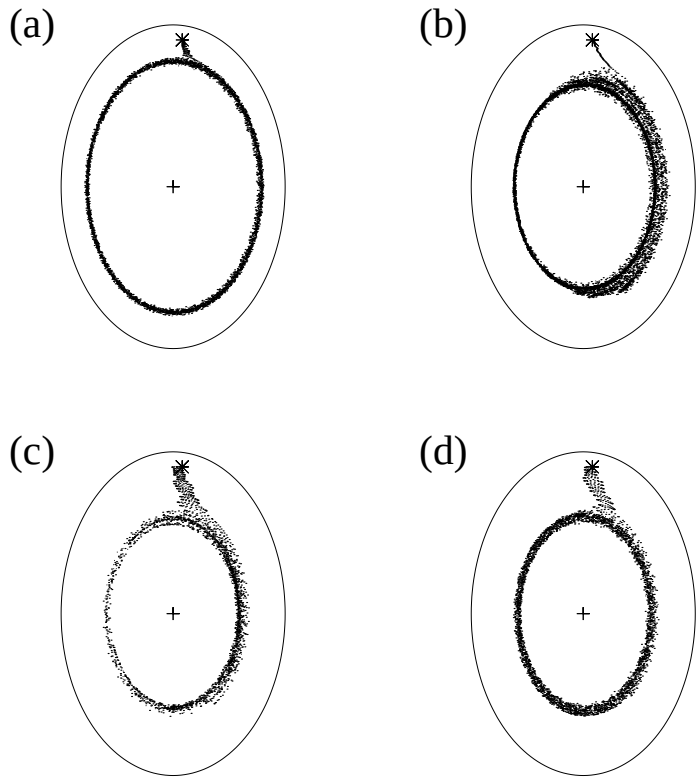

Figure 4.5: The radial penetration depth can be controlled by changing the ripple strength and the electron energy. (a) $I_{rip} = 4\,kA{\cdot}turn$ (1.45 % at the starting point) and $W_0 = 0.7\,keV$, (b) $I_{rip} = 4\,kA{\cdot}turn$ (1.45 %) and $W_0 = 2.0\,keV$, (c) $I_{rip} = 10\,kA{\cdot}turn$ (3.50 %) and $W_0 = 0.7\,keV$, (d) $I_{rip} = 8\,kA{\cdot}turn$ (2.82 %) and $W_0 = 1.0\,keV$. Either higher particle energy or larger ripple strength is necessary to get a sufficient penetration.

that the energetic electron initially has most of its kinetic energy in the direction perpendicular to the magnetic field. The toroidal field is pointed counterclockwise when viewed from top. The ∇B drift direction is downward for electrons. As shown in the figures, the energetic electron is locally trapped toroidally in the ripple well for about 4 μsec while experiencing downward drifts. Due to the decrease of the ripple strength and an increase of Coulomb collisions as it moves toward plasma center (increasing $n_e(r)$), the ripple-trapped electron now becomes detrapped and moves in the toroidal direction. The electron follows a banana orbit and, at the same time, it loses its energy to background particles by Coulomb drag. The elapsed time from the initial energy of $1.5\,keV$ to the final energy of $0.5\,keV$ is $74\,\mu sec$. As shown in Fig. 4.3, the electron penetrates $0.13\,m$ into the plasma.

The radial penetration depth of an energetic electron can be controlled by two independent variables, ripple strength and the initial electron energy. Four different cases are compared in Fig. 4.5 where (a) $I_{rip} = 4\,kA{\cdot}turn$ (1.45 % at the starting point) and $W_0 = 0.7\,keV$, (b) $I_{rip} = 4\,kA{\cdot}turn$ (1.45 %) and $W_0 = 2.0\,keV$, (c) $I_{rip} = 10\,kA{\cdot}turn$ (3.50 %) and $W_0 = 0.7\,keV$, (d) $I_{rip} = 8\,kA{\cdot}turn$ (2.82 %) and $W_0 = 1.0\,keV$. As can be seen from the figure, in order to produce a similar penetration depth to that in (d), either higher particle energy (from (a) and (b)) or larger ripple strength (from (a) and (c)) is necessary to get a sufficient penetration.

4.2 Radial Electric Field Generation

Since these penetrated electrons accumulate at the flux surfaces where they are detrapped from the ripple region and thermalized, the net effect is to charge the plasma negatively resulting in a build-up of electrostatic potentials, i.e., radial electric fields (E_r) from the edge toward the plasma center with a scale length of the penetration distance. In order to simulate this phenomenon, a few assumptions are made. First, the plasma is divided into a number of radial zones separated by concentric flux surfaces. The background particle density and temperature are assumed to be constant on a flux surface due to large parallel heat conduction [Braginskii, 1966] ($\kappa_\parallel/\kappa_\perp \sim (\omega\tau)^2 \gg 1$). Second, in order to speed up the numerical procedure, we assume that a single electron deposits multiple charges (for example, $Q = -10^{12}\,e$) at the flux surface where detrapping occurs. Third, it is also assumed that a series

of electrons are launched sequentially at the same starting point under the same condition. (The algorithm for the calculation of radial electric fields is found in Fig. 4.6). In this way, the nth launched electron sees the electric fields generated by 1st to $(n-1)^{th}$ electrons, and it experiences $\mathbf{E} \times \mathbf{B}$ drifts in both poloidal and toroidal directions.

Since the injected warm electrons move toward the plasma center and accumulate at flux surfaces farther inward than the initial flux surface where energetic electrons start their drifts, the background electron current has to counter-balance the injected electron current in steady-state. The outward radial current carried by the background cold electrons induced by an inward electric field can be written in the form

$$E_r - E_{r0} = \frac{1}{\sigma_\perp}\, j_r, \tag{4.2}$$

where E_{r0} is the equilibrium electric field without j_r and $\sigma_\perp$ is the electrical conductivity orthogonal to the flux surfaces, which may be a function of E_r. In order to find out E_r from a given j_r, we use the force balance relation between the $j_r \times B_\phi$ force and the plasma viscous force in the poloidal direction.

$$j_r\, B_\phi = (\nabla \cdot \Pi)_\theta, \tag{4.3}$$

where Π is the viscosity tensor and j_r is the radially outward electrical current carried by the background plasma. Reference [Chang, 1993] has been used for a simple analytic expression of the viscosity tensor Π. As the electric field increases, the $\mathbf{E} \times \mathbf{B}$ rotation speed v_E increases. At low v_E values, $(\nabla \cdot \Pi)_\theta$ increases with v_E. Hence, for a given j_r, an equilibrium value of v_E is determined. As v_E is increased further, $(\nabla \cdot \Pi)_\theta$ reaches a maximum and then decreases [Chang, 1993]. In this case, there can be two solutions for v_E, leading to a bifurcation. In a steady-state, the outward plasma current j_r will have to balance the injected current. Equation (4.3) is another way of writing Eq. (4.2).

Figure 4.7 shows a time trace of radial profiles of electric fields generated by 100 electrons and the corresponding final rotation speed v_E assuming poloidal rotation is dominant. The dotted curve in Fig. 4.7 (a) indicates the radial electric field strength above which a bifurcation occurs. The shape of E_r which looks similar

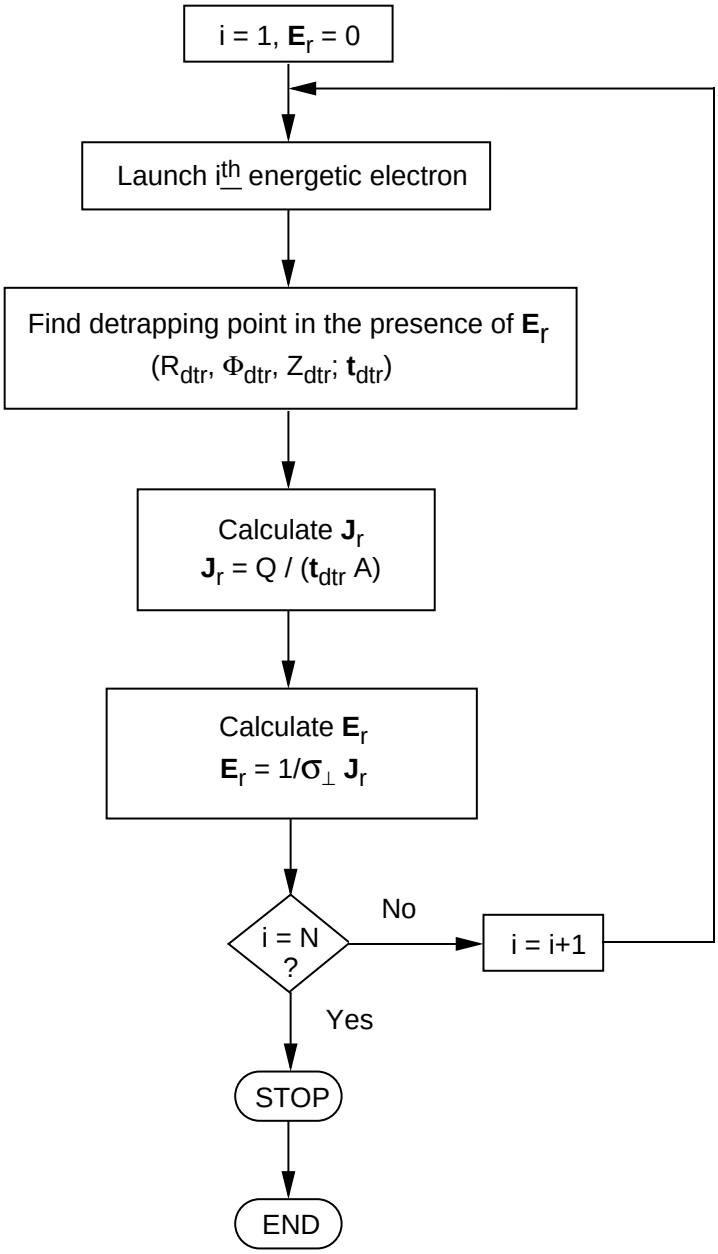

Figure 4.6: Algorithm for calculating radial electric fields generated by ripple-injected electrons.

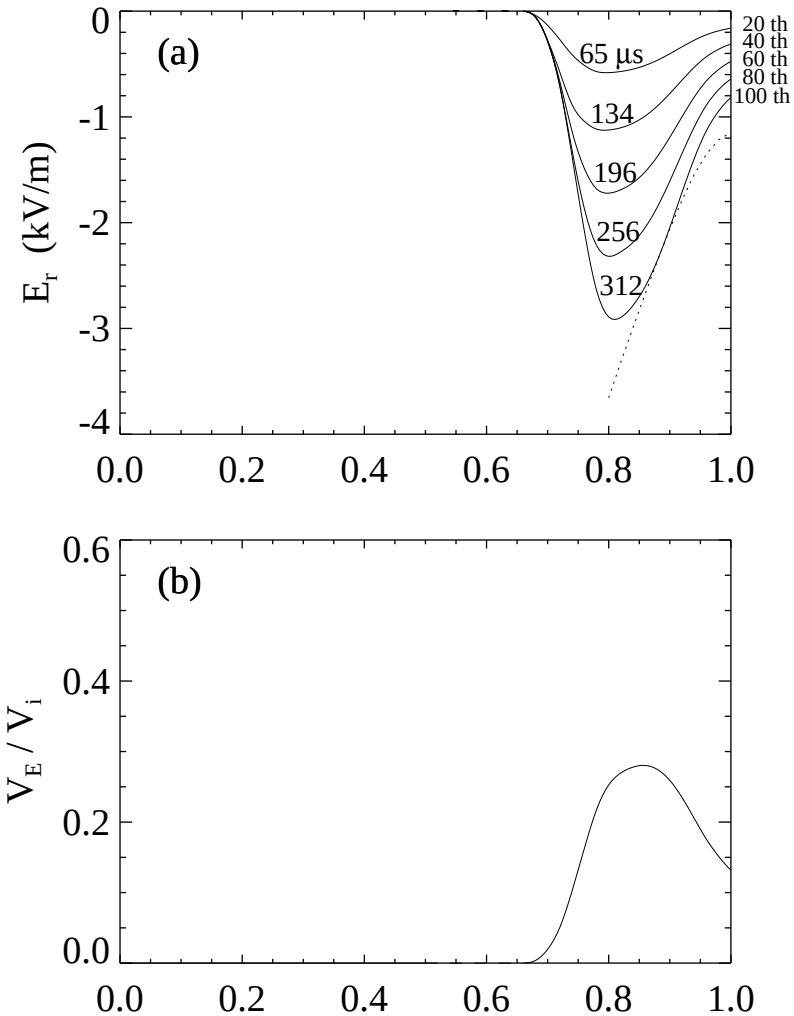

Figure 4.7: (a) Time trace of radial profiles of electric fields. Dotted curve indicates the required electric field above which a bifurcation occurs. (b) $\mathbf{E}\times\mathbf{B}$ rotation speed normalized by ion thermal speed generated by sequential deposition of 100 energetic electrons. The deposited charge per electron is assumed to be $Q = -4.6 \times 10^{12}\, e$ and $W_0 = 1.0\, keV$ and $I_{rip} = 8\, kA\cdot turn$.

to that observed in other devices with different methods [Ida *et al.*, 1991; Kim *et al.*, 1994c] is not only determined by the electron deposition profile but also by the information of background particles via $\sigma_\perp$ of Eq. (4.2). The time elapsed to induce $-3.0\,kV/m$ is less than $0.4\,msec$. Since the deposited charge per electron was assumed to be $Q = -4.6\times10^{12}e$ and 100 electrons were launched for the calculation, the total number of energetic electrons involved is 4.6×10^{14}. This indicates that the injection of a population of electrons equal to 1.2 % of the total population between $r/a = 0.9$ and $r/a = 1.0$ is necessary to generate $-3.0\,kV/m$ of electric fields. For this particular run (Fig. 4.7), the total injected radial current is $23\,A$ and this is realized approximately by the electrical charge of $4.6\times10^{14}e$ and the average detrapping time of $3\,\mu sec$. This amount of radial current suggests that only $23\,kW$ of electron cyclotron heating power may be required for a bifurcation to occur.

A large Q-value produces large electric fields but once E_r reaches a certain amount, launched electrons become less penetrating due to larger $\mathbf{E}\times\mathbf{B}$ drifts. Shown in Fig. 4.8 (a) are the radial electric field profiles generated by 10, 20, 30, 40, 50, 60, 80, and 100 electrons. The incremental increase in E_r becomes smaller with each injected electron, suggesting the saturation of E_r at some limit. In (b), the radial position at which detrapping occurs is plotted.

The role of radial electric fields on orbits of successive electrons is illustrated in Figures 4.9 and 4.10. Compared to the case without radial electric fields (Fig. 4.9 (a)), the cases with nonzero E_r makes electrons less penetrative as seen in Fig. 4.9 (b). Figure 4.10 is an illustration to show the effect of E_r on the electron penetration where the orbits of four different ($1^{st}, 22^{nd}, 48^{th}$ and 100th) electrons among 100 launched electrons are plotted. It shows the shift of orbits in the direction of the $\mathbf{E}\times\mathbf{B}$ drift whose poloidal component is in the clockwise direction in the figure.

In Fig. 4.11, the electric field profile is shown with several different ripple strengths. As is seen in the figure, the electric field can be maximized at $r/a \simeq 0.86$ with a modest amount of ripple strength ($I_{rip} = 4\,kA\cdot turn$). On the other hand, with larger ripple fields, E_r propagates further radially inward (due to deeper penetration) while the peak value is decreased (due to the larger detrapping time and thus, smaller radial current density injected).

As discussed previously, there is another parameter that can be used to control the electron penetration depth and, thus, E_r. Figure 4.12 shows that a

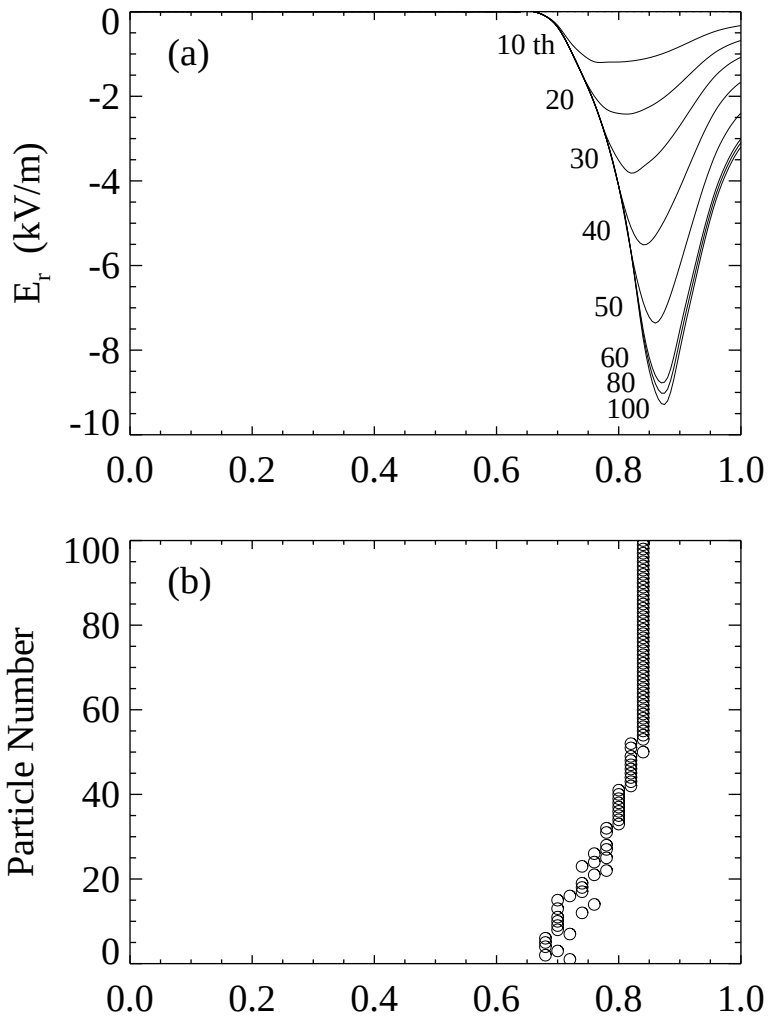

Figure 4.8: (a) Electric field profiles generated by 10, 20, 30, 40, 50 60, 80, and 100 electrons, and (b) the radial locations of 100 launched electrons where detrapping occurs. $Q = -1.8 \times 10^{13}\, e$ and $W_0 = 1.0\, keV$ and $I_{rip} = 8\, kA \cdot turn$.

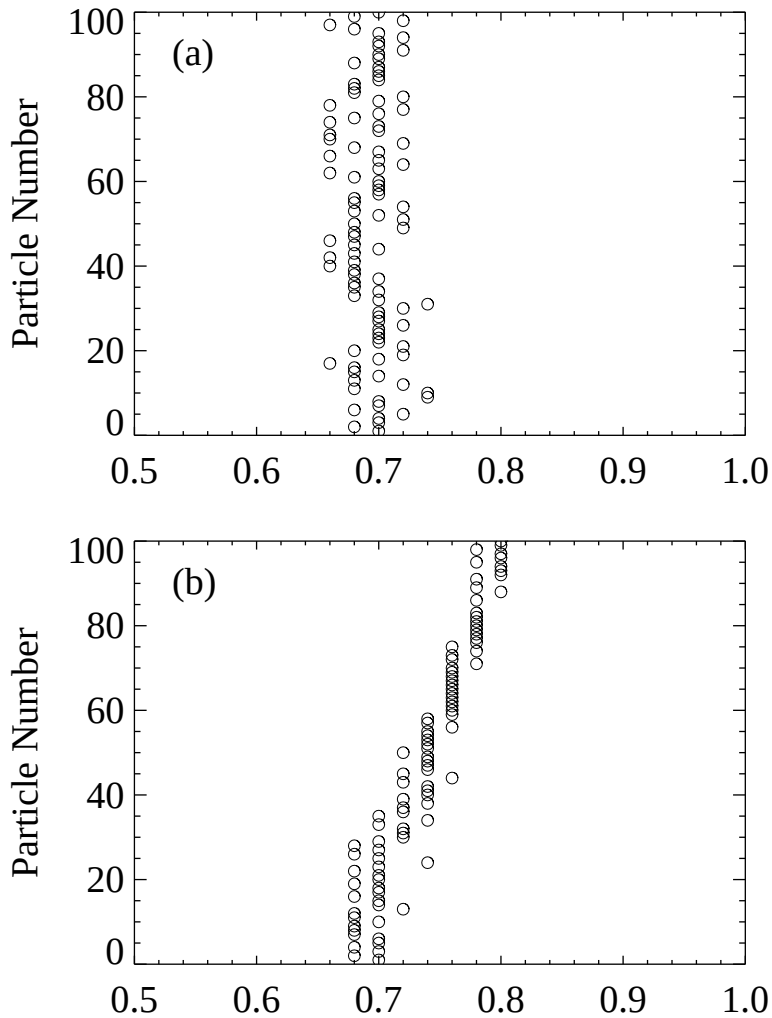

Figure 4.9: Plot of detrapping points of 100 sequentially launched electrons. Initial electron energy is $W_0 = 1.0\,keV$ and $I_{rip} = 8\,kA{\cdot}turn$ (2.82 %). (a) Radial electric fields are not considered in the calculation of electron orbits ($Q = 0$), (b) radial electric fields are included ($Q = -6.0 \times 10^{12}\,e$). In this case, electrons cannot penetrate as much as the case without electric fields since $\mathbf{E} \times \mathbf{B}$ drifts hinder the radial penetration.

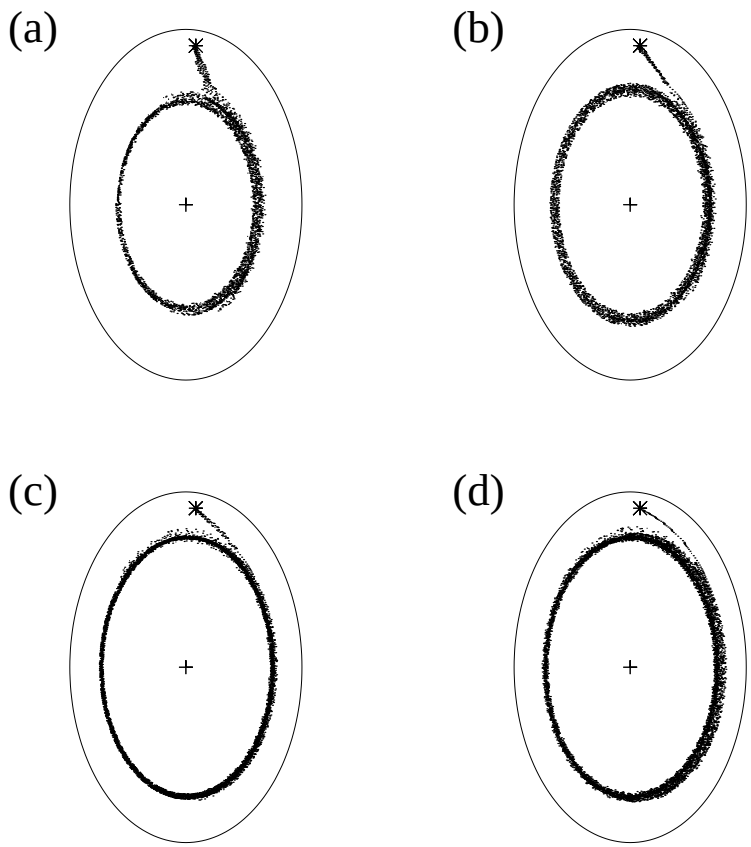

Figure 4.10: Orbits of the (a) 1st, (b) 22nd, (c) 48th, and (d) 100th electron among 100 launched electrons. $I_{rip} = 8\,kA{\cdot}turn$, $Q = -1.2 \times 10^{13}\,e$, $W_0 = 1.0\,keV$. Electrons become less penetrative as E_r builds up.

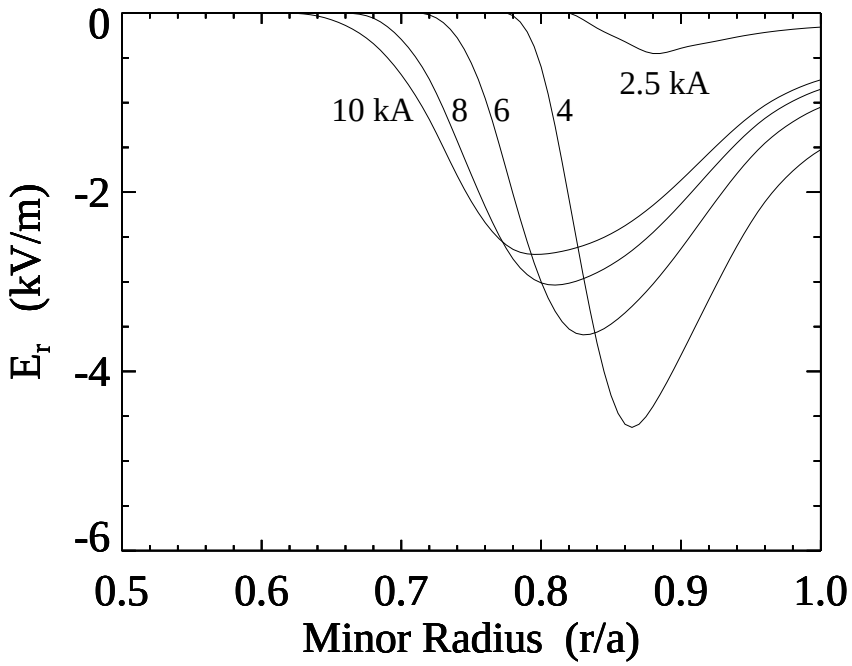

Figure 4.11: The electric field profiles with several different ripple strengths. The strength of ripple at the starting position corresponds to 0.92 % ($2.5\,kA\cdot turn$), 1.45 % ($4\,kA\cdot turn$), 2.15 % ($6\,kA\cdot turn$), 2.82 % ($8\,kA\cdot turn$), and 3.50 % ($10\,kA\cdot turn$), respectively. Energetic electrons are launched with initial energy $W_0 = 1.0\,keV$ and $Q = -4.6 \times 10^{12}\,e$.

fairly large amount of E_r can be obtained by changing the initial energy of energetic electrons with a given ripple strength and Q.

For larger size future devices such as ITER, obtaining H-mode is very important [Perkins *et al.*, 1995; Kaye *et al.*, 1995] especially for an adequate ignition margin and the possibility of using ELMs to facilitate ash removal [Hillis *et al.*, 1993; Hillis *et al.*, 1994]. In this context, it may be meaningful to extend this electron ripple injection concept to an active control of plasma confinement via externally generated radial electric fields. In order to estimate the required ECRH power in ITER, a similar simulation has been performed with ITER parameters ($\overline{n}_e = 2 \times 10^{19}\ m^{-3}$, $\overline{T}_e = 3.7\,keV$, $a = 3.0\,m$, $\kappa = 1.54$, $R_0 = 8.1\,m$, $B_0 = 5.7\,T$, $q(a) = 2.85$, $Z_{eff} = 1.34$). It is assumed that the ripple coils are located at $R = R_0$ and $Z = 1\,m$ above the edge of the plasma with the coil current of $0.8\,MA$. Since the critical electron energy above which our assumptions are valid is given by $62\,keV$ (Eq. (3.6)), the energetic electrons are launched with the energy of $80\,keV$ at $R = R_0$, $Z = 0.2\,m$ below the edge of the plasma where the ripple strength is $0.73\,\%$. Figure 4.13 is obtained from 100 electrons assuming $Q = -2.0 \times 10^{15} e$ and it shows the electric field profile and the corresponding poloidal rotation speed profile. In order to produce approximately $-260\,kV/m$ of electric fields, the total injected radial current is calculated to be $120\,A$ and the time needed is $11.9\,msec$. This would mean approximately $10\,MW$ of ECRH power is required to induce an E_r-bifurcation, which is relatively modest for ITER. For this case, a total of 2.0×10^{17} electrons are needed and this is a negligible portion of ITER edge electrons.

4.3 Summary

The behavior of energetic electrons in the presence of externally-provided ripple fields and the generation of radial electric field are investigated by a Monte-Carlo guiding-center electron orbit code. A series of simulations predicts that the generation of a fairly large radial electric field via ERI technique is possible not only on CDX-U but also on a reactor size device, ITER, with a reasonable power of about $23\,kW$ and $10\,MW$, respectively. Simulations also suggest the good controllability of E_r-generation, i.e., the magnitude and radial profile of E_r can be controlled by

ripple strength (through ripple coil current) and electron energy (through ECRH power). This prediction is an encouraging result suggesting that the ERI technique could be a promising alternative for generating a strong radial electric field and, thus, for possibly controlling tokamak plasma transport.

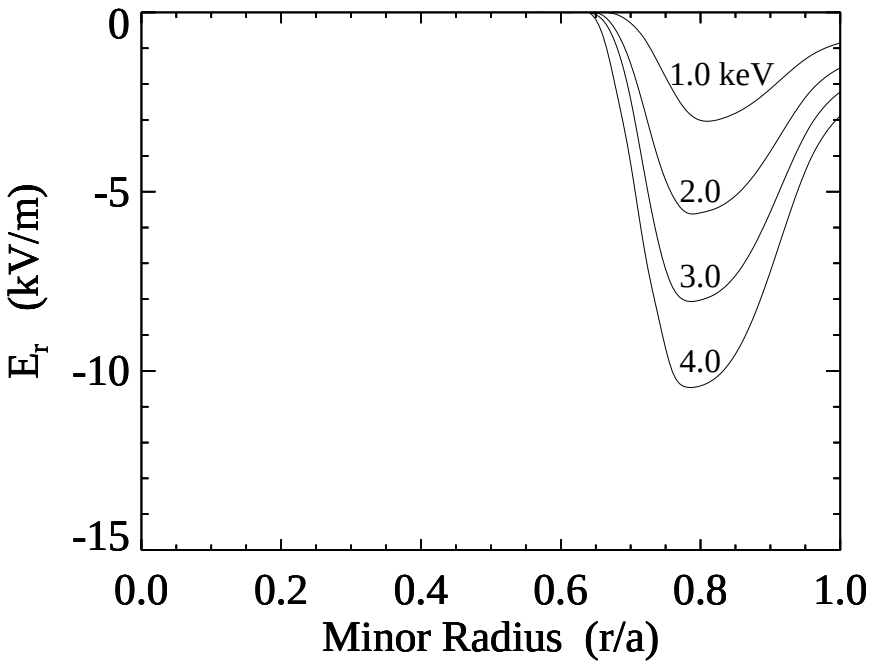

Figure 4.12: The electric field profiles with several different initial energy. $Q = -4.6 \times 10^{12}\, e$ and $I_{rip} = 8\, kA \cdot turn$.

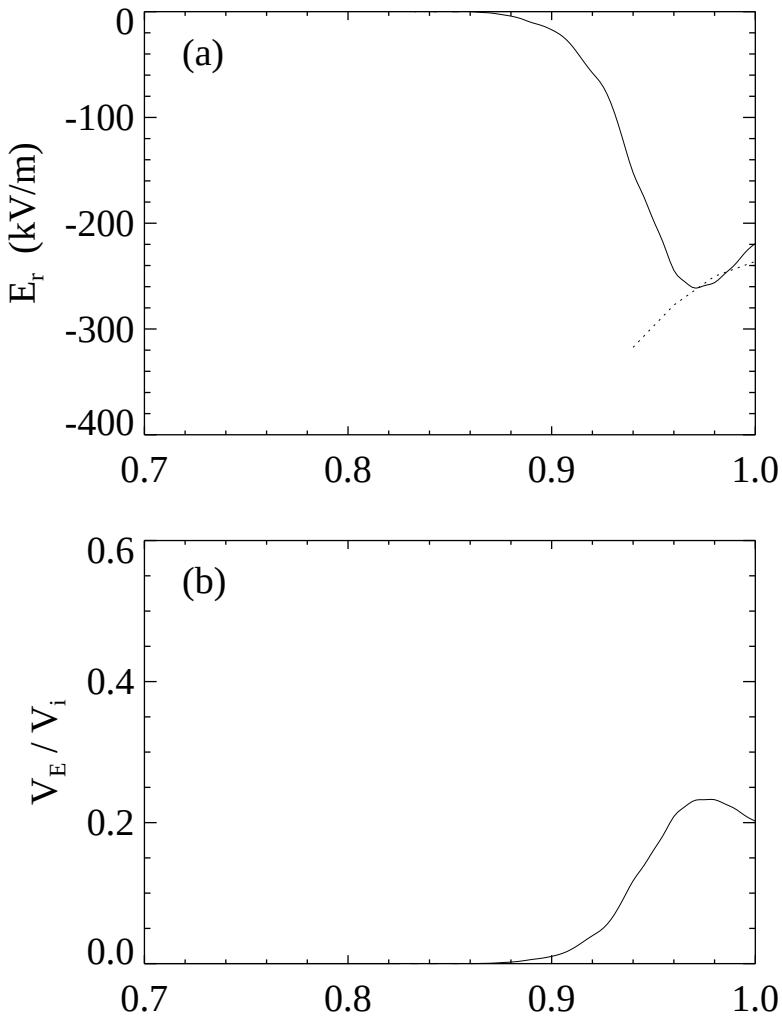

Figure 4.13: Similar run with ITER parameters. (a) Electric field profile, and (b) $\mathbf{E} \times \mathbf{B}$ rotation speed normalized by ion thermal speed. $Q = -2.0 \times 10^{15}\, e$, $W_0 = 80\, keV$, and $I_{rip} = 0.8\, MA \cdot turn$.

Chapter 5

CDX-U Device

AS DISCUSSED in previous chapters, modeling supports the electron ripple injection idea very well, so that an experimental investigation of this subject is worthwhile. Before discussing preliminary ERI experiments done on CDX-U in detail, a brief description of the CDX-U device is given in this chapter.

The CDX-U device was designed and constructed in order to accommodate the capability of exploring various advanced concepts for tokamaks. These concepts include dc-helicity injection which has been developed and studied [Ono *et al.*, 1987; Darrow, 1988; Darrow *et al.*, 1990; Ono *et al.*, 1993] as a source for the non-inductive current drive for possible long pulse and/or steady-state tokamak operation. The investigation of internally generated neoclassical currents due to trapped particles and pressure gradients that occur naturally in the plasma has also been performed [Forest, 1992; Forest *et al.*, 1992]. Since the bootstrap currents can significantly reduce the requirements for non-inductive current drive, they are considered essential for the realization of economical tokamak reactors. The unique feature of the CDX-U tokamak is that it offers a vehicle for the exploration of the tokamak physics at aspect ratios as low as 1.4 [Hwang *et al.*, 1995], which is quite low compared to the value of ~ 3 in typical tokamaks. Since the detailed description of the CDX-U device and diagnostics are found in a few references [Forest, 1992; Hwang, 1993; Jones, 1995], only a brief description of the device and the hardware that is relevant to the electron ripple injection experiment will be given in this chapter.

Geometric Parameter	Definition	Value
R_0	$(R_{outer} + R_{inner})/2$	$35\,cm$
A	$(R_{outer} + R_{inner})/(R_{outer} - R_{inner})$	1.33
κ	$H/(R_{outer} - R_{inner})$	1.72

Table 5.1: Geometric parameters of CDX-U vacuum vessel.

5.1 The CDX-U Device

The CDX-U device was constructed in 1989 and produced its first plasma in January, 1990 after three years of preparation. Since there was no ohmic transformer in the device, experiments focused mainly on non-inductive current drive. During this phase of operations, several new results such as fully bootstrap current driven tokamak configuration [Forest, 1992; Forest *et al.*, 1992] and evidence of anomalous current transport [Hwang, 1993] were observed. In October of 1993, a significant upgrade was performed by adding an ohmic heating system to the CDX-U device, motivated by the desire to explore low-aspect ratio tokamak physics at higher plasma current and temperatures, and generally more reactor-relevant plasma parameters.

A cross-section of CDX-U with the vacuum vessel assembly and locations of toroidal field (TF) and poloidal field (PF) coils is shown in Fig. 5.1. The top and side views of the assembled CDX-U device are also depicted in Fig. 5.2. As shown in the figures, the vacuum vessel is composed of a center stack, an outer cylindrical wall, and top and bottom flanges. The radius from the major axis of the device to the Inconel center stack outer surface is $8.73\,cm\,(R_{inner})$ and the major radius of the inside aluminum wall is $61\,cm\,(R_{outer})$. The maximum vertical height between the insides of the top and bottom stainless steel flanges is $90\,cm\,(H)$. Even though the maximum plasma volume will be smaller due to the presence of limiters, these vessel dimensions can give a rough indication of the possible plasma size. Table 5.1 summarizes the geometric parameters of the CDX-U device.

The toroidal field (TF) coil system consists of a bundle (128) of central conductors housed in the Inconel center stack and 16 detachable 'C'-shaped return coil sections. These return sections are located outside the vacuum vessel and

Coil	**R** (cm)	**Z** (cm)	**No. of turns**
Green	8.9	49.0	50
Green	8.9	-49.0	50
Orange	40.6	84.0	18 (57 max.)
Black	40.6	-84.0	18
Yellow	67.3	40.0	15
Yellow	67.3	-40.0	15
Blue	83.8	36.0	25
Blue	83.8	-36.0	25

Table 5.2: Poloidal field coil data (dimensions are to the center of each coil).

are electrically and mechanically connected to the center stack. The toroidal field strength in terms of the single turn coil current is

$$B_T\,(kG) = 25.6\,\frac{I_{TF}\,(kA)}{R\,(cm)},$$

and $B_T = 0.86\,kG$ at $R = 35\,cm$ with $I_{TF} = 1.18\,kA$.

As shown in Fig. 5.1, there are four pairs of poloidal field (PF) coils with various different number of winding. Each pair of coils is positioned at the same distance above and below the midplane and color-coded for convenience. The position and number of turns of coils are listed in Table 5.2. Each poloidal field coil pair can be energized independently and some coils are pulsed with an SCR switch and capacitor bank to provide time dependent poloidal magnetic fields.

An ohmic heating (OH) system was added to the existing CDX-U in 1993 with some modifications of the device. Flux changes in the solenoid not only drive plasma current inductively but also heat the plasma through ohmic dissipation. The strongest magnetic field inside the center stack at the maximum design ohmic power is $4.3\,T$ and is produced in the ohmic solenoid. The OH system was designed to generate up to $100\,kA$ of plasma current in the CDX-U device. The $150\,mV \cdot sec$ flux swing capability of the OH supply could deliver up to $200\,kW$ of current drive and heating power for the period of $20\,msec$.

Two types of ripple coils ($Type I$ and $Type II$) were designed and constructed using the computer code developed for studying the magnetic field topology, as

described in Chapter 2. However, the ripple coil *TypeII* was mainly used for the preliminary CDX-U electron ripple injection experiments to produce more prominent effects of ripple fields on the electron behavior. 8 AWG wires were wound around two TF outer sections by 28 turns in a rectangular shape in such a way that the ripple center (center of a pair of winding) coincides with the electron cyclotron heating wave inlet as shown in Fig. 2.7 and Fig. 5.3. The total resistance and the inductance of the pair of coils are $0.48\,\Omega$ and $2.20\,mH$.

5.2 $2.45\,GHz$ Microwave System

As discussed, electron cyclotron resonance heating is introduced in the electron ripple injector in order to enhance electron trapping and drift. The electron cyclotron frequency is expressed as

$$f_{ce} = \frac{eB}{2\pi m_e} = 2.8 \times 10^3\, B(kG).$$

This is in the range of $1 - 10\,GHz$ for the CDX-U toroidal magnetic field. For our purposes, a $2.45\,GHz$ magnetron was used as a wave source with the corresponding magnetic field of $0.86\,kG$ in order for electrons to resonate to this wave. The electron cyclotron heating (ECH) system is arranged as shown in Fig. 5.4. The microwave source is Richardson Electronics YJ1190, $6\,kW$ magnetron and it is installed in a cabinet, as shown in the figure, that include high voltage modulators and air cooling. The microwaves from the source were coupled and transmitted through unterminated WG-283 waveguide and a $0.16\,cm$ ceramic seal sandwiched between two waveguide flanges acting as a vacuum window, and then introduced into the vacuum vessel. The wave is launched from the top of the device where $R = 35\,cm, Z = 45\,cm$ with X-mode polarization ($\mathbf{E}_{wave} \perp \mathbf{B}$). The transmitted and reflected wave power were measured by 50 dB directional coupler and Hewlett Packard 8473B Schottky diode power detectors. Ref. [Forest *et al.*, 1990; Forest, 1992] describes the magnetron and other relevant parts in more detail.

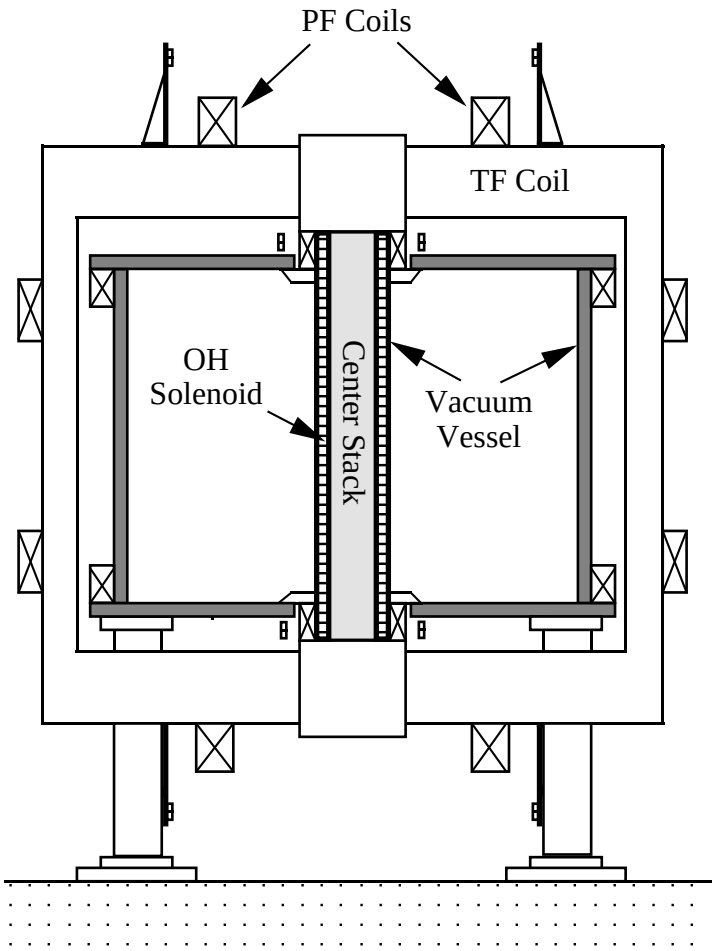

Figure 5.1: CDX-U device showing the vacuum vessel assembly and locations of the toroidal field (TF) and poloidal field (PF) coils.

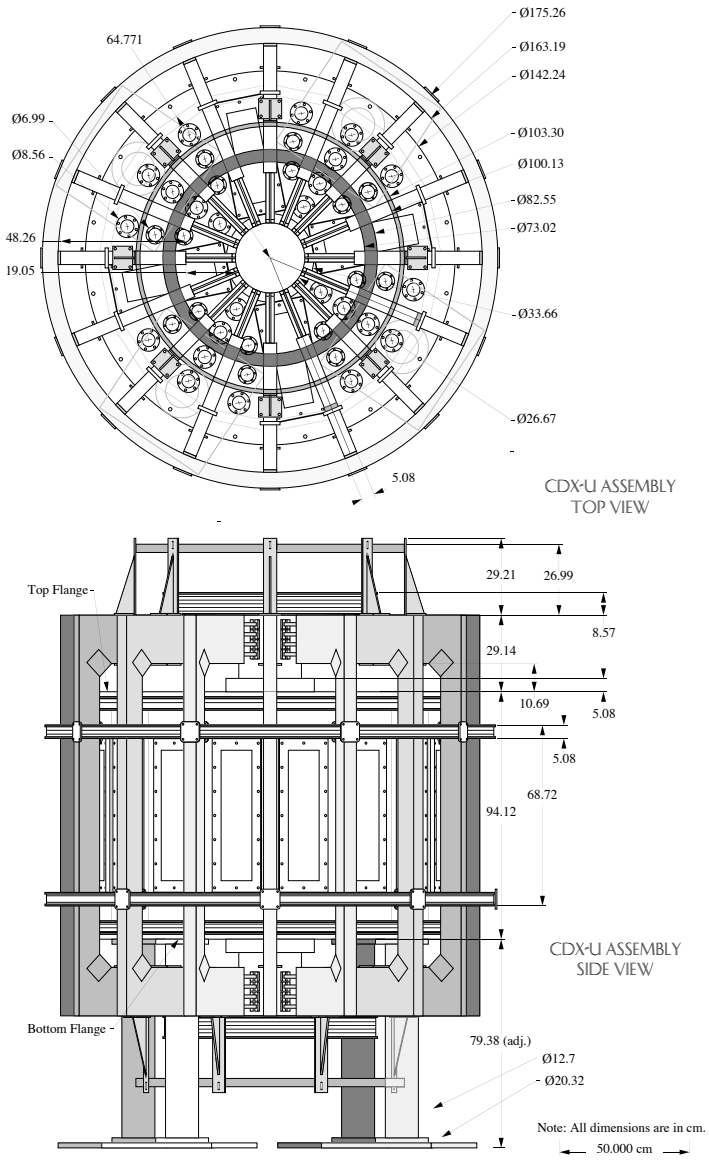

Figure 5.2: Top and side view of the assembled CDX-U device.

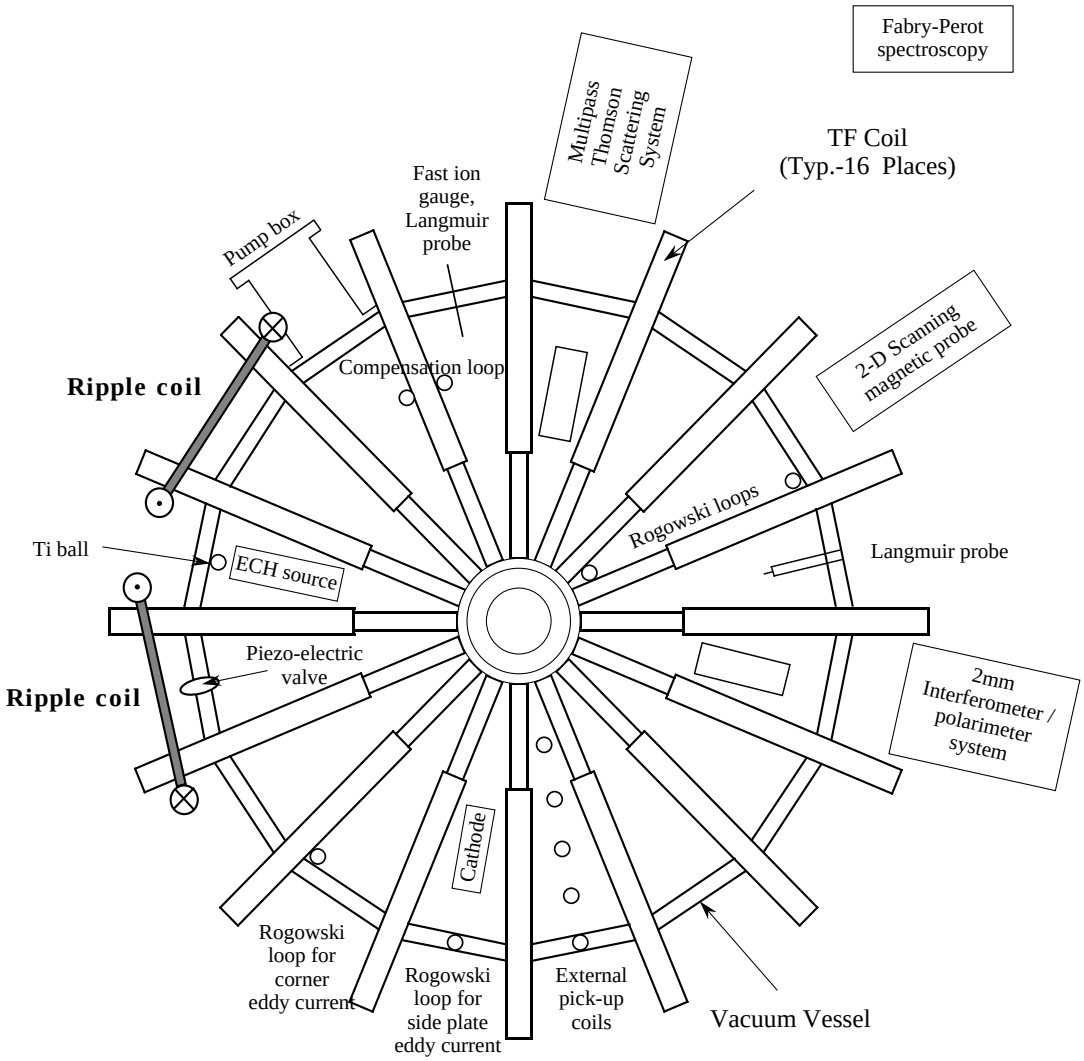

Figure 5.3: Location of CDX-U ripple coil $TypeII$ viewed from the top of the device.

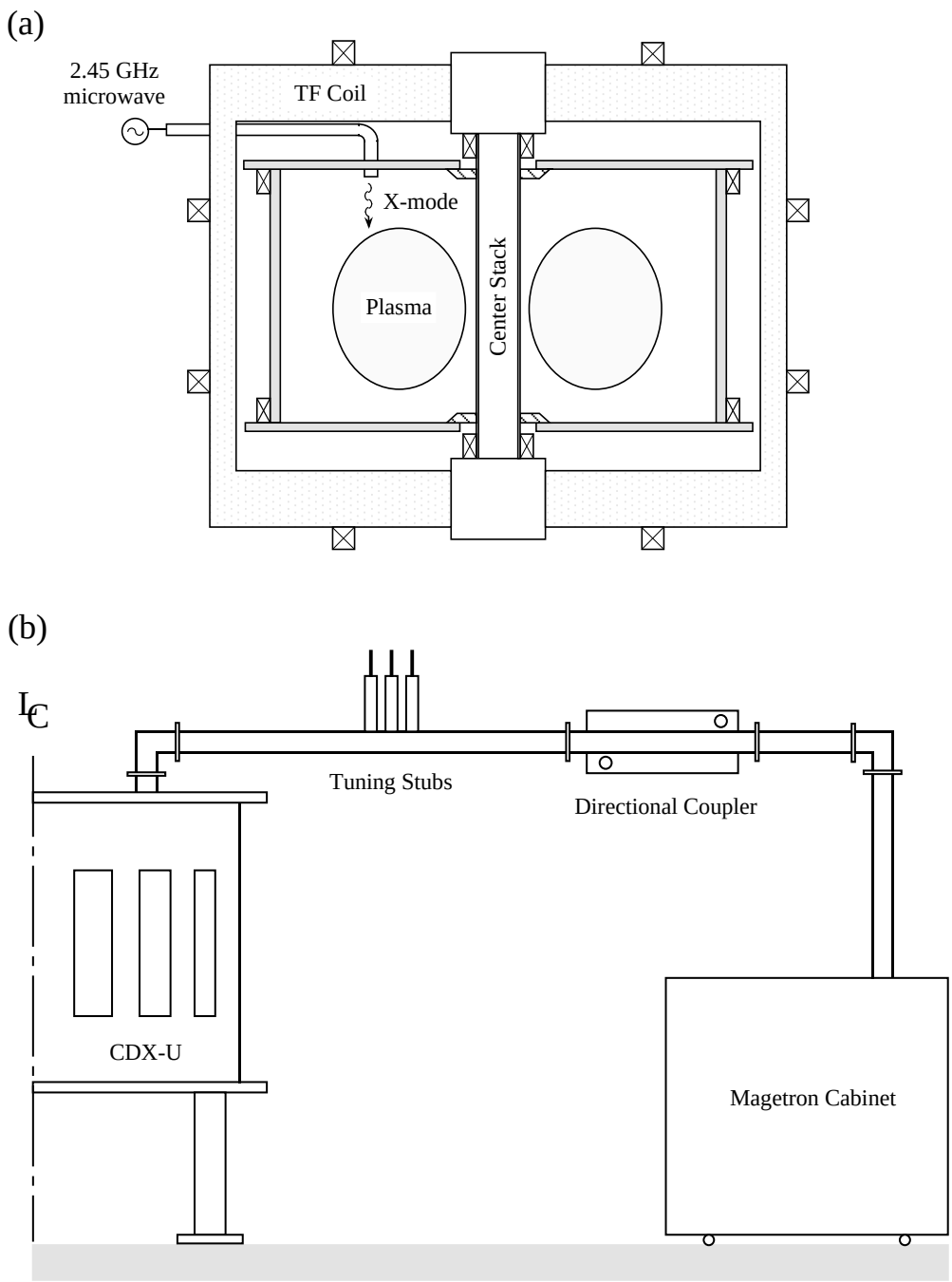

Figure 5.4: A schematic of ECH system. (a) shows where microwave power is introduced in to the vessel. (b) depicts waveguide run, directional coupler, tuning stubs, and the magnetron cabinet. The antenna is simply an unterminated WG-283 waveguide.

5.3 Diagnostics for Routine Plasma Parameters

The CDX-U plasmas were routinely diagnosed by various methods measuring line-integrated electron density, plasma temperature, plasma current and local magnetic fields, magnetic fluctuation, and plasma position etc (Table 5.3).

In 1994-95 as a collaboration work with Johns Hopkins University and Hebrew University in Israel, spectroscopic diagnostics were added to monitor the electron temperature and possible MHD activities occurring in the CDX-U plasmas. At typical densities in CDX-U ohmic discharges, the C IV (2p-1s) and O VI (3d-2p) lines would be excited and appear at temperatures above $60\,eV$ and $100\,eV$, respectively. The observation of these radiation lines would indicate that a significant number of electrons over those temperatures exist in the plasma, and thus, the minimum central electron temperature can be inferred by observing the lines. In order to accomplish this monitoring, two different metal foil filters were used: a Ag 2000 $\AA$ foil in series with a Sn 2500 $\AA$ foil with a bandpass of $30-80\,\AA$ for C IV, and a pair of Zr 4000 $\AA$ foil filters with a bandpass of $100-150\,\AA$ for O VI lines.

To date, a multipass Thomson scattering system is under preparation and when it is in the working order, it can provide more accurate and more spatially resolved informations.

5.4 Timing and Data Acquisition

Timing of all events during a plasma shot including data acquisition was controlled by a set of Berkeley Nucleonics Corp. 7010 digital time delay modules.

The CDX-U data acquisition system consists of several CAMAC modules and crates, and a MacIntosh Quadra 800 computer for crate control and data storage. The CAMAC crates and the MacIntosh are interconnected by 8901 GPIB crate controller. All data from the plasma were digitized by LeCroy 8210 (10-bit, 4 channel, 100 kHz) or LeCroy 8212A/8 (12-bit, 8 channel, 25 kHz) digitizer modules and recorded in LeCroy 8800/12 memory module in the CAMAC system, and downloaded to the MacIntosh computer. The CAMAC system was controlled by National Instruments LabVIEW 3.1 software running on the MacIntosh Quadra computer. Data saved in the MacIntosh were ultimately transferred to the SPARC

Plasma parameter	**Symbol**	**Diagnostics**
Electron density	$\bar{n}_e$ n_e	Microwave ($2\,mm$) interferometer Langmuir probe
Electron temperature	T_e	Spectroscopy, Thomson scattering Langmuir probe
Ion temperature	T_i	Fabry-Perot interferometer
Plasma current	I_p	Rogowski coil
Poloidal **B**	Ψ B_R, B_Z	Flux loops Magnetic pick-up loops 2-D scanning magnetic probe
Magnetic fluctuation/ MHD activity	$\dot{B}_p$ $\dot{T}_e$	2-D scanning magnetic probe Soft x-ray diagnostics
Plasma position		Segmented limiter array
Vacuum vessel eddy current		Rogowski coil

Table 5.3: Available CDX-U diagnostics.

workstation through ETHERNET and analyzed using Interactive Data Language (IDL) developed by Research Systems, Inc.

Chapter 6

ERI Experiment on CDX-U

IN ORDER TO understand the underlying physics of the electron ripple injection concept, a few different sets of experiments have been performed on CDX-U step by step: (1) confirmation of the existence of electrons drifts (Section 6.1); (2) investigation of magnetic field line topology in the presence of magnetic ripple fields (Section 6.2); (3) observation of combined effects of electron ripple trapping and electron cyclotron resonance heating (Section 6.3.1); and finally (4) measurement of electron temperature anisotropy (Sections 6.3.2 and 6.3.3). This chapter describes each topic in turn, and compares experimental results with the theoretical predictions.

6.1 Particle Drifts

Since the particle drifts (∇B and curvature drifts) play such a crucial role transporting energetic electrons to generate radial electric fields in the electron ripple injection concept, it would be very important to experimentally confirm the existence of these drifts. In order to attempt this, a $20\,cm$ side cubic cavity box of $0.3\,mm$ thick copper sheets was put inside the CDX-U vacuum chamber (Fig. 6.1). Inside the box, 14 copper strips of $1.1cm$ width were positioned horizontally in such a way that they were perpendicular to the toroidal magnetic field so that they could collect charged particles generated by the microwave breakdown. The strips were electrically isolated from one another and connected to ground through resistors. $2.45\,GHz$ microwave power was introduced of the top side of the box through an

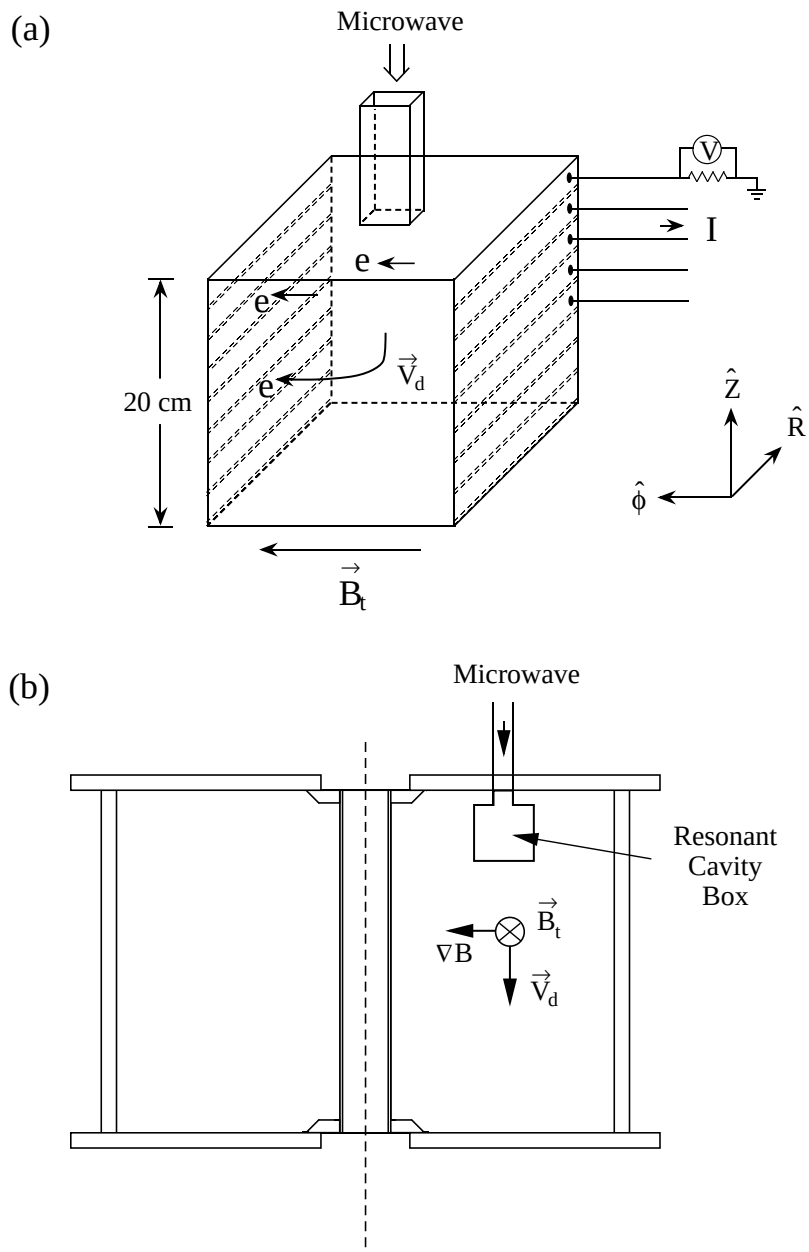

Figure 6.1: (a) 20 *cm* side cubic resonant cavity to observe vertical drifts. 14 copper strips are aligned horizontally and perpendicularly to the toroidal field. (b) Location of the cavity box inside the vacuum chamber. The direction of drifts for electrons is downward.

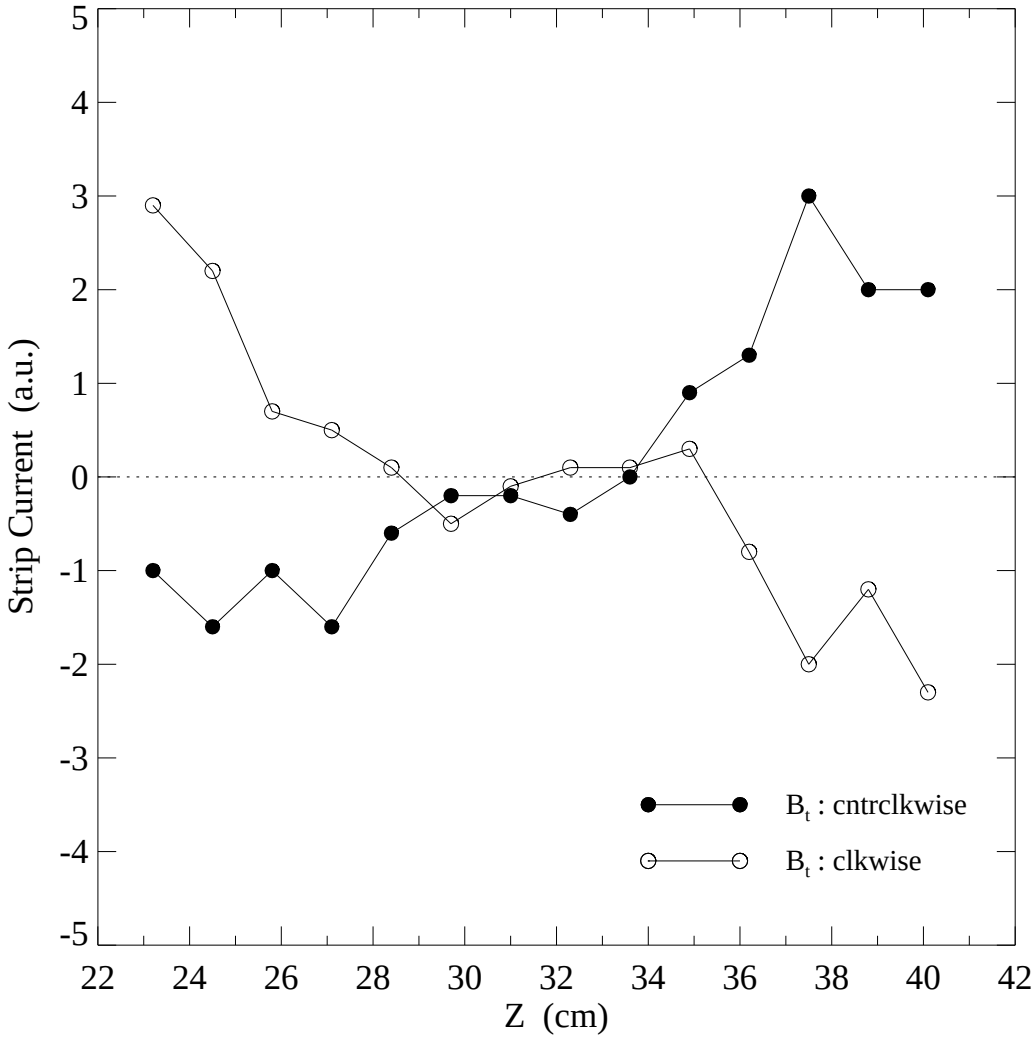

Figure 6.2: Vertical distribution of strip currents showing the existence of vertical drifts. When the toroidal magnetic field is counterclockwise looking down from the above (closed circles), the direction of electron drift is downward and vice versa for ions. With the reversed toroidal fields (open circles), the behavior is opposite.

unterminated WG-283 waveguide, and a three-stub tuner was used to maximize the absorption of wave power. In this configuration, the box was acting as a resonant cavity. The cavity Q measured via $Q \simeq f_0/\Delta f$ where $f_0 = 2.45\,GHz$ was approximately 1500. For an efficient coupling of wave power to electrons, an electron cyclotron resonance layer was positioned at the center of the cavity by providing an appropriate toroidal magnetic field strength ($860\,G$). About $0.55\,kW$ of microwave power caused the breakdown of a hydrogen gas with a gas pressure of 8.5×10^{-5} torr, and the current from each copper strip was measured. For this experiment, only toroidal field was applied and no other fields including ripple fields were introduced.

Figure 6.2 shows the vertical distribution of strip currents and it is due to the vertical drifts of charged particles depending upon the direction of toroidal fields. Closed (open) circles indicate strip currents with toroidal fields in counterclockwise (clockwise) sense looking down the setup. When the toroidal field is in the counterclockwise sense, vertical drifts generate a charge separation in such a way that electrons move downward and ions move upward. It is shown in Fig. 6.2 that strip currents are negative (electron dominant) downside and positive (ion dominant) upside as expected. With reversed toroidal field, the behavior is opposite.

6.2 Topology of a Magnetic Field Line

In order to verify how ripple fields change the topology of toroidal field lines, a couple of simple experimental setups were devised. See Chapter 2 for the description of *TypeI* and *II* ripple coils.

Toroidal field + ripple field by *TypeI* coils

In this setup, a tungsten filament was installed at the center of the ripple region to generate an electron ring using 5×10^{-5} torr of a hydrogen gas. A current sensor, composed of 20 copper strips to ground through $5\,\Omega$ resistors was aligned horizontally to measure the vertical shift of the electron ring, and a Langmuir probe was installed to observe a radial excursion of the electron ring. Since charged particles follow field lines, these diagnostics were to give the information of electron trajectories, and thus, field lines. The current sensor and the Langmuir probe were located 180° toroidally away from the electron source. Figures 6.3 and 6.4 show

the results with *TypeI* ripple coils. Open circles denote the case when only the toroidal field is applied and closed circles indicate that the ripple field is added to the toroidal field. As can be seen in Fig. 6.3, the addition of ripple fields ($\delta \simeq 3.5\,\%$) bend a field line in such a way that it bulges out in the ripple region compared to the case with toroidal field only. In this field line configuration, electrons emitted from the source that is located at the center of the ripple region follow the field line and move (major) radially inward as they get out of the ripple region and reach the probe tip which is placed on the other side of the torus, where ripple effect is negligible. Measurement indicates a radial excursion of about $1.2\,cm$, consistent with the calculation at this ripple strength (Fig. 2.8). Figure 6.4 shows the strip currents and the downward shift of the peak observed when ripple fields are present. This is attributed to the downward bend of field lines by ripple fields and downward drifts of electrons.

Another observation in Fig. 6.3 is that the probe current increases when ripple fields are applied. This can be understood by the fact that the tungsten filament is located at $Z = 36.5\,cm$ and the probe is placed at $Z = 34.5\,cm$ so that the center of the electron ring is brought down toward the probe tip due to the vertical field line bending and electron drifts.

Figure 6.5 summarizes the experiment. The projection of an electron trajectory in the absence of ripple fields, i.e., with toroidal fields only is shown in the broken line, and it is depicted as a circle in the plan view and a flat line in the side view. When ripple fields are added, however, field lines bend not only radially but also vertically as is depicted in solid lines. This field line bending causes the shift of peaks in figures 6.3 and 6.4, correspondingly.

Toroidal field + ripple field by *TypeII* coils

Similar results were obtained with *TypeII* ripple coils (Fig. 6.6). Instead of using a tungsten filament, electron cyclotron resonance wave power was provided this time for breakdown of a hydrogen gas as shown in Fig. 2.7. The radial location of the peak of probe current in the absence of ripple fields coincides with the location of electron cyclotron resonance layer. An addition of ripple fields ($\delta = 1.6\,\%$ at the resonance layer) make the probe peak shift major radially inward by $0.3\,cm$.

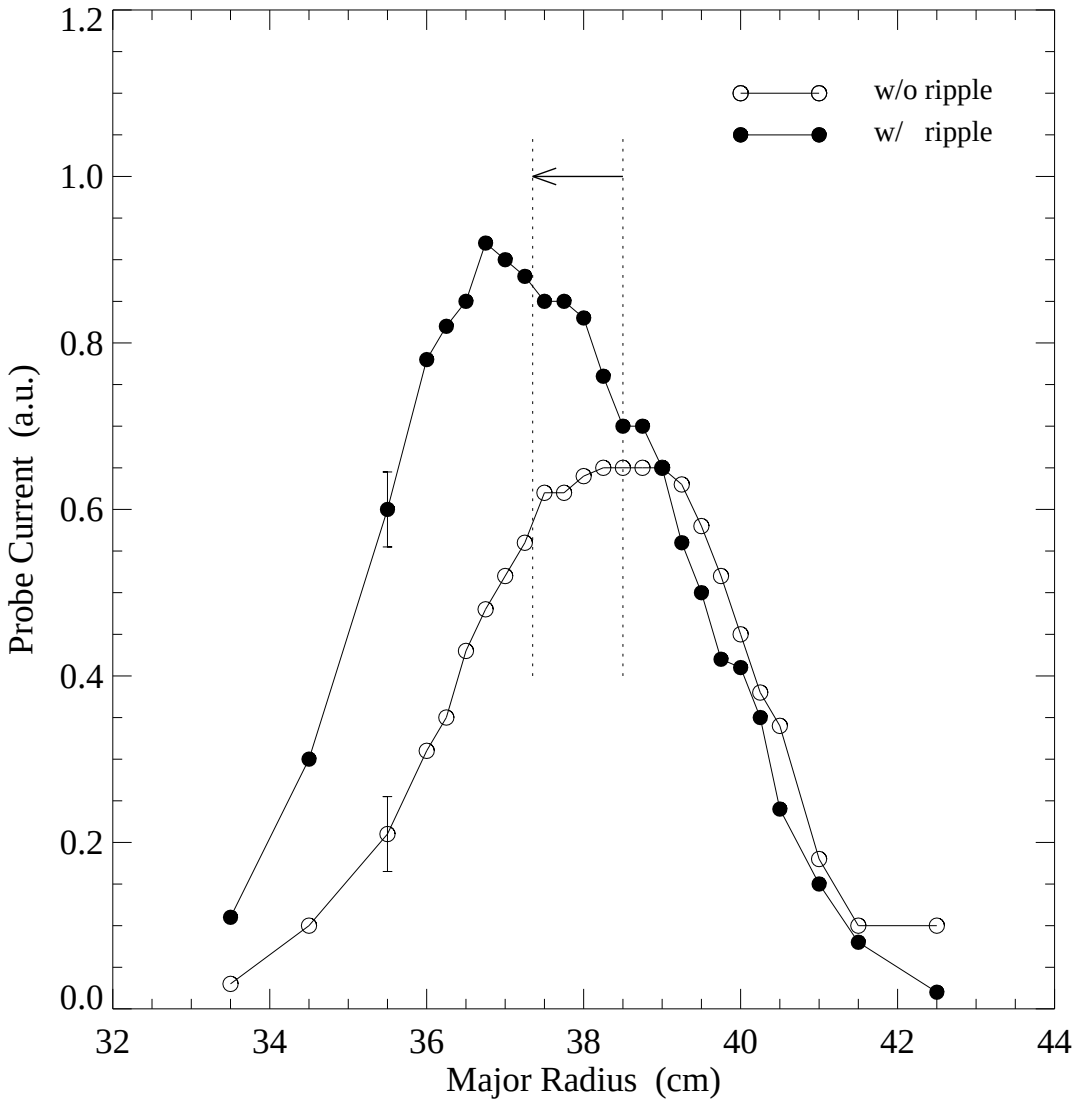

Figure 6.3: Radial profile of electron ring emitted from a tungsten filament measured by a Langmuir probe. The vertical location of tungsten electron source is at $Z = 36.5\,cm$ and probe is at $Z = 34.5\,cm$. With $\delta = 3.5\,\%$ from the ripple coil $Type I$.

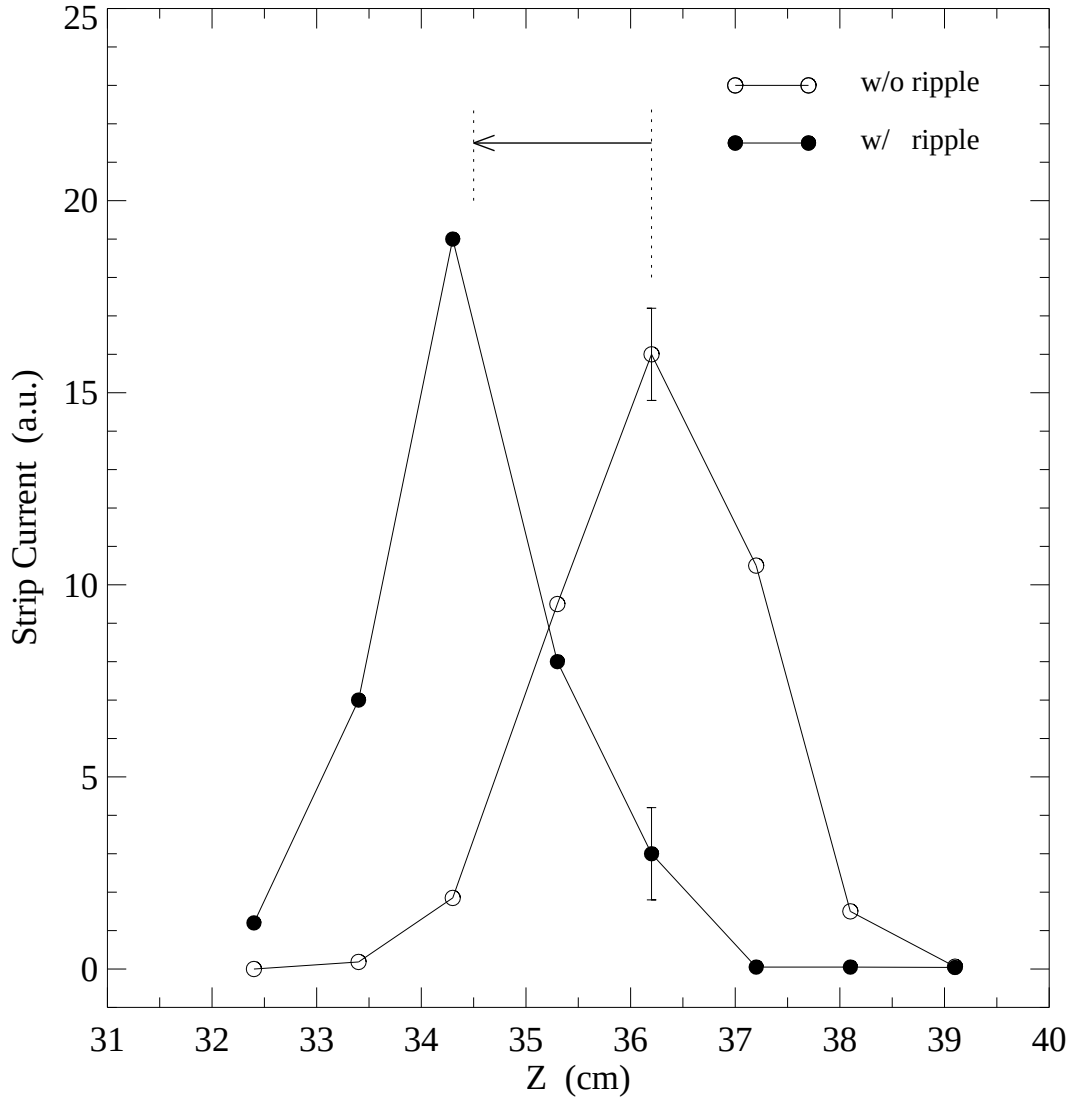

Figure 6.4: Vertical distribution of strip currents with the *Type I* ripple coils showing field line bending together with Fig. 6.3. $\delta = 3.5\,\%$.

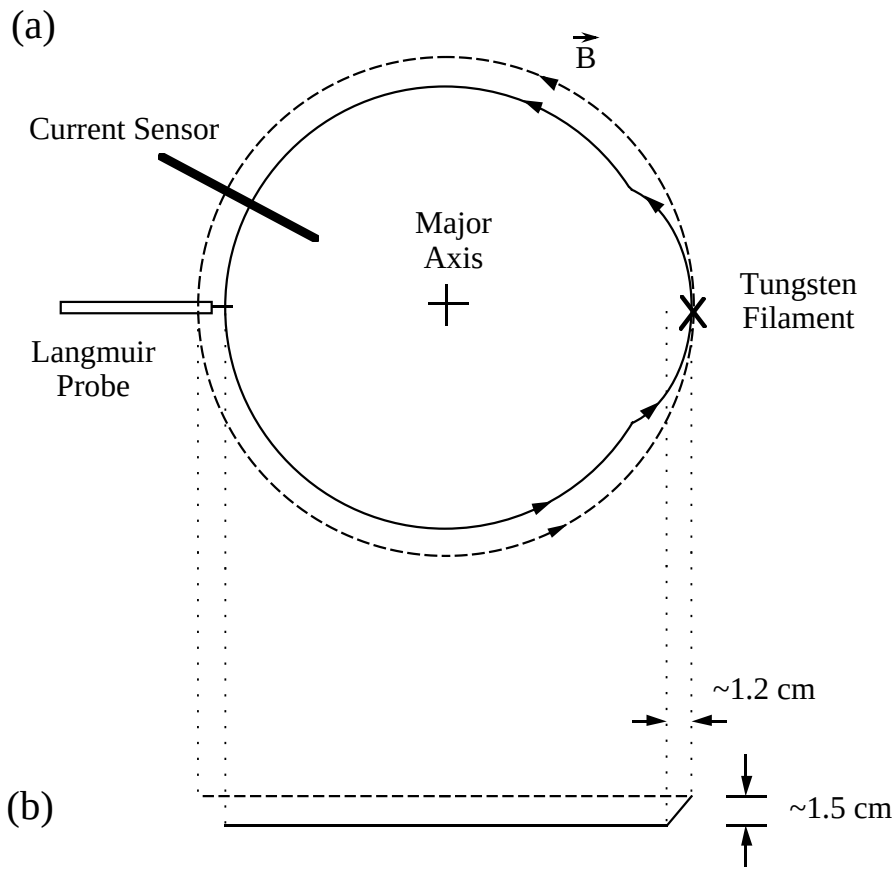

Figure 6.5: A simplified illustration showing a topology of a magnetic field line (a) looking down from the above, and (b) looking from side ways. Field line bending is caused by ripple fields. Broken line indicates the projection of an electron trajectory with toroidal fields only and the solid line denotes it in the presence of ripple fields (*Type I*). Not drawn to scale.

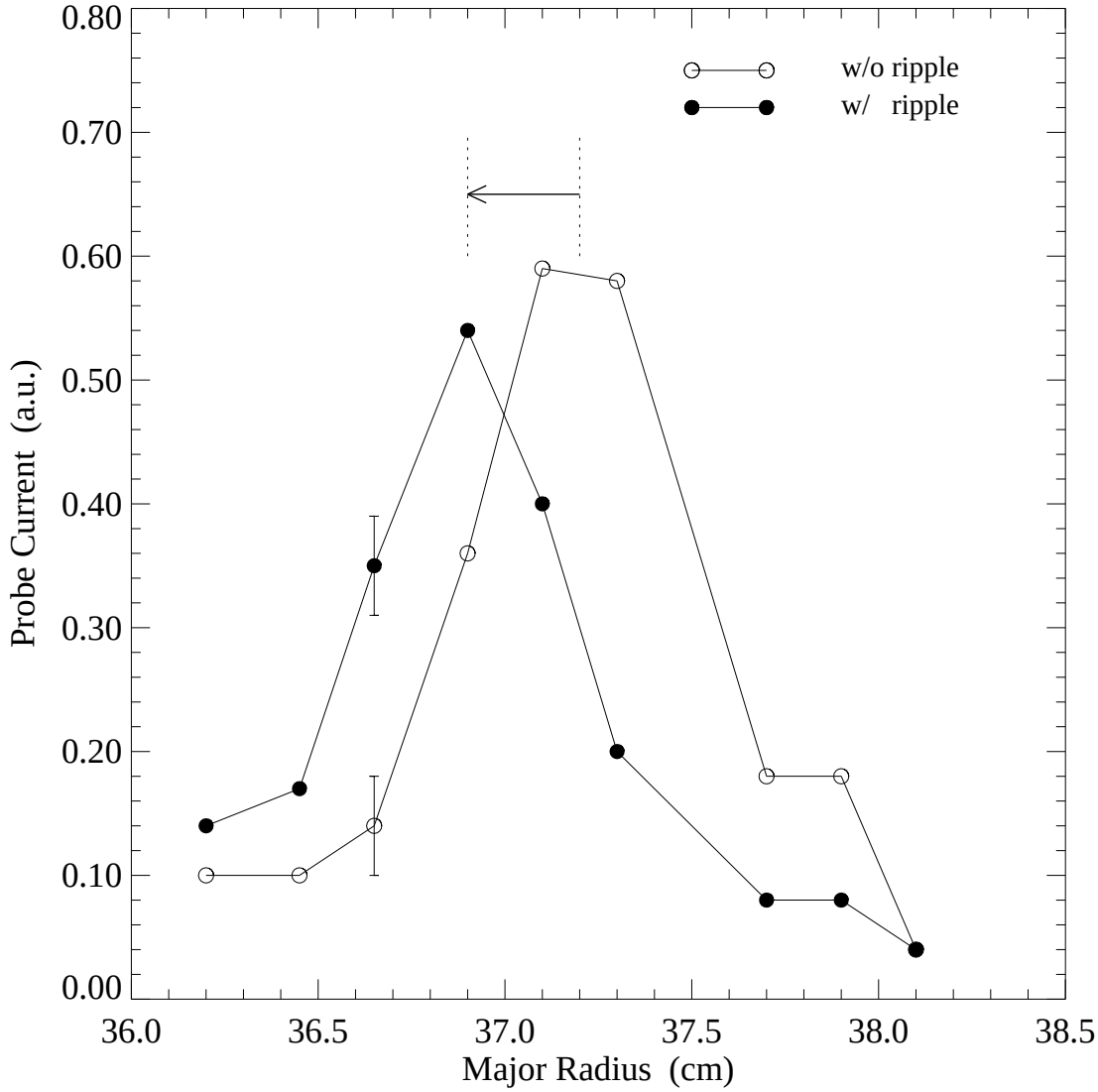

Figure 6.6: Radial profile of a Langmuir probe signal showing (major) radial bending out of field lines. With $\delta = 1.6\,\%$ from the ripple coil *TypeII*.

6.3 ECH and Ripple Trapping

Since it has been confirmed that electrons do drift (Fig. 6.2) and magnetic field lines bend (Fig. 6.3 – Fig. 6.6) as expected by the application of ripple fields, the next step is to study the effects of ripple trapping and electron cyclotron resonance heating. Hereafter, a toroidal magnetic field was applied and ripple fields by *TypeII* ripple coils were added to produce a small perturbation to the toroidal field. The corresponding field configuration is seen in Fig. 2.7 in Chapter 2. For the sake of simplicity, we define two different regions, *region 1* and *region 2* as unperturbed and perturbed (by the ripple magnetic field) region, respectively.

6.3.1 Observation of Limiter Currents in two regions

The experimental setup is illustrated in Fig. 6.7. In this setup, a hydrogen plasma was produced by $2\,kW$ of $2.45\,GHz$ microwave breakdown and simultaneously heated through cyclotron resonance heating at this frequency ($R_{res} = 37\,cm$). Two copper limiters, $0.16\,cm$ thick, $40\,cm$ long and $7.5\,cm$ high that encompass the whole radial extent of the CDX-U device were installed: one in *region 1* and the other in *region 2*. The limiters were located at the midplane of the chamber so that they could collect electrons drifting down by ∇B and curvature drifts. By comparing the two limiter currents, one can investigate the role of ripple fields and electron cyclotron heating.

Figure 6.8 shows the results of the limiter current measurements. The abscissae of the figure denotes the total current flowing in the ripple coils, which is approximately linearly proportional to the ripple strength at a fixed spatial position since the toroidal field is kept constant. Numerical calculations estimate that $5.25\,kA\cdot turn$ corresponds to $\delta \simeq 3\,\%$ at the resonance location. The ordinate of the figure denotes the difference of two limiter currents normalized by the current without ripple fields. The limiter currents in *region 2* are shown to increase as much as $50\,\%$ as the ripple strength increases.

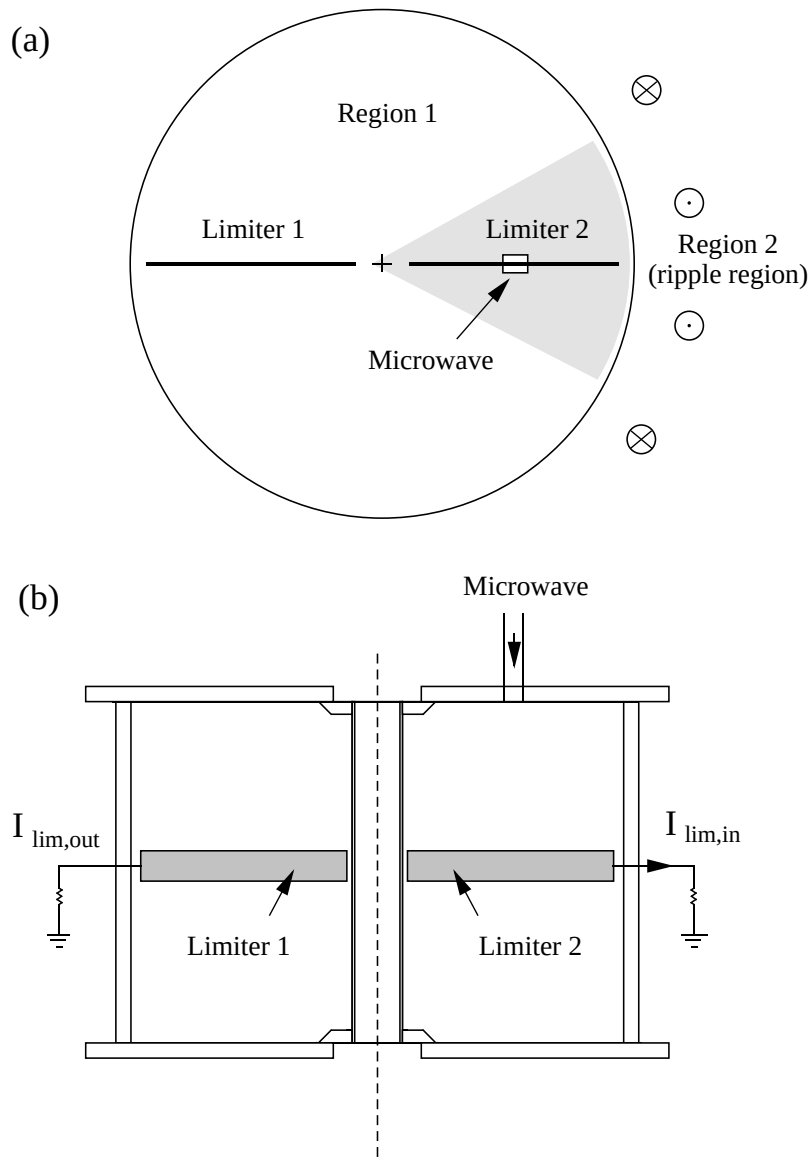

Figure 6.7: Experimental setup to study ripple trapping and ECH. (a) Plan view and (b) side view of CDX-U with ripple coils *TypeII*. Copper limiters cover a whole radial extent of the CDX-U device and are located at the midplane. Not drawn to scale.

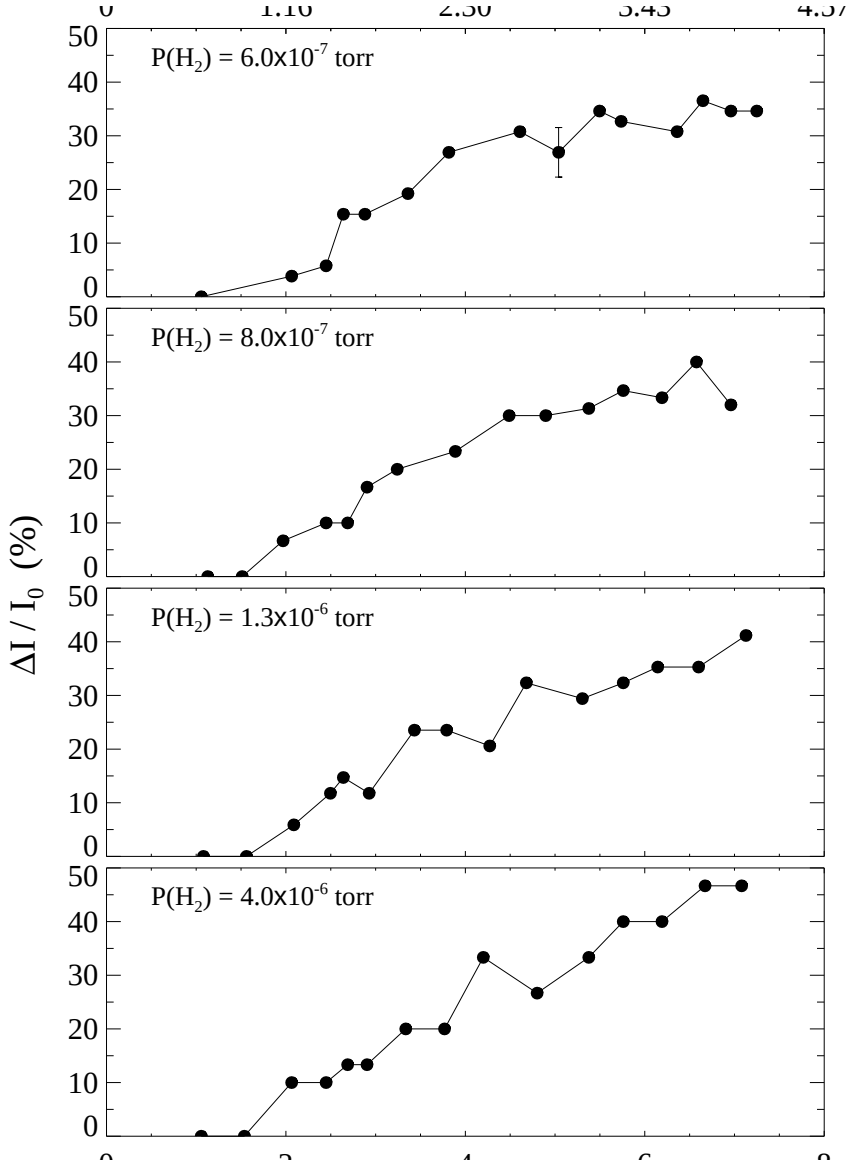

Figure 6.8: The difference of limiter currents in regions *1* and *2* where I_0 is the limiter current in the absence of ripple fields. The experimental arrangement is shown in Fig. 6.7 and only toroidal field and ripple fields are applied.

6.3.2 Density in terms of temperature anisotropy and ripple strength

In a relatively collisionless plasma where collisions are not sufficiently frequent to randomize particle motions perpendicular and parallel to the magnetic field, the pressure tensor can be anisotropic. In this section, we calculate the ratio of particle densities in two regions in terms of magnetic well depth and temperature anisotropy.

Let us start from the unperturbed region (*region 1*). With two characteristic temperatures, $T_\parallel$, $T_\perp$ with respect to the direction of magnetic field, the distribution function for an anisotropic medium is assumed to be bi-Maxwellian:

$$f_1 = \frac{n_1}{\left(\frac{2\pi k T_\parallel}{m}\right)^{1/2}\left(\frac{2\pi k T_\perp}{m}\right)}\ exp\left[-\frac{m}{2}\left(\frac{v_\parallel^2}{T_\parallel}+\frac{v_\perp^2}{T_\perp}\right)\right], \tag{6.1}$$

where n_1 is the electron density in *region 1*. As in a simple mirror geometry, the constants of motion in this case are the first adiabatic invariant, $\mu(= mv_\perp^2/2B)$, and the particle's total energy, w. Using conservation of μ and w, the exponent can be expressed as

$$\frac{v_\parallel^2}{T_\parallel}+\frac{v_\perp^2}{T_\perp} = \frac{\left(v_\parallel^2+v_\perp^2\right)}{T_\parallel} + \left(\frac{v_\perp^2}{B}\right)B_1\left(\frac{1}{T_\perp}-\frac{1}{T_\parallel}\right). \tag{6.2}$$

Since the distribution function is constant along any particle trajectory according to Liouville's theorem [Krall and Trivelpiece, 1973], we can write the distribution function in *region 2* as

$$f_2 = \frac{n_1}{\left(\frac{2\pi k T_\parallel}{m}\right)^{1/2}\left(\frac{2\pi k T_\perp}{m}\right)}\ exp\left[-\frac{m}{2}\left(\frac{v_\parallel^2}{T_\parallel}+\frac{v_\perp^2}{T_{\perp 2}}\right)\right], \tag{6.3}$$

where $T_{\perp 2}$ is defined from Eq. (6.2) with $B = B_2$:

$$\frac{1}{T_{\perp 2}} = \frac{1}{T_\parallel} + \left(\frac{B_1}{B_2}\right)\left(\frac{1}{T_\perp}-\frac{1}{T_\parallel}\right). \tag{6.4}$$

It follows from Eqs. (6.1) and (6.3) that parallel temperatures for both f_1 and f_2 are the same and only perpendicular temperatures are different in two regions. The electron density in *region 2* (n_2) is obtained by integrating f_2 over velocity space:

$$n_2 = n_1\ \frac{T_{\perp 2}}{T_\perp}. \tag{6.5}$$

By putting $T_\perp$ from Eq. (6.4) into Eq. (6.5), we get the density ratio expressed in terms of magnetic field ratio and the temperature anisotropy in *region 2* :

$$\frac{n_2}{n_1} = \frac{1 + s\ (m-1)}{m}. \tag{6.6}$$

where $m = B_1/B_2 = (1+\delta)/(1-\delta)$ with the ripple strength δ, and $s = T_{\perp 2}/T_\parallel$. As extreme cases, the above equation produces $n_2 = n_1$ for either $m = 1$ ($B_1 = B_2$) or $s = 1$ (isotropic distribution).

Equation (6.6) can also be obtained by a different approach. We write the distribution function in *region 2* as

$$f = f_N\ exp\left[-\frac{1}{T_c}\left(\frac{v_\perp^2}{s} + v_\parallel^2\right)\right], \tag{6.7}$$

where T_c and s are the characteristic temperature and temperature anisotropy in the perturbed region, respectively, and f_N is the normalization factor (that depends on T_c and s). Then the total density is expressed as

$$n_2 = \int d^3v\ f = \pi \int f\ dv_\perp^2\ dv_\parallel.$$

Choosing (w, μ) as coordinates produces the Jacobian, $\mathcal{J} = v_\parallel/B$. The passing particle density in the perturbed region is then obtained by integrating over passing velocity space:

$$\begin{aligned} n_{2p} &= \int_{pass} d^3v_2\ f \\ &= \frac{2\pi}{m^2}\int_{pass} f\ \frac{B_2}{v_{\parallel 2}}\ d\mu dw \\ &= n_2\left(1 - f_T\right), \end{aligned} \tag{6.8}$$

where n_2 is the total density, f_T is the trapped particle fraction in *region 2*, and $v_{\parallel 2} = \sqrt{2(w - \mu B_2)/m}$. Since the particles in the unperturbed region, however, are all passing, the density there can be written as

$$n_1 = \int_{whole} d^3v_1\ f$$

$$
\begin{aligned}
&= \frac{2\pi}{m^2}\int_{whole} f\ \frac{B_1}{v_{\|1}}\ d\mu dw \\
&= \frac{2\pi}{m^2}\int f\ \left(\frac{B_1}{B_2}\right)\left(\frac{v_{\|2}}{v_{\|1}}\right)\left(\frac{B_2}{v_{\|2}}\right)\ d\mu dw \\
&= \frac{2\pi}{m^2}\int_{pass} d^3v_2\ f\ \left(\frac{B_1}{B_2}\right)\left(\frac{v_{\|2}}{v_{\|1}}\right),
\end{aligned}
\tag{6.9}
$$

The Jacobian factor in the integration has its own physical meaning in this case: given a small tube of magnetic field lines, the number of particles with w and μ (constants of motion) passing various points on the tube should be proportional to the magnetic field strength since the cross sectional area of the tube is proportional to $1/B$ (flux conservation). On the other hand, the density should be inversely proportional to the parallel speed because particles speed up in the field direction in the weaker magnetic field region due to μ conservation. In other words, the parallel current is proportional to the field strength along a flux tube [Longmire, 1963]. The choice of (w, μ) as constants of motion in this case already assumes Liouville's theorem. $\left(v_{\|2}/v_{\|1}\right)$ in n_1 is obtained by using energy and μ conservation and it is given by

$$
\frac{v_{\|2}}{v_{\|1}} = \frac{\cos\varphi}{\sqrt{1-\left(\frac{B_1}{B_2}\right)\sin^2\varphi}},
\tag{6.10}
$$

where $\varphi = \arctan(v_\perp/v_\|)$. Calculation of n_2 and n_1 in Eqs. (6.8) and (6.9) using Eqs. (6.7) and (6.10) produces the same answer as Eq. (6.6).

In practice, the densities observed in *regions 1* and *2* consist of the cold background electron part (Maxwellian) and the warm electron part (anisotropic bi-Maxwellian) because not all the electrons are resonant with electron cyclotron waves. Denoting the subscript b (w) to stand for the background (warm) part, we can write

$$
\begin{aligned}
n_2^{tot} &= n_{2b} + n_{2w}, \\
n_1^{tot} &= n_{1b} + n_{1w}.
\end{aligned}
\tag{6.11}
$$

Since the background part has an isotropic distribution, the background densities in both regions are same and are independent of m following from Eq. (6.6). Letting

$n_b \equiv n_{1b} = n_{2b}$, and using Eq. (6.6) again for the warm part, n_b is expressed as

$$n_b = n_1^{tot} \frac{1}{s-1} \left[s - \frac{m \left(\frac{n_2^{tot}}{n_1^{tot}} \right) - 1}{m-1} \right]. \tag{6.12}$$

By knowing the magnetic field ratio m and the measured total densities in both regions, Eq. (6.12) should yield information about the temperature anisotropy s. In other words, the temperature anisotropy can be determined by two data points at each m subscribed by I and II with the help of the measured n_1^{tot} and n_2^{tot} by setting s to be constant with respect to m. That is,

$$\left(n_1^{tot}\right)_I \left[s - \frac{m_I \left(\frac{n_2^{tot}}{n_1^{tot}} \right)_I - 1}{m_I - 1} \right] = \left(n_1^{tot}\right)_{II} \left[s - \frac{m_{II} \left(\frac{n_2^{tot}}{n_1^{tot}} \right)_{II} - 1}{m_{II} - 1} \right]. \tag{6.13}$$

Another method is to plot Eq. (6.12) with a few data points and to find the crossing point of each curve.

6.3.3 Experimental determination of temperature anisotropy

In order to determine the temperature anisotropy in the ripple region based on Section 6.3.2, an experimental setup was prepared that was similar to that used for the limiter current measurements. A couple of Langmuir probes were utilized at the midplane instead of limiters. The analysis in Section 6.3.2 assumes that there are no collisions, as noted. Since the particle mean free path is much larger than the characteristic scale size of the device in the CDX-U plasma for this experiment, the collisionless assumption is valid.

The probe measurements show that the density in *region 1* decreases while the change of density in *region 2* is within the error bar as the ripple field is applied. This can be explained by considering the drift loss in the vertical direction. Provided that there is no loss, the density in *region 1* should be depleted and the density in *region 2* should increase because some electrons from *region 1* are trapped in *region 2* which is a magnetic well. At the same time, the temperature in *region 2* is higher (from Eq. (6.6)) resulting in more drift loss in *region 2* because the drift speed v_d is linearly proportional to $T_\perp$. Therefore, little change of the density in *region 2* suggests more drift loss there. This is seen in the limiter current measurements

shown in Fig. 6.8, where the limiter current due to vertical drifts in *region 2* is larger than that in *region 1*. This will be discussed more later in this section.

Figure 6.9 depicts the electron density measured in *region 1* (unperturbed region) at various major radial positions. The ripple coil current was held fixed in this figure so that each data point corresponds to a particular magnetic field line with each own ripple strength, in *region 2*. An open (closed) circle denotes the measured density in the absence (presence) of ripple fields applied in *region 2*. As is seen in the figure, the density reaches a maximum at $R \simeq 35\,cm$ which corresponds to the location of the electron cyclotron resonance layer. It shows that the density difference with and without the ripple field is large at points with large major radii even if the measuring locations are far away from the resonance layer. On the other hand, the difference decreases quickly for $R \leq 35\,cm$. This is because the ripple strength decreases toward small major radii positions (ripple coils are located at $R = 75\,cm$). At $R = 39\,cm$, the electron temperature obtained by the I-V characteristic is $10\,eV$ and the density estimated from the ion saturation current is $4 \times 10^{16}\,m^{-3}$.

After positioning a Langmuir probe at $R = 39\,cm$, the electron density in both regions was measured using several different ripple strengths, and Fig. 6.10 is the result. It should be noted here that n_2^{tot}/n_1^{tot} was obtained based on n_1^{tot} measurements since n_2^{tot} showed little change as discussed earlier. With the data points shown in Fig. 6.10 in hand, it is possible to estimate the warm electron temperature anisotropy in *region 2* by plotting Eq. (6.12). As is seen in Fig. 6.11, each curve crosses at $s \simeq 11.5$ and this is the electron temperature anisotropy at R $= 39$ *cm*. Given an electron temperature of $10\,eV$ from the probe measurement that is mostly a parallel temperature, the perpendicular temperature of warm electrons is estimated to be about $115\,eV$.

Since the main loss mechanism in this experiment is the drift loss, it would be instructive to compute the particle balance by comparing the drift loss rate and the ionization source rate. The drift loss rate, expressed as $n_{2w}\,v_d/L$ where L is the vertical scale length, is linearly proportional to the electron temperature (since $v_d \propto T_\perp$). The ionization rate is given by $n_{2w}\,n_H\,\langle\sigma v\rangle$, where n_H is the hydrogen neutral density and $\langle\sigma v\rangle$ is the Maxwellian-averaged ionization rate coefficient. Using $\langle\sigma v\rangle$ found from Ref. [Janev *et al.*, 1987] and a hydrogen neutral pressure of

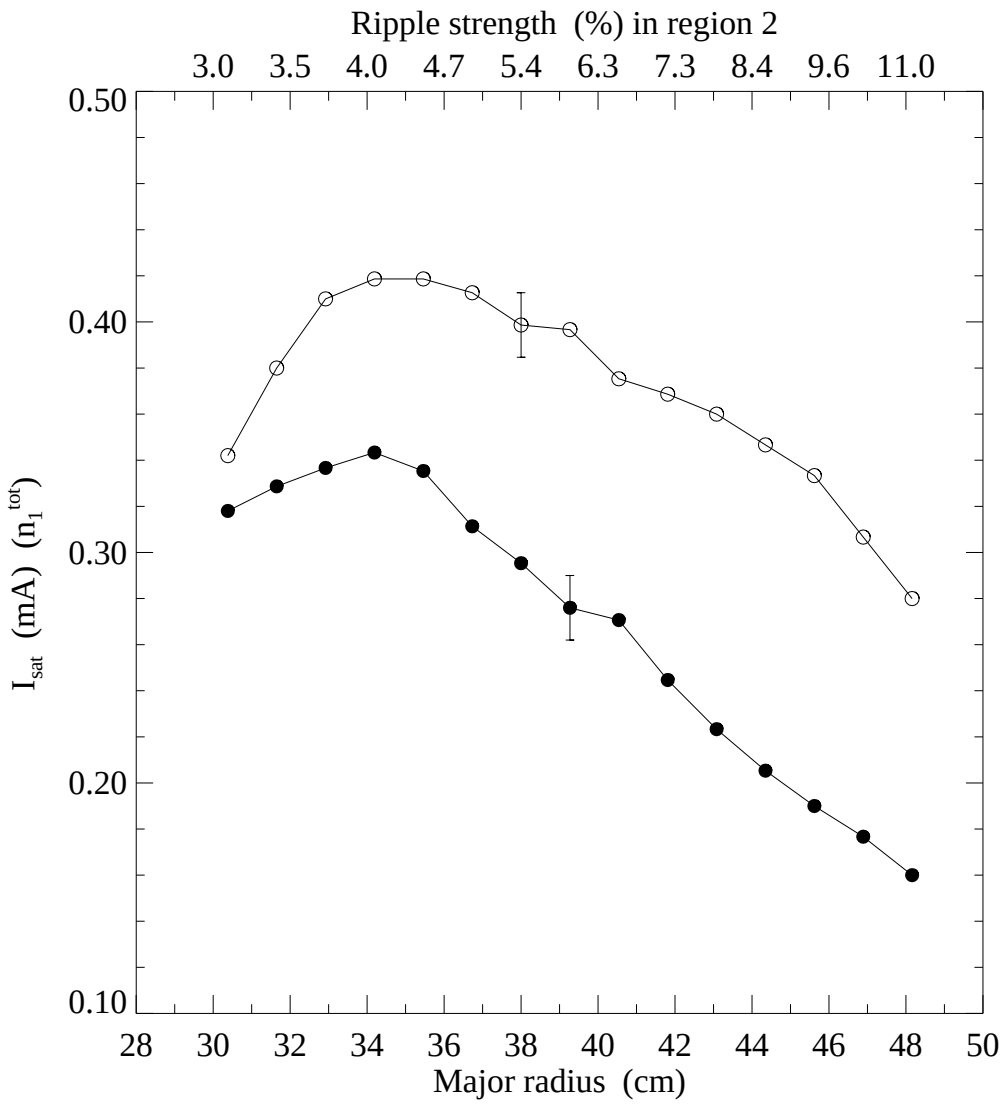

Figure 6.9: Electron density in *region 1* (unperturbed region) at various major radial positions. Open (closed) circle denotes the measured density in the absence (presence) of ripple fields applied in *region 2*. The electron cyclotron resonance layer locates at $R \simeq 35\,cm$.

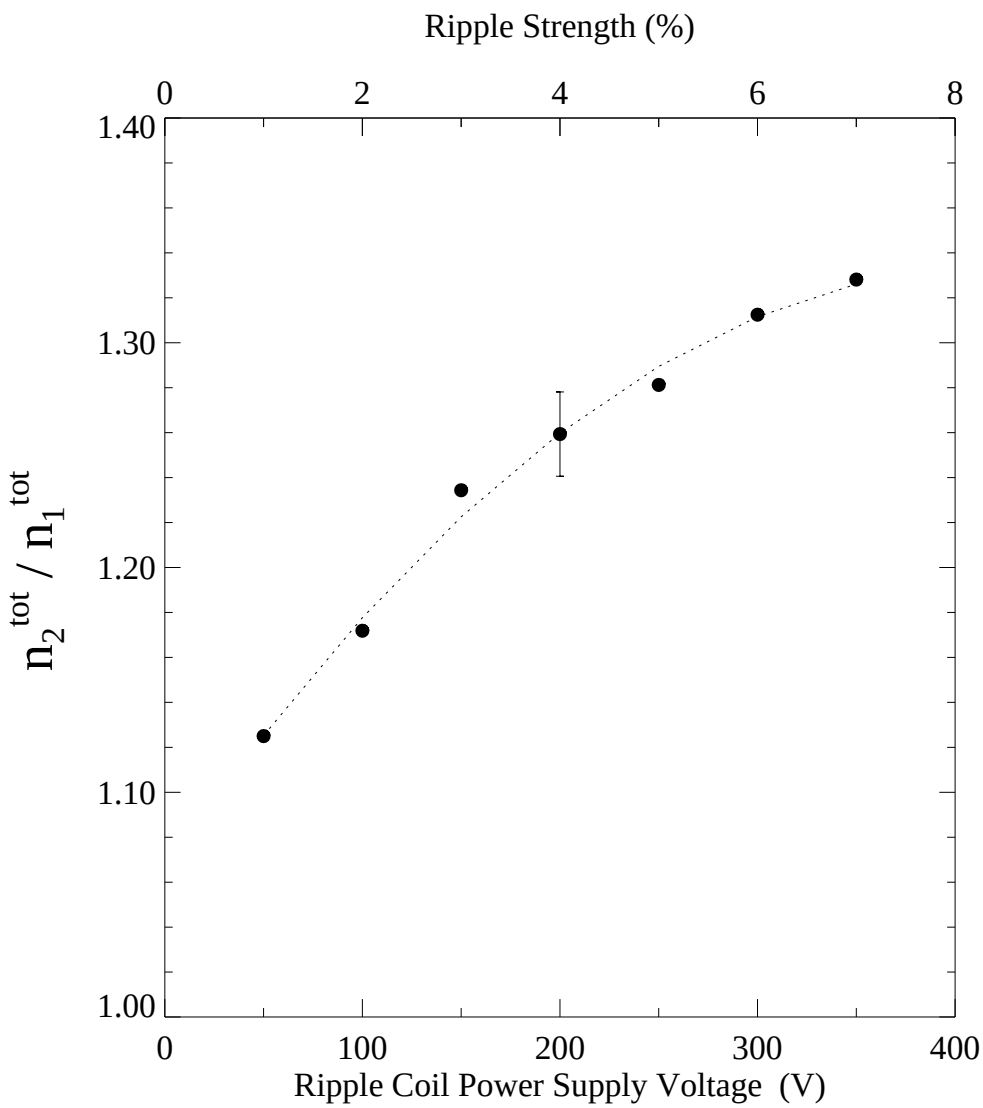

Figure 6.10: Total density ratio in two regions at various ripple strengths. At R = 39 *cm*.

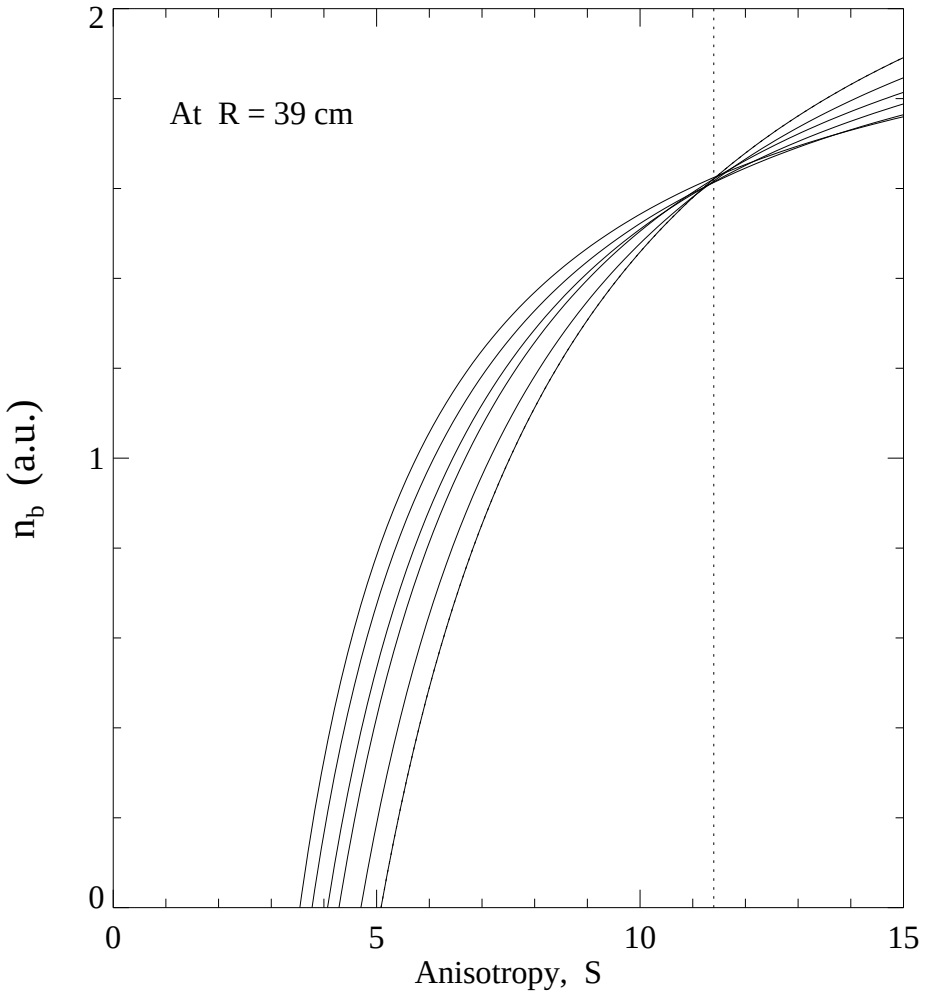

Figure 6.11: Plot of Eq. (6.12) with several different data points. Each curve indicates a data point in Fig. 6.10 with each ripple strength (or m). The crossing point indicates that the temperature anisotropy s is about 11.5. At R = 39 cm.

1×10^{-5} *torr*, the loss and source rates normalized by n_{2w} are compared in Fig. 6.12. The figure indicates that the two terms balance at $T_\perp \simeq 110\,eV$ which corresponds to the experimentally estimated perpendicular temperature in *region 2* as the above. It suggests that once the perpendicular temperature reaches this value by the application of a ripple field, more electrons are generated through the ionization process, but at the same time there is a greater loss of electrons through vertical drifts so that the two effects balance each other. This may explain why little change in the electron density was observed with a ripple field on in *region 2*.

The perpendicular temperature of warm electrons can be also estimated from the limiter current measurements and the drift loss rate considered in the previous paragraph. Since the limiter covers the whole radial extent of the CDX-U device, all the electrons that drift down would be collected by the limiter. In this case, the limiter current can be expressed as $I_{lim} \simeq n_{2w}\, V e\, v_d / L$ where V is the plasma volume. This gives a perpendicular temperature of approximately $70\,eV$.

Following the procedure described in Chapter 3, the analytic calculation of the electron temperature anisotropy has been attempted for this field configuration. The temperature anisotropy at the resonance surface is plotted in Fig. 6.13. For the parameter $d_e = P_\perp / n_{2w}\, kT_e\, \nu_0$ which is defined in Eq. (3.59), $1.67\,kW$ of wave power was assumed which is 67 % of the total input power utilized for electron resonance heating. (In order to justify this, the power used for the ionization of neutral hydrogen was estimated as the other main loss of input wave power. It turns out to be about 10 % of the input power, which suggests that the above assumption is not unreasonable). Using the resonant electron density n_{2w} obtained from Eqs. (6.11) and (6.12) with the determined temperature anisotropy ($n_{2w}/n_e \simeq 0.4$), d_e is about 6. At this d_e value, $T_\perp / T_\parallel = (7-9)$ at $Z_{eff} = (1-2)$ which is consistent with the experimentally determined value within a factor of two.

The same measurements have been done at different radial locations. Figures 6.14 and 6.15 show that the temperature anisotropies at $R = 43\,cm$ and $R = 48\,cm$ are about 8.5 and 7.0, respectively, suggesting that the temperature anisotropy becomes smaller at further away from the resonance layer.

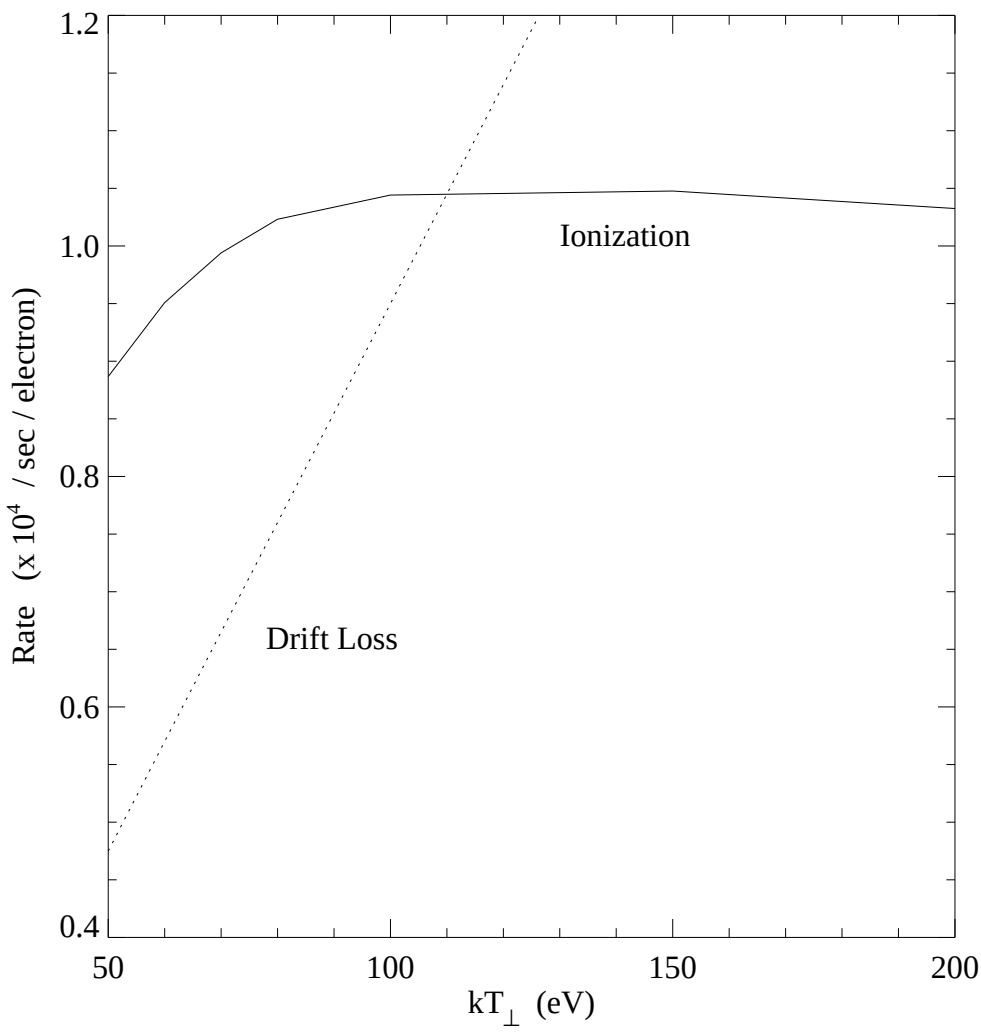

Figure 6.12: Ionization source rate versus drift loss rate of electrons as a function of electron temperature. The two terms balance at $110\,eV$ which corresponds to the experimentally determined perpendicular temperature in *region 2*. The rates are divided by the electron density.

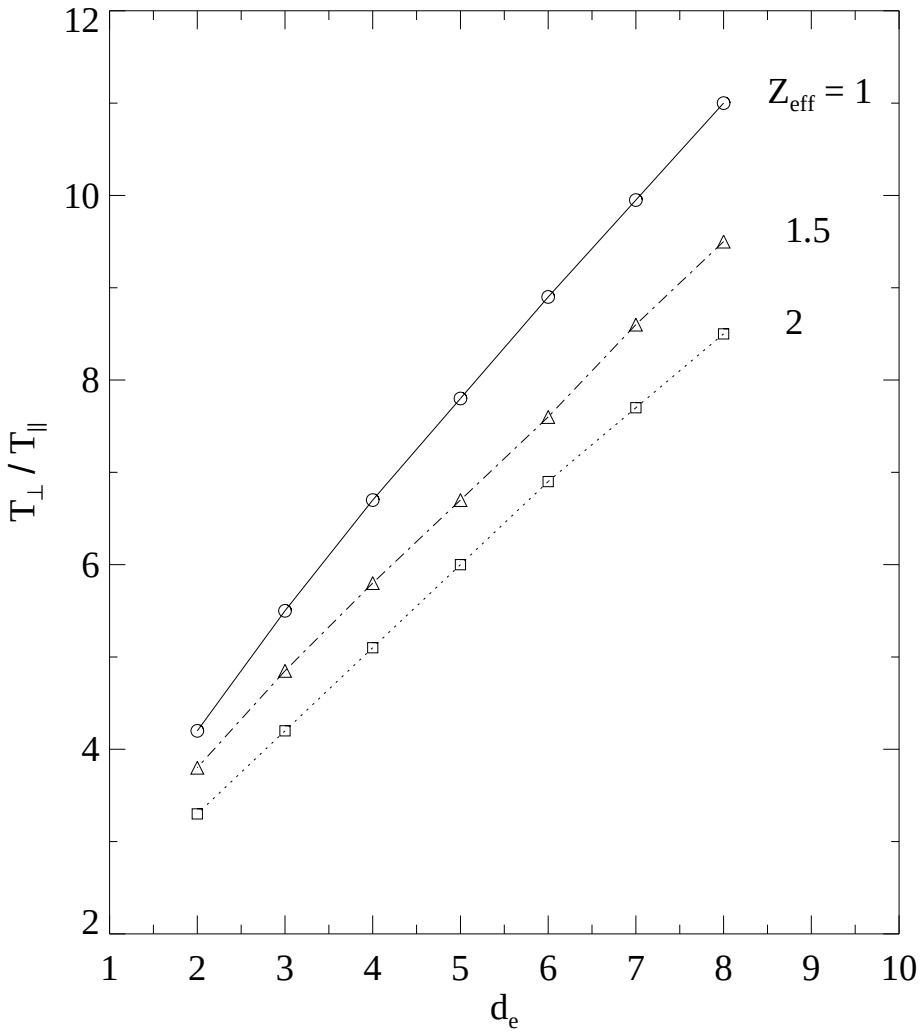

Figure 6.13: Analytically calculated warm electron temperature anisotropy at the resonance layer. $\delta = 5\,\%$ and $\nu_L/\nu_0 = 0.01$.

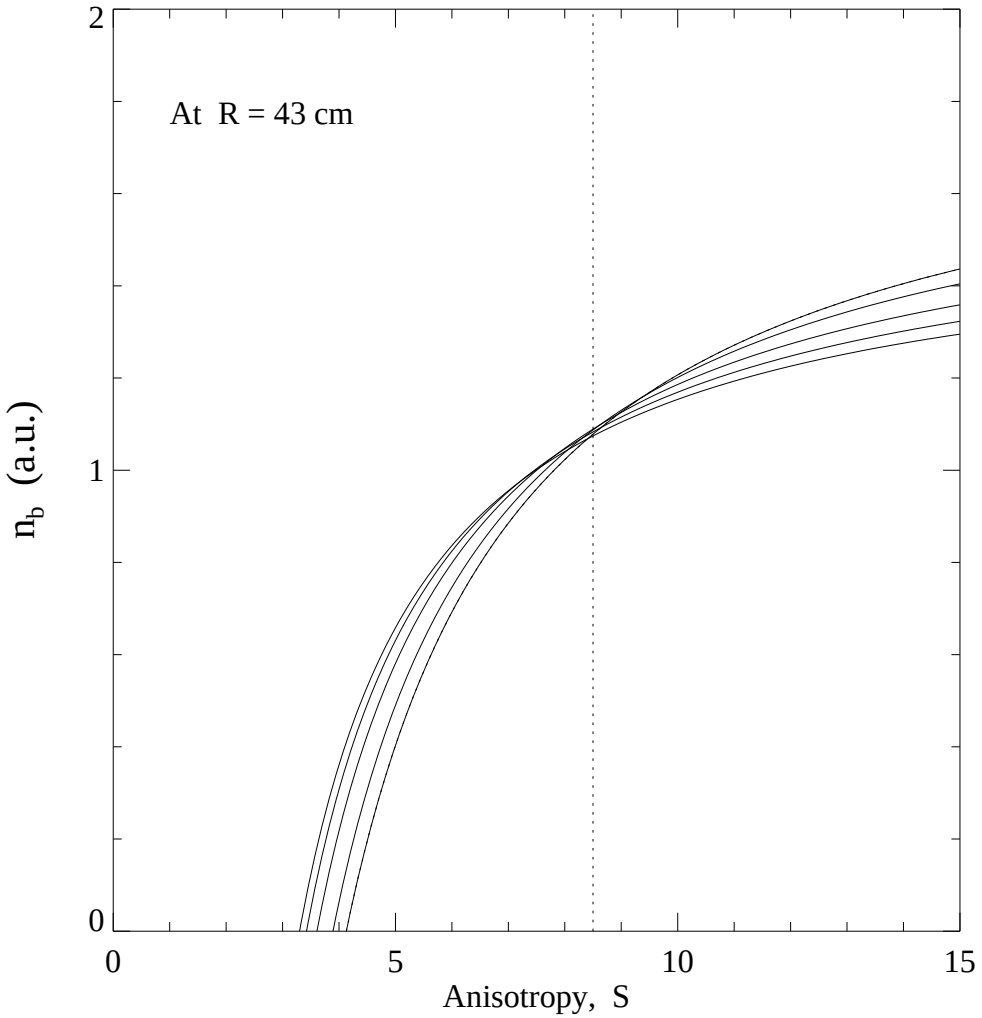

Figure 6.14: Similar plot as Fig. 6.11 at R = 43 *cm*.

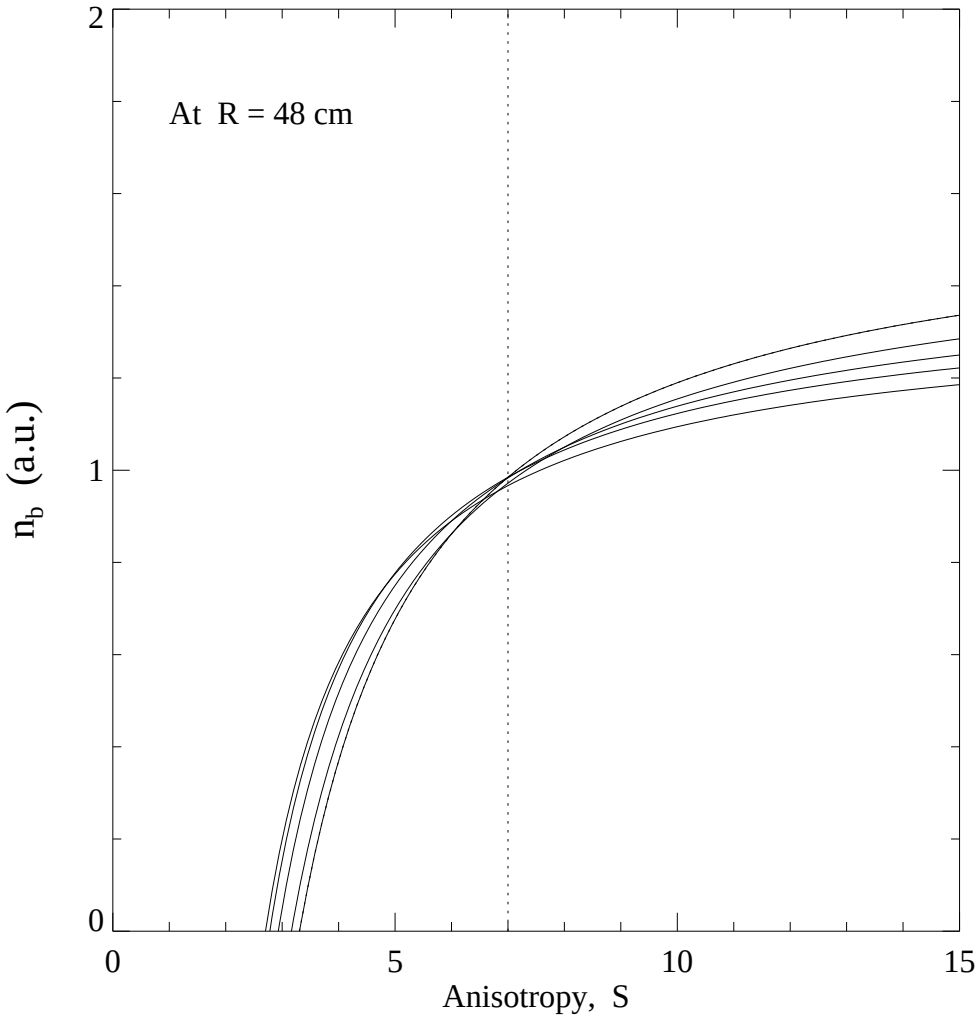

Figure 6.15: Similar plot as Fig. 6.11 at R = 48 *cm*.

6.4 Summary

In this chapter, experiments with a few different setups have been done with different goals. For the sake of simplicity, only a toroidal field was provided and an additional ripple field was applied locally with a ripple strength of a few percent, if necessary.

Firstly, the electron drifts (∇B and curvature) were confirmed to have the expected direction. When the toroidal field was reversed, the drift direction was also reversed. Secondly, the topology of magnetic field lines was studied with two different types of ripple coils. The probe and current sensor measurements of electrons emitted from a tungsten source show a radial and vertical excursion due to a ripple field, and the excursion distance is consistent with numerical calculations. Thirdly, the temperature anisotropy of warm electrons generated by cyclotron resonance heating and particle trapping was experimentally determined by measurements of electron densities in both unperturbed and perturbed regions. Results show that the temperature anisotropy is approximately 11 and this value is obtained based on the collisionless model. The estimation from the limiter current measurements gives that it is about 7. On the other hand, the value derived by kinetic calculation is $(7-9)$ depending on $Z_{eff} = (1-2)$. From this, we can conclude that the measured temperature anisotropy of warm electrons reasonably agrees with the analytically calculated value within a factor of two.

Chapter 7

Emissive Limiter Bias Experiment on CCT

IN ADDITION TO the electron ripple injection technique, another approach has been taken utilizing electron injection for tokamak plasma confinement improvement.

When H-mode was discovered in ASDEX, it was only observed in divertor discharges, and H-mode did not develop in limiter discharges. Due to these observations, H-mode was at first considered to be accessible only in diverted plasmas but a few years later it was also observed in limiter plasmas [Shimada *et al.*, 1985; Conn *et al.*, 1987; Phillips *et al.*, 1987; Matsumoto *et al.*, 1987a; Matsumoto *et al.*, 1987b; Odajima *et al.*, 1987; Sengoku *et al.*, 1987; Schissel *et al.*, 1989; Toi *et al.*, 1989; Burrell *et al.*, 1989; Couture *et al.*, 1990; Shimada *et al.*, 1990; Bush *et al.*, 1990; Bush *et al.*, 1991; Bush *et al.*, 1994]. Since the discovery of H-mode, plasma biasing by various means has been a useful way of inducing H-mode, and especially there have been several excellent H-mode experiments regarding biasing limiters. In PBX [Shimada *et al.*, 1985], a negative bias voltage up to $-290\,V$ was applied to the limiter with respect to the vessel wall. As a result of biasing, the averaged electron density increased by $10\,\%$ at a constant rate of gas puffing and H_α emission at the wall decreased by a factor of two. The improvement of plasma energy confinement time was about $4\,\%$. The limiter current was $140\,A$ when the bias voltage was less than $-180\,V$ but decreased to $50\,A$ when V_{bias} increased to $-290\,V$. In TEXTOR [Conn *et al.*, 1987], TEXT [Phillips *et al.*,

1987], DIII-D [Shimada *et al.*, 1990], and Tokamak de Varennes [Couture *et al.*, 1990], positive biasing as well as the negative biasing was attempted and better results were generally obtained with negative biasing. Results from DIII-D showed an improvement in plasma particle confinement time inferred by steeper density gradient and smaller particle flux at the edge region. Similarly, the global particle confinement time increased by 20 % and the radial electric field was $\sim 100\ V/cm$ in the TEXT experiments. In Tokamak de Varennes, the bias voltage was scanned to see how sensitive parameters such as density, H_α, neutral pressure and impurity flux were with respect to the applied voltage. They observed a simultaneous steepening of the density gradient at the edge and the reduction of Z_{eff}.

In the DC-helicity injection experiments of CDX [Darrow, 1988; Ono *et al.*, 1989], it was discovered somewhat unexpectedly that a DC-helicity driven tokamak has a negative potential well as shown in Fig. 7.1. Because of the negative potential in the plasma, a dc radial electric field was created, and as a result, poloidal rotation of the plasma with a typical rotation velocity of $\sim 1\times10^4\ m/sec$ was observed. Based on the measurements, the radial electric field in the gradient region scales typically as $E_r\,(V/m) \approx 1.1\times10^3\ B_T\,(kG)/\sqrt{\mu}$, where μ is the ratio of main ion mass to proton mass. The depth of the negative potential well is about 1/2 to 1/3 of the value of the cathode voltage. One of the possible explanations for the generation of potential well is that the hot electrons which can move relatively quickly along magnetic field lines may diffuse toward plasma center, perhaps due to the stochasticity of the field lines at the plasma edge. This experimental observation suggests that a radial electric field can be created inside plasma by at least a few cm by actively injecting hot electrons from the plasma edge. The experiment presented in this chapter is motivated by observations in CDX experiments and thus, in contrast to other plasma biasing experiments mentioned in the previous paragraph, it has a uniqueness in that it utilizes a novel scheme of an emissive electrode both to charge up the plasma and to define the plasma as a limiter.

The CCT tokamak and the related LaB_6 cathode assembly with which this experiment was performed is briefly described in Section 7.1. In Section 7.2, results are shown when the limiter is biased negatively without being heated. Section 7.3 presents experimental results when the limiter is heated so that it emits electrons. Finally, conclusions and possible applications of this idea in future machines are

described in Section 7.4. This experiment was done as a collaborative work between the UCLA CCT group and the PPPL CDX-U group.

7.1 Description of the Experimental Setup

Figure 7.2 depicts a cross-sectional view of the Continuous Current Tokamak (CCT) located at the University of California at Los Angeles. The CCT vacuum vessel is made of 1 cm thick stainless steel and has an insulating break to prevent eddy current from flowing in the toroidal direction. The loop voltage developed is measured across this insulating break. Inside the vacuum vessel, 3 mm thick copper panels line the vessel and this copper liner also has several breaks both toroidally and poloidally. The diameter of the liner is 80 cm so that the plasma can be as much as 40 cm in minor radius. The major radius of CCT is 1.5 m and it was operated with $I_p = (30-40)\,kA$, $B_T = 0.3\,T$, and $n_e = (1-6)\times 10^{18}\,m^{-3}$. The cathode used as a limiter in this experiment was located at the top of the device ($\theta = 90°$), at a single toroidal location as seen in Fig. 7.2. It was made of carbon-heated lanthanum hexaboride (LaB_6) and the description of its construction can be found in several references [Ono *et al.*, 1987; Darrow, 1988; Darrow *et al.*, 1990]. The cathode assembly is composed of 18 beads whose diameter is 1.9 cm and is strung onto a carbon rod. This carbon rod is heated electrically, and the beads are in turn heated by this rod to become sufficiently hot to emit electrons. As shown in Fig. 7.2(b), tungsten plates, of size 13 $cm \times 10\,cm$, are placed on both sides of the cathode with openings for the LaB_6 beads. Since the beads are open on both sides toroidally, the electrons emitted follow field lines in both directions. The assembly is biased negatively with respect to the vacuum vessel, so that the vessel acts as an anode in this case.

7.2 Limiter Biasing and H-mode Transition

When the limiter bias exceeded a certain voltage, transition to H-mode could be obtained. Figure 7.3 shows the temporal evolution of various plasma parameters when the limiter is located at 15 cm inside the wall and biased at $-450\,V$. At 39 $msec$ the bias voltage is applied to the limiter and at the same time injection current through

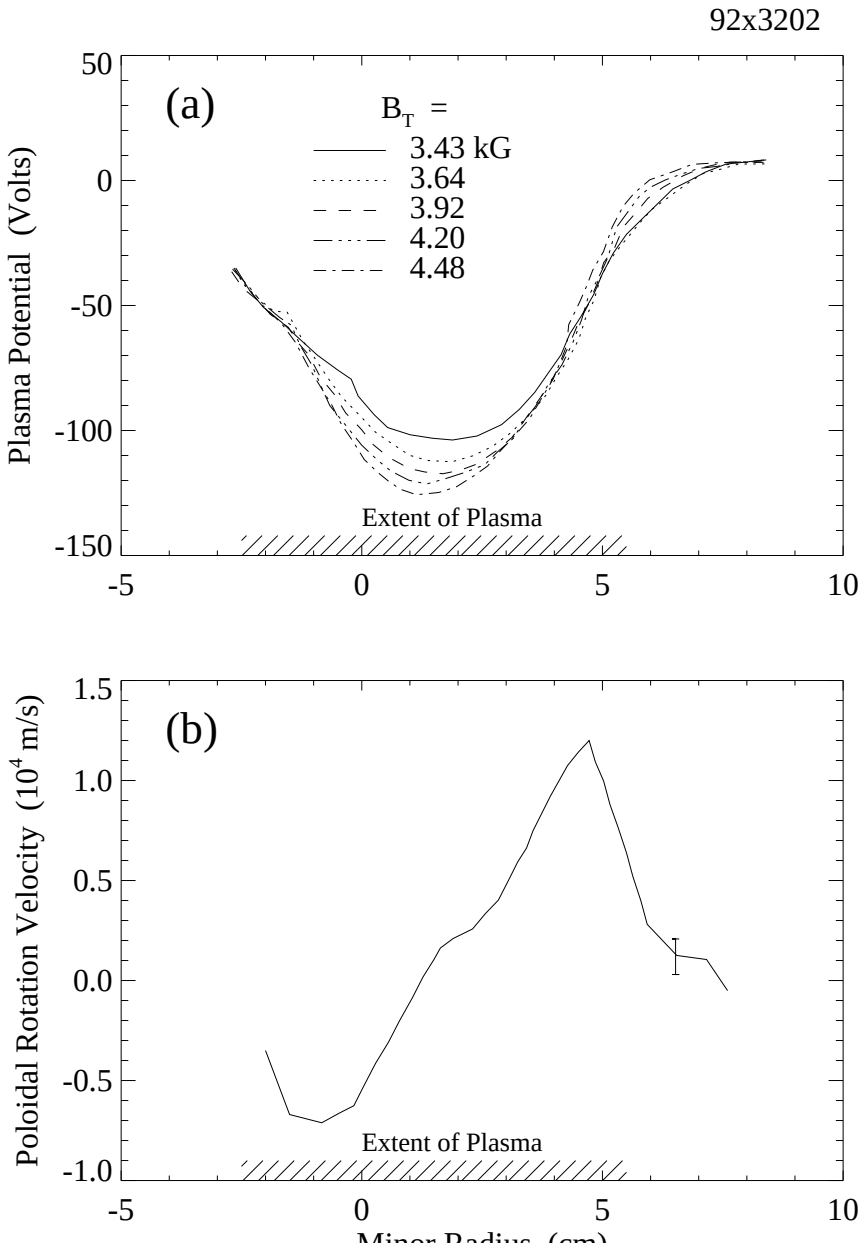

Figure 7.1: (a) The plasma potential, as measured by the emissive probe, during the CDX hydrogen discharges at different toroidal fields. (b) The poloidal rotation speed inferred from (a).

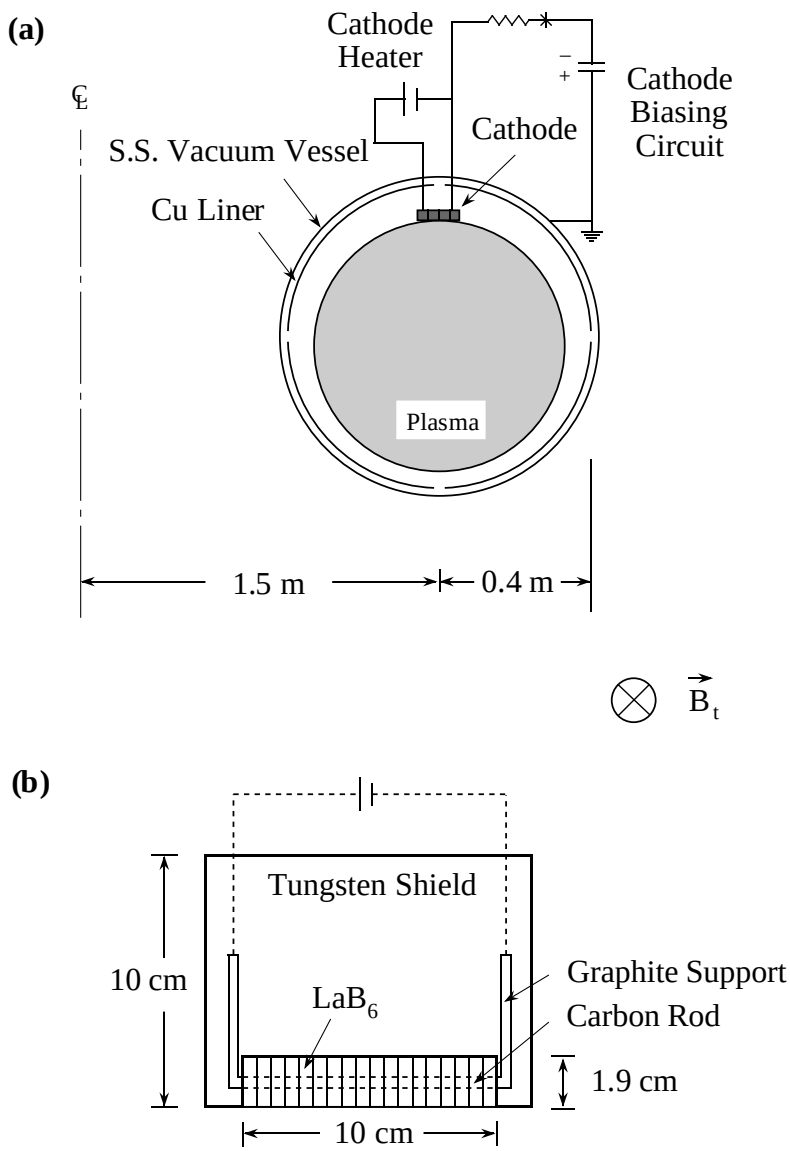

Figure 7.2: Cross-sectional view of CCT and the cathode limiter assembly. (a) Cathode is located inside the copper liner whose minor radius is 40 cm. In this experiment the cathode was inserted up to 15 cm from the liner. (b) 18 LaB_6 beads are open in the toroidal direction and are heated by a carbon rod.

the limiter begins to flow. I_{inj} continues to increase up to $\sim 80\,A$ and then suddenly drops to $\sim 40\,A$ at $72\,msec$ ($33\,msec$ after biasing), implying that the transport of emitted electrons from the cathode to the copper liner has decreased and that the confinement of the plasma is improved. Line-integrated electron density also starts to increase at this time of transition to H-mode. The H-mode lasts for $\sim 8\,msec$ and then an abrupt rise in UV light due to impurities appears, thereafter leading to a plasma disruption. In this paper, an H-mode transition is defined by the decrease of injection current and loop voltage, a drop of impurity line spectrum intensity, and a subsequent increase of plasma density. In contrast, when the limiter was biased by $-250\,V$, no H-mode transition was observed and the plasma remained in L-mode. This triggering of transition with high bias voltage may be explained by the plasma ion bombardment to the limiter. Initially the 'injected' current caused by the biased limiter is due to plasma ion flow to the limiter itself, but once the limiter surface is heated up due to these bombarding ions, the current can be attributed to thermionically emitted electrons from the limiter. At a higher bias voltage, ions collide with the limiter at a higher energy resulting in a more effective heating of the LaB_6 cathode and producing electrons sooner after the bias is applied.

In order to support this hypothesis, a simple numerical estimate of the time required for the LaB_6 surface to reach $\sim 1200\,℃$ was made by solving the time dependent heat conduction equation assuming a slab geometry. Since the thermal conductivity of this material ($k = 48\,W/mK$) is relatively small compared to the heat transfer coefficient of the plasma ($h = 4.6 \times 10^4\,W/m^2K$) (i.e., Biot number $B_i = hD/2k \gg 1$ where D is the diameter of a LaB_6 ring), the penetration depth of the heat flux from one side of the boundary is much shorter than the size of the cathode. In other words, the temperature is peaked near the surface and rapidly drops off away from the surface.

According to this estimate, the time to get to approximately $1200\,℃$ is about $60\,msec$, which is the same order of magnitude as the measured delay time ($33\,msec$). Additional heating is expected from the plasma which would further reduce the required time.

Based on this explanation, $-250\,V$ is too low a potential to heat the cathode and provide the sufficient radial current. Therefore, there is a threshold to induce the transition, which is between $-250\,V$ and $-450\,V$. This suggests that a limiter

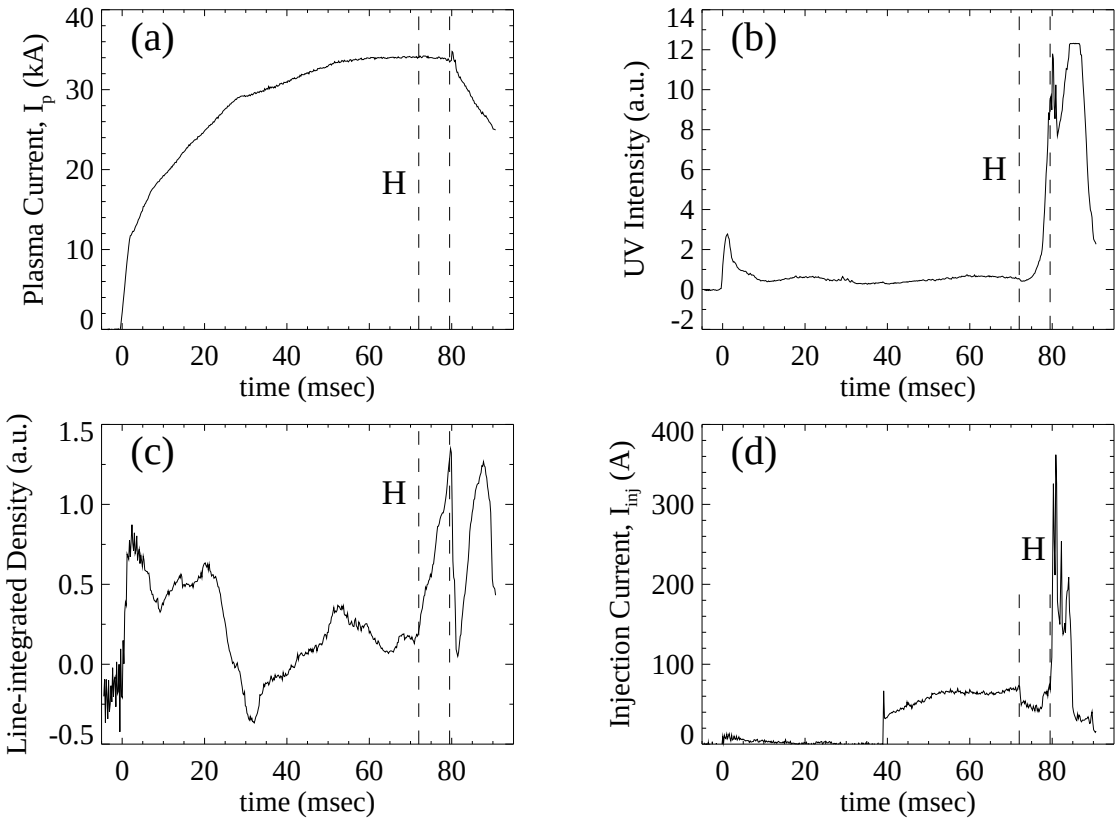

Figure 7.3: Time trace of main plasma parameters when the limiter was biased at $-450\,V$ and was not heated. Ohmic discharge began at $0\,msec$ and the bias was applied at $39\,msec$. The bifurcation was observed at $72\,msec$ when the line-integrated density increased and the injection current decreased.

with an emissive surface would initiate the bifurcation in a more effective way. The electrons emitted will charge up the plasma negatively, producing a local radial electric field layer at the edge region which is believed to play an important role in obtaining H-mode.

7.3 Results with Emissive Limiter

In order to see the effect of electrons emitted from the limiter, the limiter was heated by a carbon rod which supported 18 LaB_6 beads as shown in Fig. 7.2(b). The heater was turned on all the time including the period when a negative bias voltage was applied. The factor which determined the limiter temperature was the current flowing in the heater circuit.

(a) Location of the plasma edge

Finding out the location of the plasma edge is important in this experiment to confirm the role of the cathode as a limiter.

First, for the H-mode transition, it was important to position the plasma so that the cathode acts as the primary limiter. When the limiter was inserted into the vessel well away from the liner, the position control was relatively easy. As the limiter was moved closer to the liner, the plasma positioning became more critical in obtaining the H-mode transition since the plasma could easily touch the liner, causing the cathode current to flow directly into the liner, thereby preventing a charge up of the plasma.

Second, with a fixed bias voltage ($V_{bias} = -220\,V$) and cathode temperature ($I_{heater} = 320\,A$), a series of shots were taken by varying the physical locations of the cathode. Figure 7.4 shows the contour plot of the electron density from the multi-tip Langmuir probe array. The probe array, having 10 tips which were 1 cm apart from each other, was inserted into the vessel to measure the floating potential and the electron density. It was located at the top of the device ($\theta = 90°$), at a single toroidal location but not close to the cathode. The ordinate of the figure is the normal distance measured from the copper liner. As shown in the figure, the electron density increased at 39 $msec$ when the bias voltage was applied and there were regions of the steep density gradient. The position of the cathode bottom end is 9 cm and 13 cm for Fig. 7.4(a) and (b), respectively. Since the diameter of a LaB_6

bead is 1.9 cm, the region of steep density gradient matches well with the location of the cathode, which means that the edge of the plasma can be identified by the position of the cathode.

(b) Typical H-mode shot with a fully heated cathode limiter

Figure 7.5 shows the evolution of the plasma current, loop voltage, injection current, line-integrated density, and UV emission of a typical H-mode shot with the heated cathode limiter. For this shot, the limiter was located at 15 cm inside the liner and was heated with heater current of 300 A and biased by $-250\,V$ from 39 $msec$. As shown in the figure, the UV spectrum decreased and, simultaneously, the electron density measured by the *8 mm* microwave interferometer began to increase, indicating the start of H-mode. The injection current was measured to be as low as 30 A, which was much less than $\sim 100\,A$ for L-mode plasmas. After $t = 84\,msec$, giant sawteeth began to develop which led to the disruption of the plasma. The loop voltage for a series of H-mode shots including the one in Fig. 7.5 remained at between $0.9\,V$ and $1.1\,V$, which was less than that ($\sim 1.6\,V$) of L-mode plasmas, suggesting an improvement of the energy confinement time (beyond the usual improvement due to the density rise). One thing to notice here is that when the limiter is heated, the transition occurs immediately after the imposition of the bias voltage to get into the H-mode state. In Fig. 7.6, a time delay from the beginning of biasing to the onset of H-mode in three different cases is compared. With a limiter that was biased ($V_{bias} = -450\,V$) but unheated ($I_{heater} = 0\,A$), the observed time delay was about 33 $msec$. When $V_{bias} = -250\,V$ and $I_{heater} = 250\,A$, the delay time was less than 10 $msec$. This may be related again to the required time for the self-heating of the cathode to reach the emissive temperature. As discussed previously, the H-mode transition could be seen at a lower bias voltage as long as the limiter was hot enough to emit electrons thermionically. The low bias voltage also probably helps to reduce the impurity content caused by sputtering due to the application of high voltages to the limiter.

Figure 7.7 shows the time history of floating potentials at 4 probe tips that are located at 9, 11, 13, and 15 cm from the liner. The radial electric field is obtained from the plasma potentials, $V_p = V_f + 3kT_e$, of two probe tips located at 9 and 15 cm from the liner respectively, assuming a constant electron temperature around the plasma edge region. The floating potential which was measured by this

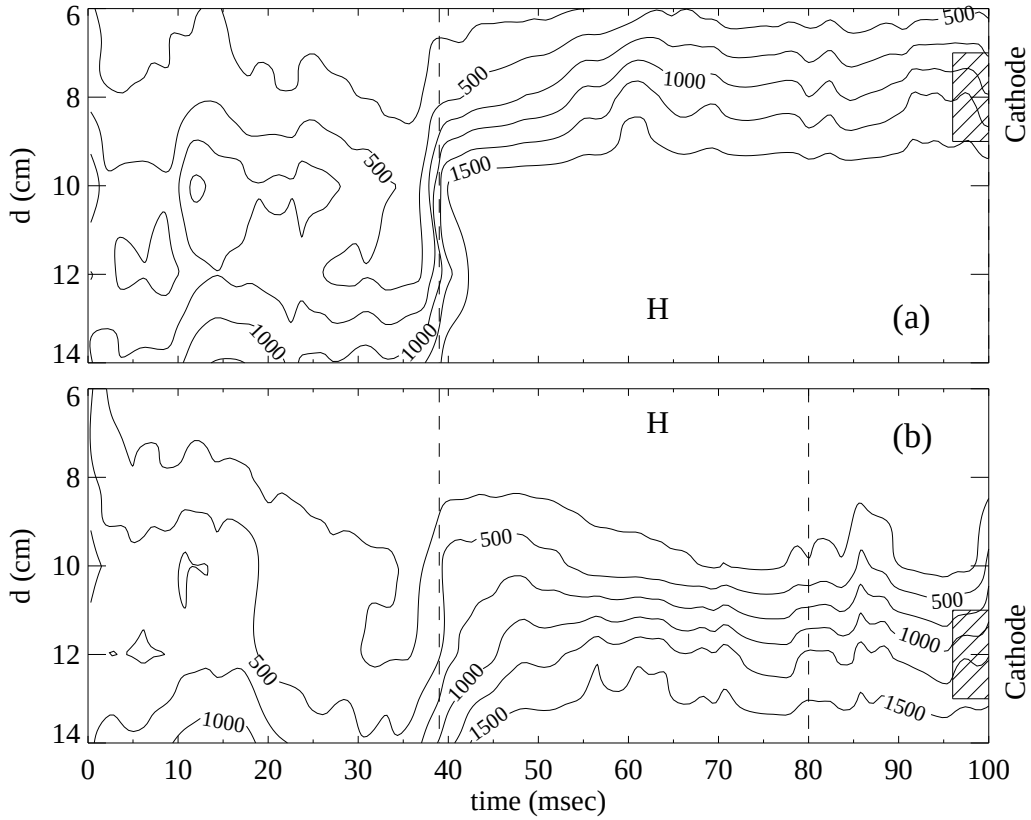

Figure 7.4: Contour plot of electron density (a.u.) from the multi-tip Langmuir probe array. The ordinate indicates the distance from the copper liner. The cathode is placed (a) from $d = 9\,cm$ to $7\,cm$, and (b) from $13\,cm$ to $11\,cm$ in the plot. For these shots, $V_{bias} = -220\,V$, and $I_{heater} = 320\,A$. H-mode occurs from $39\,msec$ for (a) and from $39\,msec$ to $80\,msec$ for (b).

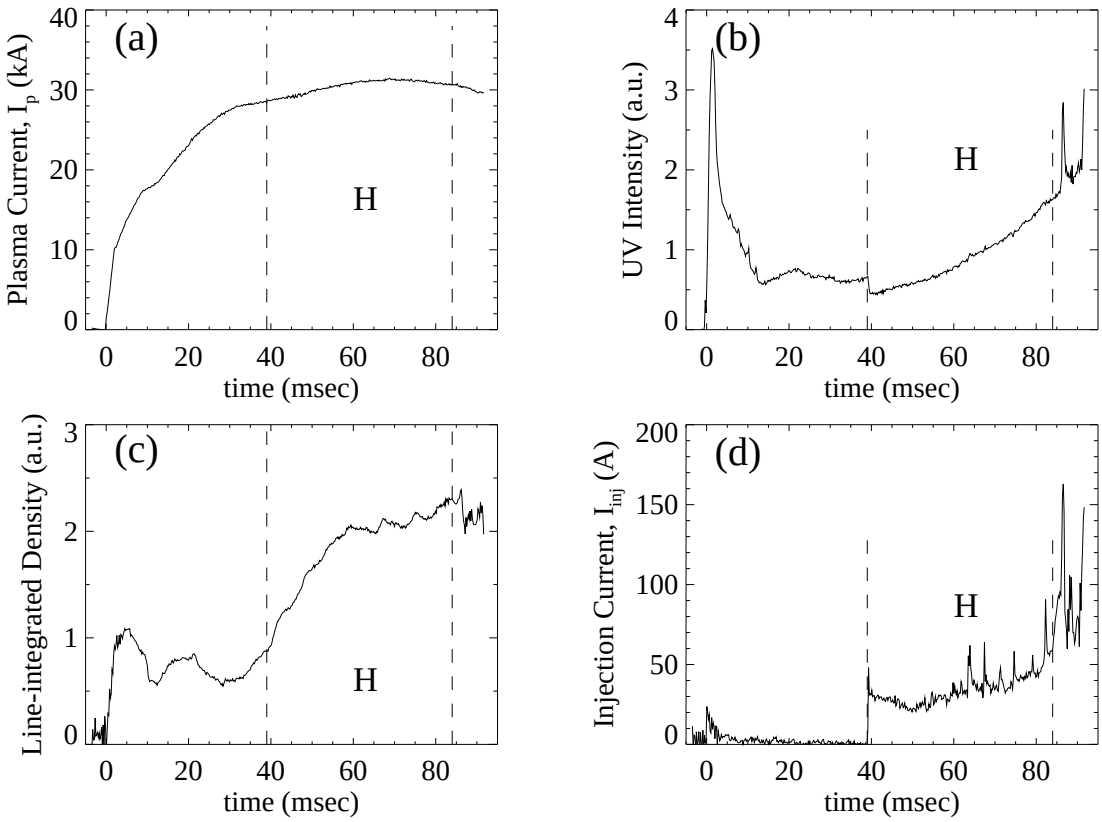

Figure 7.5: Evolution of plasma parameters of a typical H-mode when the limiter was heated ($I_{heater} = 300\,A$) and biased by $-250\,V$. Biasing began at $39\,msec$ and the transition followed immediately after the biasing.

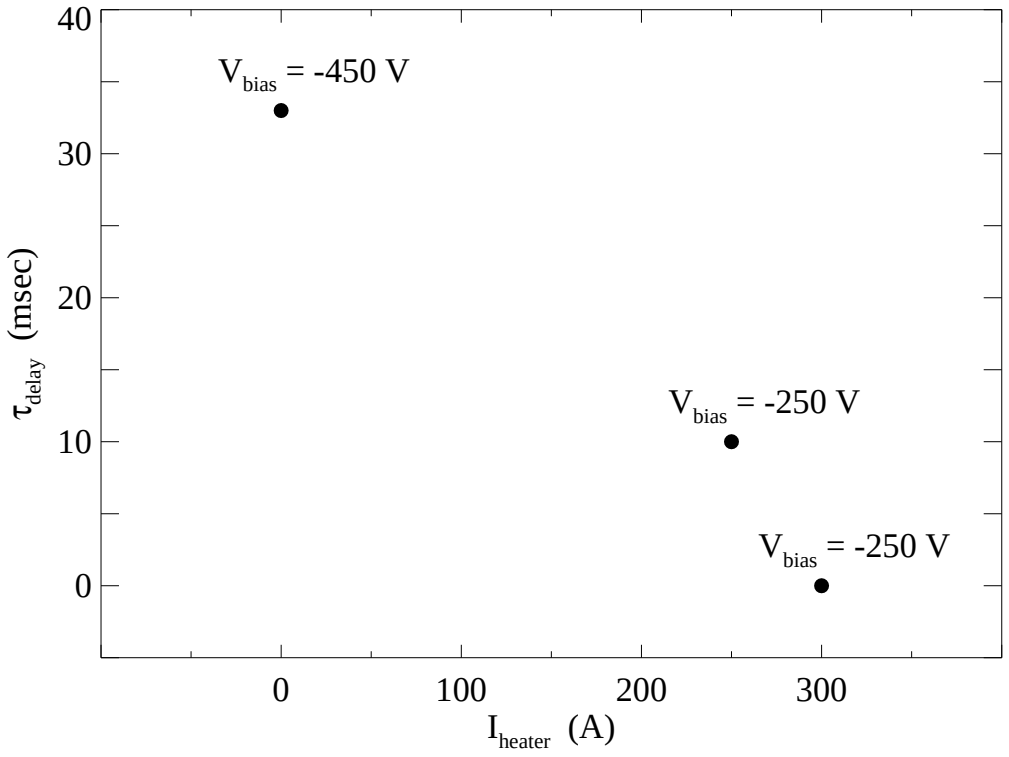

Figure 7.6: Time delay to reach H-mode after biasing begins.

probe array (Fig. 7.7(a)) indicates that right after the negative bias is applied, the resulting electric field around where the limiter resides increases by a factor of 3 compared to that before biasing (Fig. 7.7(b)).

The radial profile of the floating potential near the cathode from 4 different shots with different locations of the cathode is depicted in Fig. 7.8. For this series of shots, $V_{bias} = -220\,V$, $I_{heater} = 320\,A$, and other conditions were held fixed. The dotted line in the figure indicates the potential before the bias voltage was applied to the limiter and the others are potentials in the H-mode state. The abscissa is the distance from the liner and Δt represents the time after the H-mode transition occurs. The comparison between before and after biasing illustrates that the biasing steepens the slopes of the potential. Moreover, this increased radial electric field is found to be extended inward to approximately 2 or 3 cm from the lower boundary of the cathode as well as outside of it in the SOL region. The usual transport phenomena may not explain this inward extension of E-layer, and two possible explanations exist. One possibility is transport along stochastic magnetic field, i.e., the emitted electrons are not localized due to the field stochasticity so that electrons spread out radially around the cathode. The other possibility is the inward convective motion of emitted high energy electrons.

Figure 7.9 was obtained from 4 shots (Fig. 7.8) in the H-mode regime with different locations of the cathode. Even though the absolute value of the potentials are slightly different from each other, the slopes of the 4 potential traces are more or less same.

(c) Cathode limiter bias voltage scan

In order to see how sensitively the radial electric field changes at the edge of the plasma due to the bias voltage, several shots were taken with different voltages while the heater current of $300\,A$ and other conditions remained fixed (Fig. 7.10). In this experiment, $-150\,V$ was the lowest bias voltage in which a transition was obtained. Due to the charging-up of the plasma by electrons emitted from the cathode limiter, a $100\,V$ difference in the bias voltage change produces an increase of the electric field by a factor of 2.

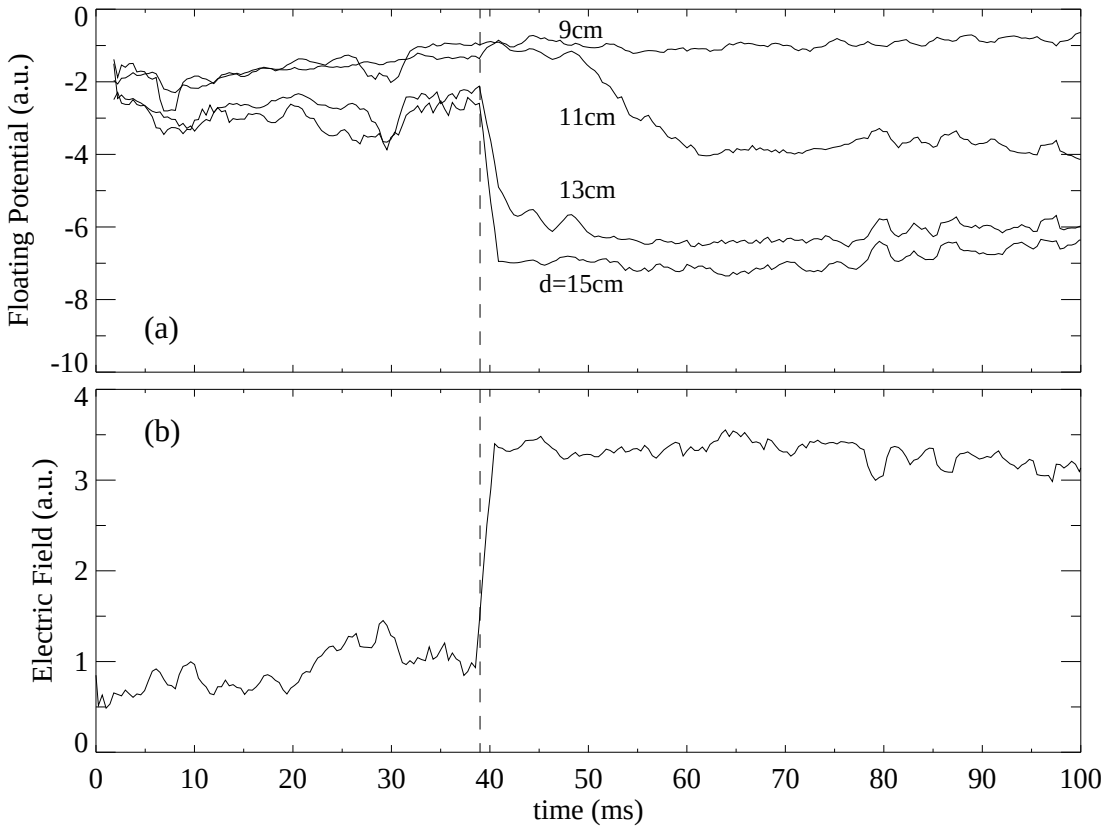

Figure 7.7: Time history of (a) floating potentials at 4 locations and (b) the corresponding electric field from 2 probe tips. The tips are located at 9, 11, 13, 15 cm from the copper liner, respectively. As soon as the bias voltage is applied at $t = 39\,msec$, the electric field between probe tips at $d = 15\,cm$ and $d = 9\,cm$ increases by 3 times compared to that before biasing. The cathode is located at 15 cm from the liner and $V_{bias} = -250\,V$, $I_{heater} = 300\,A$.

7.4 Summary

The utilization of a limiter which is capable of injecting thermionic electrons may provide an efficient means of inducing H-modes in plasmas. In experiments on CCT, when the limiter was heated to reach a certain temperature ($\sim 1200\,℃$) and biased by $-150\,V$ to $-260\,V$, the ohmic plasma transitioned to the H-mode regime, showing line-integrated density rise, impurity light intensity drop, lower loop voltage, and a decrease of injection current, implying the drop of electron transport to the wall. The emissive capability of the limiter also lowered the impurity influx from the wall, since the H-mode could be induced at a lower bias voltage. According to the limiter position scan, positioning of the plasma becomes more crucial as the cathode is moved closer to the wall since the plasma can easily detach from the cathode and reattach to the wall. When the limiter heater current was not sufficiently high, a higher bias voltage was required to induce H-mode, and a time delay to get into H-mode was observed. The maximum electric field after an H-mode transition is a linear function of the limiter bias voltage in the operating regime of this experiment ($-150\,V$ to $-260\,V$), but it is unrelated to the limiter heater current ($250\,A$ to $300\,A$).

The radial profile of the plasma potential shows that the electric field at the edge of the plasma increases by a factor of 3 after the biasing of the electron-emitting limiter began. This increased electric field exists $2-3\,cm$ beyond the limiter bottom edge inside the plasma, and may be attributed to the inward penetration of emitted electrons by an anomalous diffusion process.

An emissive limiter has the advantages that it is simple and reliable, inexpensive to operate, and the heated cathode may be able to reduce the impurity problem compared to using a cold limiter. The results shown in this experiment suggest that the performance of the limiter or divertor bias experiments can be significantly improved by simply adding emissive capability.

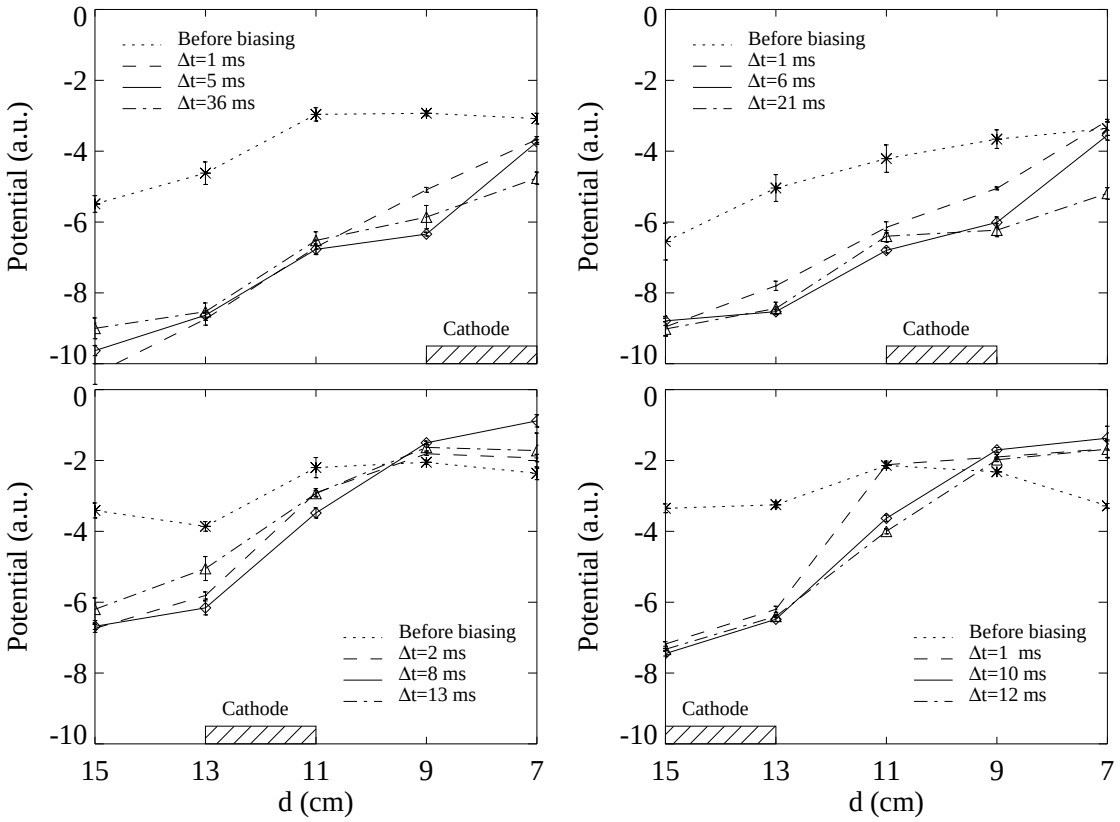

Figure 7.8: Radial profile of the floating potential inside and outside the cathode from four different shots. Δt indicates the time after the H-mode transition and the abscissa is the distance measured from the copper liner. $V_{bias} = -220\,V$ and $I_{heater} = 320\,A$ for these shots. Potential in the H-mode increased noticeably compared to that before cathode bias was applied.

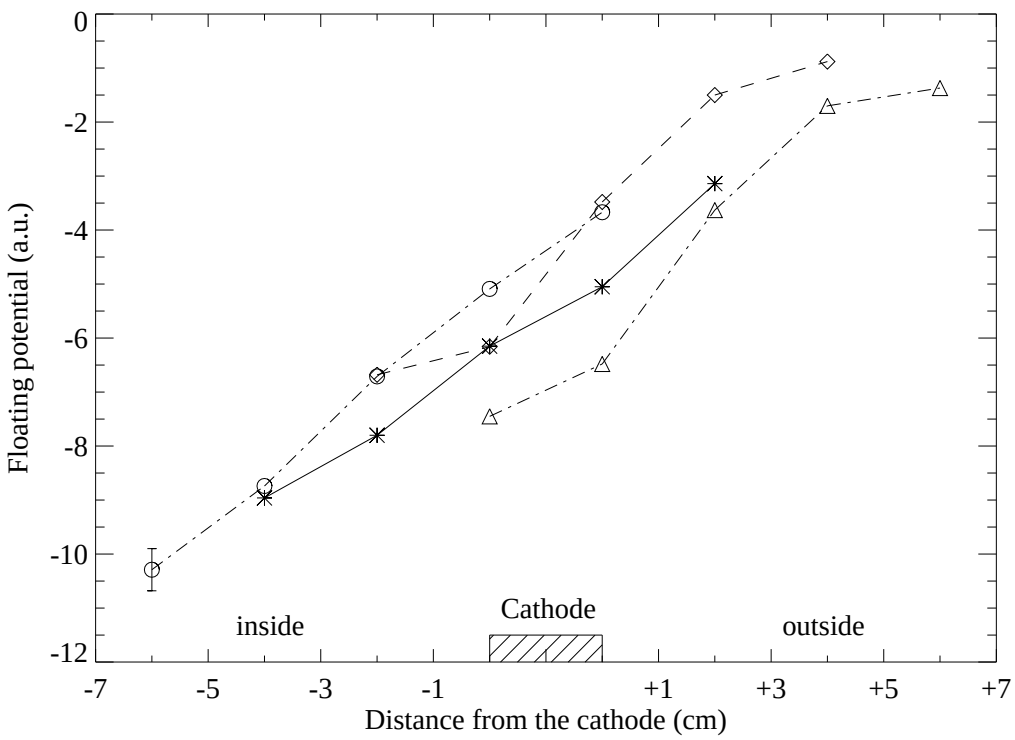

Figure 7.9: Radial profile of the typical floating potential in the H-mode inside and outside cathode from four different shots. In the plot, inside means plasma region and outside means scrape-off-layer region. $V_{bias} = -220\,V$ and $I_{heater} = 320\,A$ for these shots.

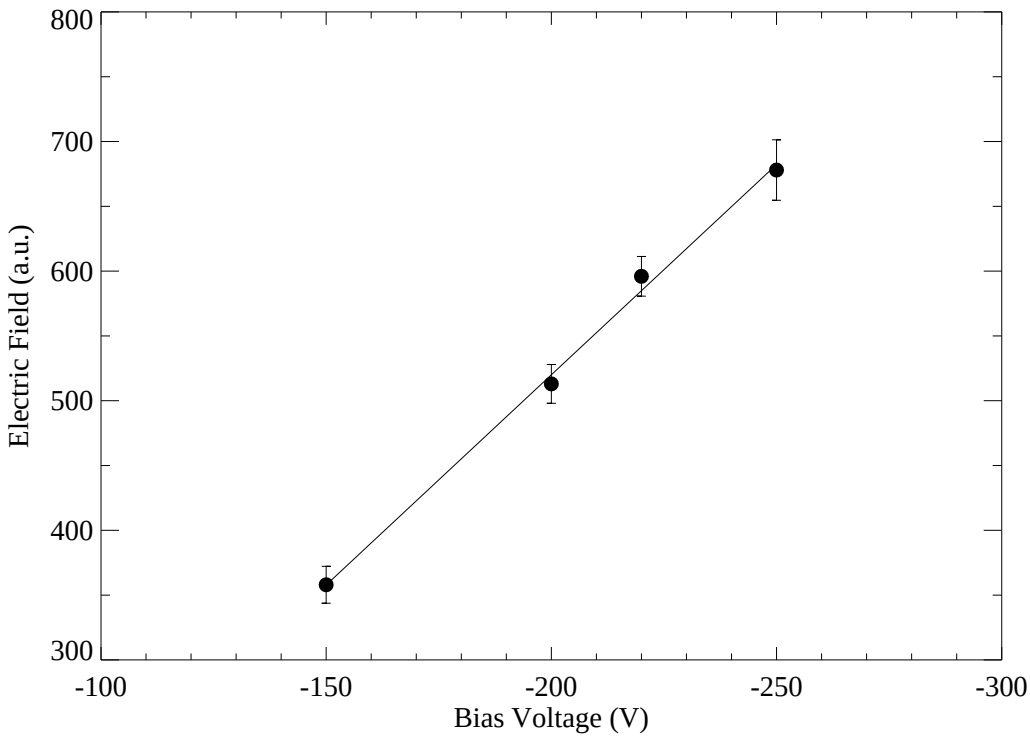

Figure 7.10: Maximum electric field as a function of limiter bias voltage after H-mode transition. The cathode limiter was placed at 15 cm inside the liner and heated with $I_{heater} = 300\,A$.

Chapter 8

Summary of the Thesis and Future Work

8.1 Summary of the Thesis

For the successful operation of advanced and next generation tokamaks, it is important to have a tool for plasma transport modification. The development of a versatile knob to control plasma transport could help optimize tokamak plasma performance, eventually making tokamak reactors more efficient and economical. Since the projection for the H-mode power threshold is unacceptably high for future size devices (eg., $> 100\,MW$ for ITER), and it is necessary to reduce the required input power. Recently, it has been discovered that the radial electric field plays an important role in H-mode barrier formation [Wagner *et al.*, 1984; Tynan *et al.*, 1994], and thus, in the transition into improved confinement regimes, i.e., the L-H and H-VH mode [Burrell *et al.*, 1994; Kim *et al.*, 1994b; Kim *et al.*, 1994a]. Motivated by these observations, efforts have been made in this thesis to devise two novel techniques to create the needed radial electric field by external means, utilizing injection of hot electrons.

8.1.1 Electron Ripple Injection

This concept is for inducing a radial electric field by a non-intrusive way. The advantages are that the physics involved is relatively simple, and that the method is easily controllable and therefore applicable to larger size devices. Electron cyclotron

resonance heating and the externally provided magnetic ripple field are utilized for particle trapping. The trapped electrons drift towards the plasma center by ∇B and curvature drifts. These electrons are eventually detrapped at the inner flux surfaces resulting in charging up the plasma negatively.

A computer program was developed to study the complex 3-dimensional magnetic field topology in the presence of a local ripple field. The code was also useful in the design of ripple coils.

As ECRH is applied, the temperature anisotropy of epithermal electrons was calculated analytically by solving the perpendicular and parallel energy moments of the Fokker-Planck equation, including heat transport due to the electron ripple injection. A bi-Maxwellian model was used for the warm electron distribution function and the full form of the Coulomb collision operator was retained. Results show that $T_\perp/T_\parallel$ can be quite large (≤ 15) with a moderate input wave power and a reasonable ripple strength.

The behavior of energetic electrons and the generation of a radial electric field in the presence of externally provided ripple fields were investigated using a Monte-Carlo guiding-center electron orbit code. A series of simulations for the CDX-U parameters predicts that the generation of a fairly large radial electric field ($\simeq -3.0\,kV/m$) is possible by injecting electrons equal to about 1.2 % of the total population in number in the region of $r/a = (0.9{-}1.0)$. The predicted injected radial current and ECRH power are $23\,A$ and $23\,kW$, respectively. In order to extrapolate this technique to larger size devices, a simulation has also been performed using ITER parameters. For ITER simulations, it is assumed that the ripple coils are located at $R = R_0$ and $Z = 1\,m$ above the edge of the plasma and have a coil current of $0.8\,MA$. The energetic electrons are launched with an energy of $80\,keV$ at $R = R_0$ and $Z = 0.2\,m$ below the edge of the plasma where the ripple strength is 0.73 %. In order to generate approximately $-260\,kV/m$ of electric fields, the total injected radial current was calculated to be $120\,A$ and the time needed is $11.9\,msec$. This would mean approximately $10\,MW$ of ECRH power (which is 10 % of the required H-mode threshold power) is required to induce an E_r-bifurcation. This power level is relatively modest for ITER. For this case, a total of 2.0×10^{17} electrons are needed, which is a negligible portion of ITER edge electrons. This prediction is an encouraging result suggesting that the ERI technique could be

a promising alternative for generating a strong radial electric field and, thus, for possibly controlling tokamak plasma transport.

In parallel to the modeling work, a few different sets of preliminary experiments have been performed on CDX-U. First, the existence of electron drifts was confirmed with the observed behavior consistent with expectations. Second, the magnetic field topology was investigated in a simple magnetic field geometry with toroidal and ripple fields. The results are in good agreement with the numerical calculation. Finally, the measurement of the warm electron temperature anisotropy under ECH and ripple trapping has been accomplished. The experimentally determined value of the temperature anisotropy is in reasonably good agreement with the analytically predicted value.

8.1.2 Emissive Limiter Biasing

One other approach has been taken in utilizing electron injection for tokamak plasma confinement improvement: experiments in ohmic tokamak discharges with a LaB_6 biased limiter. This experiment is unique among limiter biasing experiments in that the limiter is capable of emitting energetic electrons.

To study the effect of the emitted electrons, the limiter position, bias voltage, and plasma position were varied. The results show that the plasma position with respect to the emissive limiter plays an important role in obtaining H-mode plasmas. The emissive limiter must be located close to the last closed flux surface in order to charge up the plasma. As the limiter was moved closer to the wall, the position of the plasma became more critical since the plasma could easily detach from the limiter and reattach to the wall, resulting in termination of the H-mode. The emissive capability appeared to be important for operating at lower bias voltage and reducing impurity levels in the plasma. With a heated limiter, transition to H-mode was observed for $V_{bias} \leq -150\,V$ and $I_{inj} \geq 30\,A$. At a lower limiter heater current, a higher bias voltage was required for the transition. Moreover, with a lower limiter heater current, the time delay for inducing H-mode became longer, which could be attributed to the required time for the self-heating of the limiter to reach the emissive temperature. With L-mode plasmas, the injection current flowing out of the limiter was generally higher than $100\,A$ and it was approximately $30\,A$ for the H-mode case.

In order to develop concepts for controlling edge plasma transport, we developed and tested two novel concepts by utilizing injection of hot electrons in this thesis research. One technique is to bias an edge plasma utilizing a limiter which has the capability of emitting hot electrons. Experimental results show that the capacity for emission can significantly improve the performance of limiter biasing for inducing H-mode transition. For large size, reactor-relevant, high density and temperature devices, however, a non-intrusive way of modifying plasma edge transport is more desirable since any material contact on the plasmas will cause many problems. In this regard, the electron ripple injection technique may provide a good and potential answer for this question. Both modeling and preliminary experiments on CDX-U support this concept, as discussed in detail.

8.2 Suggestions for Future Work

As discussed at length in previous chapters, the electron ripple injection provides a promising technique to generate a radial electric field in a non-intrusive way. In order for it to be practical and successful, several important issues should be resolved:

(1) Collisions: it was assumed that Coulomb collisions were negligible in the model that determined the electron temperature anisotropy from the experimental data. This assumption is valid because the collisional mean free path is much larger than the system scale length in the experiments on CDX-U. However, a plasma can be quite collisional especially at the plasma edge in some tokamaks. In these cases, collisions will reduce ripple trapping via pitch angle scattering so that the ripple effect can become inefficient. More study on this issue is necessary.
(2) Direct measurement of electron energy distribution function: the temperature anisotropy was determined from density measurements in both perturbed and unperturbed regions, as the temperature anisotropy is related to the ripple trapping. The temperature anisotropy obtained by a direct measurement of the electron energy distribution function is one way to check our results.
(3) Effect of structure of ripple coils: even though all the modeling has been performed for both *TypeI* and *TypeII* ripple coils, the experimental determination of the temperature anisotropy was performed only with *TypeII* ripple coils. This is

because the ripple effect is expected to be global in the vertical direction (there is a larger volume of ripple region) with *TypeII* ripple coils, which makes experiments better controlled. The physics is expected to be same with ripple coils of *TypeI*, but experiments to verify this would be instructive.

(4) Velocity-space instabilities in the ripple region: Okuda *et al.* [Okuda, 1995] performed the stability analysis for an injected electron population with a predominantly perpendicular energy. He assumed a Maxwellian background and a warm distribution function of the form $f_w = n_w\,\delta(v_\perp - v_0)/v_\perp\, f_M(v_\parallel)$. According to the simulation results, instabilities were observed for $\omega_{pe}/\Omega_e \geq 4$, where ω_{pe} includes both background and warm electron contributions. For tokamaks, ω_{pe}/Ω_e is of order unity at the plasma center, and is usually much less than unity at the edge, which suggests that no instability should be expected.

(5) Possible perturbation of magnetic flux surfaces and the bulk plasma transport properties.

(6) Alpha particle loss due to magnetic field ripple: recent work [Boivin *et al.*, 1993; Redi *et al.*, 1995; Darrow, 1995] reveals that $\leq 15\,\%$ of alpha particle energy is lost globally due to first orbit and collisional stochastic ripple diffusion caused by $2\,\%$ of TFTR toroidal field ripple. In reactor-relevant devices such as ITER in general, the loss of this charged fusion product can be an important issue. According to our simulation, however, the ripple strength required for bifurcation is low ($0.73\,\%$), and the ripple region is spatially localized. As Fig. 4.13 shows, the radial region where E_r is generated is about $30\,cm$ from the plasma edge. In this region, an alpha particle may be already lost due to its large Larmor radius and banana width. Therefore, the additional loss of alpha particles caused by a ripple injector may not be significant.

(7) Application to larger tokamaks: since both modeling and preliminary experiments done on CDX-U give encouraging results, the electron ripple injection experiment on tokamak plasmas represents worthwhile experiments for the near future.

Bibliography

ASDEX Team (1989). The H-mode of ASDEX. *Nucl. Fusion* **29**, 1959.

Askinazi, L. G., Golant, V. E., and Lebedev, S. V. (1992). Radial Current in a Tokamak Caused by a Biased Electrode. *Nucl. Fusion* **32**, 271.

Biglari, H., Diamond, P. H., and Terry, P. W. (1990). Influence of Sheared Poloidal Rotation Edge Turbulence. *Phys. Fluids B* **2**, 1.

Boivin, R. L., Zweben, S. J., and White, R. B. (1993). Study of Stochastic Toroidal Field Ripple Losses of Charged Fusion Products at the Midplane of TFTR. *Nucl. Fusion* **33**, 449.

Braginskii, S. I. (1966). *Review of Plasma Physics Vol.1 (ed. M.A. Leontovich)*. Consultants Bureau, New York.

Burrell, K. H., Allen, S. L., Bramson, G., *et al.* (1989). Confinement Physics of H-mode Discharges in DIII-D. In *Plasma Phys. Control. Fusion*, volume 31, page 1649, International Atomic Energy Agency, Vienna.

Burrell, K. H., Doyle, E. J., Gohil, P., *et al.* (1994). Role of the Radial Electric Field in the Transition from L (low) mode to H (high) mode to VH (very high) mode in the DIII-D tokamak. *Phys. Plasmas* **1**, 1536.

Burrell, K. H., Ejima, S., Schissel, D. P., *et al.* (1987). Observation of an Improved Energy-Confinement Regime in Neutral-Beam-Heated Divertor Discharges in the DIII-D Tokamak. *Phys. Rev. Lett.* **59**, 1432.

Bush, C. E., Bretz, N., Budny, R., *et al.* (1994). Supershot to Limiter H-mode Transitions in Deuterium Plasmas in TFTR. In *Plasma Phys. Control. Fusion*, volume 36, page A153, International Atomic Energy Agency, Vienna.

Bush, C. E., Bretz, N. L., Frederickson, E. D., *et al.* (1991). Limiter H-mode Experiments on TFTR. In *Plasma Physics and Controlled Nuclear Fu-*

sion Research, 1990, volume 1, page 309, International Atomic Energy Agency, Vienna.

Bush, C. E., Goldston, R. J., Scott, S. D., *et al.* (1990). Peaked Density Profiles in Circular-Limiter H Modes on the TFTR Tokamak. *Phys. Rev. Lett.* **65**, 424.

Carolan, P. G., Fielding, S. J., Gerasimov, S., *et al.* (1994). Characteristics of Ohmic H-modes in COMPASS-D. In *Plasma Phys. Control. Fusion*, volume 36, page A111, International Atomic Energy Agency, Vienna.

Chang, C. S. (1993). Neoclassical Viscosity of a Tokamak Plasma with Large Mass Flow. *Phys. Fluids B* **5**, 4360.

Chang, C. S. and Colestock, P. (1990). Anisotropic Distribution Function of Minority Tail Ions Generated by Strong Ion-cyclotron Resonance Heating. *Phys. Fluids B* **2**, 310.

Chang, C. S., Lee, J.-Y., and Weitzner, H. (1991). Thoery of Energetic Ion Transport Induced by Waves of Ion Cyclotron Range of Frequencies in a Tokamak Plasma. *Phys. Fluids B* **3**, 3429.

Choe, W., Chang, C. S., and Ono, M. (1995a). Temperature Anisotropy in a Cyclotron Resonance Heated Tokamak Plasma and the Generation of Poloidal Electric Field. *Phys. Plasmas* **2**, 2044.

Choe, W., Ono, M., and Chang, C. S. (1995b). Conceptual Study of Electron Ripple Injection for Tokamak Transport Control. Technical Report PPPL-3138, Princeton Plasma Physics Laboratory; submitted to *Nucl. Fusion*.

Choe, W., Ono, M., and Chang, C. S. (1995c). Electron Ripple Injection Concept for Tokamak Transport Control. In *Proceedings of the Eleventh Topical Conference on Radio Frequency Power in Plasmas, Palm Springs.* to be published.

Choe, W., Ono, M., Darrow, D. S., *et al.* (1993a). Emissive Limiter Bias Experiments for Improved Confinement of Tokamaks. In *Proc. IAEA Technical Committee Meeting on Tokamak Plasma Biasing, Montreal, 1992*, page 95, International Atomic Energy Agency, Vienna.

Choe, W., Ono, M., and Hwang, Y. S. (1993b). Electron Ripple Injection

Concept for Transport Control. In *Proc. IAEA Technical Committee Meeting on Tokamak Plasma Biasing, Montreal, 1992*, page 297, International Atomic Energy Agency, Vienna.

Coda, S. and Porkolab, M. (1995). Edge Fluctuation Measurements by Phase Contrast Imaging on DIII-D. *Rev. Sci. Instrum.* **66**, 454.

Conn, R. W., Goebel, D. M., Leung, W. K., *et al.* (1987). ALT-I Pump Limiter Behavior and Edge Plasma Flows During Biasing and ICRF Heating in the TEXTOR Tokamak. In *Plasma Physics and Controlled Nuclear Fusion Research, 1986*, volume 1, page 249, International Atomic Energy Agency, Vienna.

Couture, P., Boileau, A., Décoste, R., *et al.* (1992). Biasing of Closed Double Null Poloidal Divertor Plates on TdeV. *Phys. Lett. A* **163**, 204.

Couture, P., Terreault, B., Bourque, G., *et al.* (1990). Reduction of Plasma-Wall Interaction by Plasma Biasing. *J. Nucl., Mat.* **176-177**, 825.

Darrow, D. S. (1988). *DC Helicity Injection Studies on the Current Drive Experiment*. PhD thesis, Princeton University.

Darrow, D. S. (1995). private communication.

Darrow, D. S., Ono, M., Forest, C. B., *et al.* (1990). Properties of dc Helicity Injected Tokamak Plasmas. *Phys. Fluids B* **2**, 1415.

DoE, U. (1992). FEAC Report on the U.S. Program of Fusion Energy Research. Technical report, U.S. Department of Energy.

Equipe TFR (1979). Low-Z_{eff} Plasma Confinement in TFR 600 Tokamak. In *Plasma Physics and Controlled Nuclear Fusion Research, 1978*, volume 1, page 135, International Atomic Energy Agency, Vienna.

Erckmann, V., Brakel, R., Burhenn, R., *et al.* (1993a). H-mode Like Transitions in the W7-AS Stellarator with High Power 140 GHz ECRH. In *Plasma Physics and Controlled Nuclear Fusion Research, 1992*, volume 2, page 469, International Atomic Energy Agency, Vienna.

Erckmann, V., Wagner, F., Baldzuhn, J., *et al.* (1993b). H Mode of the W7-AS Stellarator. *Phys. Rev. Lett.* **70**, 2086.

Field, A. R., Fussmann, G., and Hoffmann, J. V. (1992). Measurement of the Radial Electric Field in the ASDEX Tokamak. *Nucl. Fusion* **32**, 1191.

Forest, C. B. (1992). *Pressure Driven Currents in the CDX-U Trapped Particle Configuration*. PhD thesis, Princeton University.

Forest, C. B., Greene, G., and Ono, M. (1990). CDX-U two-dimensional scanning microwave system. *Rev. Sci. Instrum.* **61**, 2888.

Forest, C. B., Hwang, Y. S., Ono, M., *et al.* (1992). Internally Generated Currents in a Small-Aspect-Ratio Tokamak Geometry. *Phys. Rev. Lett.* **68**, 3559.

Fulkerson, W., Judkins, R. R., and Sanghvi, M. K. (1990). Energy from Fossile Fuels. *Sci. Am.* **September**, 129.

Gaudreau, M., Gondhelekar, A., Hughes, M. H., *et al.* (1977). High-Density Discharges in the Alcator Tokamak. *Phys. Rev. Lett.* **39**, 1266.

Goldston, R. J., Jassby, D. L., Towner, H. H., *et al.* (1977). Magnetics Design for Ripple-assisted Beam Injection into the ISX-B and TFTR Tokamaks. In *Proc.* 7th *Symposium on Engineering Problems of Fusion Research*, volume v.2, page 1333.

Greenfield, C. M., Jackson, G. L., Burrell, K. H., *et al.* (1992). VH-mode Discharges in the DIII-D Tokamak. In *Proc.* 19th *Eur. Conf. on Contr. Fusion and Plas. Heating*, volume v.16, page 11.

Groebner, R. J., Burrell, K. H., Gohil, P., and Seraydarian, R. P. (1990a). Spectroscopic Study of Edge Poloidal Rotation and Radial Electric Fields in the DIII-D Tokamak. *Rev. Sci. Instrum.* **61**, 2920.

Groebner, R. J., Burrell, K. H., and Seraydarian, R. P. (1990b). Role of Edge Electric Field and Poloidal Rotation in the L-H Transition. *Phys. Rev. Lett.* **64**, 3015.

Groebner, R. J., Peebles, W. A., Burrell, K. H., *et al.* (1991). Role of the Edge Electric Field and Microturbulence in the L-H Transition. In *Plasma Physics and Controlled Nuclear Fusion Research, 1990*, volume 1, page 453, International Atomic Energy Agency, Vienna.

Hahm, T. S. and Burrell, K. H. (1995). Flow Shear Induced Fluctuation Suppression in Finite Aspect Ratio Shaped Tokamak Plasma. *Phys. Plasmas* **2**, 1648.

Hawkes, N. (1993). Electric Field Measurements during the H-mode in JET. In *Proc.* 20th *Eur. Conf. on Contr. Fusion and Plas. Heating*, volume v.17C, page 3.

Hillis, D. L., Hogan, J. T., Wade, M. R., *et al.* (1993). Helium Transport Studies in Enhanced Confinement Regimes on the DIII-D Tokamak. In *Plasma Physics and Controlled Nuclear Fusion Research, 1992*, volume 1, page 577.

Hillis, D. L., Wade, M. R., Hogan, J. T., *et al.* (1994). Helium Transport and Exhaust Studies of H-mode Discharges in the DIII-D Tokamak. In *Plasma Phys. Control. Fusion*, volume 36, page A171, International Atomic Energy Agency, Vienna.

Hinton, F. L. (1983). *Basic Plasma Physics I (ed. A.A. Galeev).* North Holland, Amsterdam.

Holzhauer, E. and Dodel, G. (1990). Collective Laser Light Scattering from Electron Density Fluctuations in Fusion Research Plasmas. *Rev. Sci. Instrum.* **61**, 2817.

Holzhauer, E., Dodel, G., Endler, M., *et al.* (1994). The H-mode in the ASDEX Tokamak. In *Plasma Phys. Control. Fusion*, volume 36, page A3, International Atomic Energy Agency, Vienna.

Hoshino, K., Yamamoto, T., Kawashima, H., *et al.* (1989). H Mode Observed in the JFT-2M Tokamak with Edge Heating by Electron Cyclotron Waves. *Phys. Rev. Lett.* **63**, 770.

Hoshino, K., Yamamoto, T., Suzuki, N., *et al.* (1988). Transition from the L-mode to the H-mode by Electron cyclotron Heating of a Tokamak Edge Plasma. *Nucl. Fusion* **28**, 301.

Hwang, Y.-S. (1993). *Studies of Non-inductive Current Drive in the CDX-U Tokamak.* PhD thesis, Princeton University.

Hwang, Y. S. *et al.* (1995). Exploration of Low-aspect-ratio Tokamak Regimes in CDX-U and TS-3 Devices. In *Plasma Physics and Controlled Nuclear Fusion Research, 1994*. IAEA-CN-60/A5-II-6, to be published.

Ida, K., Hidekuma, S., Kojima, M., *et al.* (1992). Edge Poloidal Rotation Profiles of the H-mode Plasmas in the JFT-2M Tokamak. *Phys. Fluids B* **4**,

2552.

Ida, K., Hidekuma, S., Miura, Y., *et al.* (1990). Edge Electric-Field Profiles of H-Mode Plasmas in the JFT-2M Tokamak. *Phys. Rev. Lett.* **65**, 1364.

Ida, K., Kawahata, K., Toi, K., *et al.* (1991). Observation of Toroidal Plasma Rotation Driven by the Electric Field Induced by Loss of Ions. *Nucl. Fusion* **31**, 943.

Janev, R. K., Langer, W. D., Evans, K., *et al.* (1987). *Elementary Processes in Hydrogen-Helium Plasmas.* Springer-Verlag, Berlin.

JET Team (1993). JET Progress Report 1993. Technical report, JET Joint Undertaking.

Jones, T. J. (1995). *Low-Aspect-Ratio Tokamak Start-up and Operational Current Limits in CDX-U.* PhD thesis, Princeton University.

Kaufmann, M., Bosch, H.-S., Field, A., *et al.* (1993). Edge Physics and H-mode Studies in ASDEX Upgrade. In *Plasma Phys. Control. Fusion*, volume 35, page B205, International Atomic Energy Agency, Vienna.

Kaye, S. *et al.* (1995). Projection of ITER Performance Using the Multi-Machine-L and H-mode Databases. In *Plasma Physics and Controlled Nuclear Fusion Research, 1994.* IAEA-CN-60/E-P-3, to be published.

Kaye, S. M., Bell, M. G., Bol, K., *et al.* (1984). Attainment of High Confinement in Neutral Beam Heated Divertor Discharges in the PDX Tokamak. *J. Nucl., Mat.* **121**, 115.

Keilhacker, M., v. Gierke, G., Müller, E. R., *et al.* (1986). Confinement in ASDEX with Neutral Beam and RF Heating. In *Plasma Phys. Control. Fusion*, volume 28, page 29, International Atomic Energy Agency, Vienna.

Kennel, C. F. and Engelmann, F. (1966). Velocity Space Diffusion from Weak Plasma Turbulence in a Magnetic Field. *Phys. Fluids* **9**, 2377.

Kikuchi, M., Shirai, H., Takizuka, T., *et al.* (1993). H- and L-mode Confinement in JT-60U. In *Plasma Physics and Controlled Nuclear Fusion Research, 1992*, volume 1, page 189, International Atomic Energy Agency, Vienna.

Kim, J., Burrell, K. H., Gohil, P., *et al.* (1994a). Fuel Ion Rotation Measurement and Its Implications on H-mode Theories. In *Plasma Phys. Control.*

Fusion, volume 36, page A183, International Atomic Energy Agency, Vienna.

Kim, J., Burrell, K. H., Gohil, P., *et al.* (1994b). Rotation Characteristics of Main Ions and Impurity Ions in H-Mode Tokamak Plasma. *Phys. Rev. Lett.* **72**, 2199.

Kim, J., Burrell, K. H., Gohil, P., *et al.* (1994c). Rotation Characterstics of Main Ions and Impurity Ions in H-mode Tokamak Plasma. *Phys. Rev. Lett.* **72**, 2199.

Klüber, O. and Murmann, H. (1982). Energy Confinement in the Tokamak Devices Pulsator and ASDEX. Technical Report IPP III/72, Pax-Planck-Institute fur Plasmaphysik.

Koide, Y., Kikuchi, M., Mori, M., *et al.* (1994). Internal Transport Barrier on q=3 Surface and Poloidal Plasma Spin Up in JT-60U High-β_p Discharges. *Phys. Rev. Lett.* **72**, 3662.

Krall, N. A. and Trivelpiece, A. W. (1973). *Principles of Plasma Physics.* McGraw-Hill, New York.

LaHaye, R. J., Groebner, R. J., Hyatt, A. W., *et al.* (1993). Effect of magnetic braking of the plasma rotation on the H-mode radial electric field and energy confinement in the DIII-D tokamak. *Nucl. Fusion* **33**, 349.

Lazarus, E. A., Lao, L. L., Taylor, T. H., *et al.* (1992). An Optimization of Beta in the DIII-D Tokamak. *Phys. Fluids B* **4**, 3644.

LeHacka, T., Doyle, E. J., Philipona, R., *et al.* (1989). Results from the DIII-D Milimeter-Wave Reflectometer. In *Proc.* 16th *Eur. Conf. on Contr. Fusion and Plas. Heating*, volume v.13B, page 123.

Lohr, J., Burrell, K. H., Coda, S., *et al.* (1993). Enhanced Confinement Regimes and Control Technology in the DIII-D Tokamak. Technical report, General Atomics.

Lohr, J., Stallard, B. W., Prater, R., *et al.* (1988). Observation of H-mode Confinement in the DIII-D Tokamak with Electron Cyclotron Heating. *Phys. Rev. Lett.* **60**, 2630.

Longmire, C. L. (1963). *Elementary Plasma Physics.* Interscience Publishers, New York.

Mahdavi, M. A., Schaffer, M., Anderson, P., *et al.* (1991). Divertor Baffling and Biasing Experiments on DIII-D. In *Plasma Physics and Controlled Nuclear Fusion Research, 1990*, volume 1, page 335, International Atomic Energy Agency, Vienna.

Manso, M. E., Wagner, F., Matias, J., *et al.* (1991). H-mode Studies with Microwave Reflectometry on ASDEX. In *Proc.* 18th *Eur. Conf. on Contr. Fusion and Plas. Heating*, volume v.15C, page 393.

Matsumoto, H., Funahashi, A., Hasegawa, M., *et al.* (1987a). Studies of H-mode in the Limiter Discharges on JFT-2M Tokamak. In *Proc.* 14th *Eur. Conf. on Contr. Fusion and Plas. Heating*, volume v.11D, page 5.

Matsumoto, H., Ogawa, T., Tamai, H., *et al.* (1987b). H-mode Phenomena during ICRF Heating on JFT-2M. *Nucl. Fusion* **27**, 1181.

Miura, Y., Aikawa, H., Hoshino, K., *et al.* (1991). Studies of Improved Confinement on JFT-2M. In *Plasma Physics and Controlled Nuclear Fusion Research, 1990*, volume 1, page 325, International Atomic Energy Agency, Vienna.

Murakami, M., Neilson, G. H., Howe, H. C., *et al.* (1979). Plasma Confinement Studies in the ISX-A Tokamak. *Phys. Rev. Lett.* **42**, 655.

Nieuwenhove, R. V., Oost, G. V., Weynants, R. R., *et al.* (1991). Novel Features of H-mode Plasmas Induced by Edge Polarization in TEXTOR. In *Proc.* 18th *Eur. Conf. on Contr. Fusion and Plas. Heating*, volume v.15C, page 405.

Odajima, K., Funahashi, A., Hoshino, K., *et al.* (1987). Confinement Studies of Additionally Heated Plasma in the JFT-2M Tokamak. In *Plasma Physics and Controlled Nuclear Fusion Research, 1986*, volume 1, page 151, International Atomic Energy Agency, Vienna.

Okuda, H. (1995). private communication.

Ono, M., Bell, R., Bernabei, S., *et al.* (1995a). Formation of core transport barrier and CH-Mode by ion Bernstein wave heating in PBX-M. Technical Report PPPL-3042, Princeton Plasma Physics Laboratory.

Ono, M., Darrow, D. S., Greene, G. J., *et al.* (1989). DC Helicity Driven Tokamak. In *Plasma Physics and Controlled Nuclear Fusion Research, 1988*, volume 3, page 479.

Ono, M., Forest, C. B., Hwang, Y. S., *et al.* (1993). Novel Current Drive Experiments on the CDX-U, HIT and DIII-D Tokamaks. In *Plasma Physics and Controlled Nuclear Fusion Research, 1992*, volume 1, page 693.

Ono, M., Furth, H., Forest, C. B., *et al.* (1990). Non-intrusive Methods for Producing Radial Electric Fields in Tokamaks. In *US/Japan Workshop on Edge Plasma Modification in Fusion Plasmas, Nagoya, Japan.*

Ono, M., Greene, G. J., Darrow, D., *et al.* (1987). Steady-state Tokamak Discharge via dc Helicity Injection. *Phys. Rev. Lett.* **59**, 2165.

Ono, M., LeBlanc, B., Munsat, T., *et al.* (1995b). Core Transport Modification by Application of Ion Bernstein Wave Power. *submitted to Physical Review Letter* .

Osborne, T. H., Brooks, N. H., Burrell, K. H., *et al.* (1990). Observation of the H-mode in Ohmically Heated Divertor Discharges on DIII-D. *Nucl. Fusion* **30**, 2023.

Perkins, F., Barabaschi, P., Bosia, G., *et al.* (1995). ITER Physics Basis. In *Plasma Physics and Controlled Nuclear Fusion Research, 1994*. IAEA-CN-60/E-1-I-3, to be published.

Phillips, P. E., Wootton, A. J., Rowan, W. L., *et al.* (1987). Biased Limiter Experiments on TEXT. *J. Nucl., Mat.* **145-147**, 807.

Redi, M. H., Budny, R. V., Darrow, D. S., *et al.* (1995). Modelling TF Ripple Loss of Alpha Particles in TFTR DT Experiments. *Nucl. Fusion* , to be published in December issue.

Rettig, C. L., Peebles, W. A., Burrell, K. H., *et al.* (1993). Edge Turbulence Reduction at the L-H Transition in DIII-D. *Nucl. Fusion* **33**, 643.

Ryter, F., Gruber, O., Büchl, K., *et al.* (1993). Ohmic H-mode and H-mode Power Threshold in ASDEX Upgrade. In *Proc.* 20th *Eur. Conf. on Contr. Fusion and Plas. Heating*, volume v.17C, page 23.

Sakai, Yasaka, Y., and Itatani, R. (1993). High Radial Confinement Mode Induced by dc Limiter Biasing in the HIEI Tandem Mirror. *Phys. Rev. Lett.* **70**, 4071.

Schissel, D. P., Brooks, N., Burrell, K. H., *et al.* (1989). Confinement

Scaling Studies in DIII-D. In *Proc.* 16th *Eur. Conf. on Contr. Fusion and Plas. Heating*, volume v.13B, page 115.

Schissel, D. P., DeBoo, J. C., Rurrell, K. H., *et al.* (1991). H-mode Energy Confinement Scaling from the DIII-D and JET Tokamaks. *Nucl. Fusion* **31**, 73.

Sengoku, S., Funahashi, A., Hasegawa, M., *et al.* (1987). Regime of Improved Confinment in Neutral-Beam-Heated Limiter Discharges of a Tokamak. *Phys. Rev. Lett.* **59**, 450.

Shaing, K. C., Crume, E. C., and Houlberg, W. A. (1990). Bifurcation of Poloidal Rotation and Suppression of Turbulent Fluctuation: A Model for the L-H Transition in Tokamaks. *Phys. Fluids B* **2**, 1492.

Shimada, M., Bell, M. G., Fonck, R. J., *et al.* (1985). Limiter Bias Experiments in PBX Tokamak. *Bull. Amer. Phys. Soc.* **30**, 1439.

Shimada, M., Ozaki, A., Peterson, P., *et al.* (1990). Limiter Bias Experiments in DIII-D. *J. Nucl., Mat.* **176-177**, 821.

Snipes, J. A., Granetz, R. S., Greenwald, M., *et al.* (1994). First Ohmic H Modes in ALCATOR C-MOD. *Nucl. Fusion* **34**, 1039.

Söldner, F. X., Müller, E. R., Wagner, F., *et al.* (1988). Improved Confinement in High-Density Ohmic Discharges in ASDEX. *Phys. Rev. Lett.* **61**, 1105.

Stambaugh, R. D., Wolfe, S. M., Hawryluk, R. J., *et al.* (1990). Enhanced Confinement in Tokamaks. *Phys. Fluids B* **2**, 2941.

Steinmetz, K., Noterdaeme, J.-M., Wagner, F., *et al.* (1987). Observation of a High-Confinement Regime in a Tokamak Plasma with Ion Cyclotron-Resonance Heating. *Phys. Rev. Lett.* **58**, 124.

Stix, T. H. (1975). Fast-wave Heating of a Two-component Plasma. *Nucl. Fusion* **15**, 737.

Strachan, J. D., Bitter, M., Ramsey, A. T., *et al.* (1987). High-Temperature Plasmas in the Tokamak Fusion Test Reactor. *Phys. Rev. Lett.* **58**, 1004.

Stringer, T. E. (1972). Effect of the Magnetic Field Ripple on Diffusion in Tokamaks. *Nucl. Fusion* **12**, 689.

Tanga, A., Bartlett, D. V., Behringer, K., *et al.* (1987). Experimental Studies in JET with Magnetic Separatrix. In *Plasma Physics and Controlled Nuclear Fusion Research, 1986*, volume 1, page 65, International Atomic Energy Agency, Vienna.

Taylor, R. J., Brown, M. L., Fried, B. D., *et al.* (1989). H-mode Behavior Induced by Cross-Field Currents in a Tokamak. *Phys. Rev. Lett.* **63**, 2365.

Taylor, R. J., Conn, R., Fried, B. D., *et al.* (1991). Enhanced Confinement in CCT and PISCES-A in the Presence of Radial Electric Fields. In *Plasma Physics and Controlled Nuclear Fusion Research, 1990*, volume 1, page 463, International Atomic Energy Agency, Vienna.

Toi, K., Adati, K., Akiyama, R., *et al.* (1989). Limiter H-modes in the JIPP T-IIU Tokamak. In *Proc.* 16th *Eur. Conf. on Contr. Fusion and Plas. Heating*, volume v.13B, page 221.

Toi, K., Akiyama, R., Arimoto, H., *et al.* (1994). H-Mode Transition in the CHS Heliotron/Torsatron. In *Plasma Phys. Control. Fusion*, volume 36, page A117, International Atomic Energy Agency, Vienna.

Toi, K., Okamura, S., Iguchi, H., *et al.* (1993). Formation of an H-mode-like Transport Barrier in the CHS Heliotron/Torsatron. In *Plasma Physics and Controlled Nuclear Fusion Research, 1992*, volume 2, page 461, International Atomic Energy Agency, Vienna.

Tsuji, S., Ushigusa, K., Ikeda, Y., *et al.* (1990). Observation of the Limiter H Mode in the JT-60 Tokamak with Lower-Hybrid Current Drive. *Phys. Rev. Lett.* **64**, 1023.

Tubbing, B. J. D., Jacquinot, J. J., Stork, D., *et al.* (1989). H-mode in JET with Ion Cyclotron Resonance Heating Alone. *Nucl. Fusion* **29**, 1953.

Tynan, G. R., Schmitz, L., Blush, L., *et al.* (1994). The Physics of Transport Barrier Formation in the PBX-M H-mode. In *Plasma Phys. Control. Fusion*, volume 36, page A285, International Atomic Energy Agency, Vienna.

Wagner, F. (1994). New Subjects of the H-mode. In *Plasma Phys. Control.*

Fusion, volume 36, page A319, International Atomic Energy Agency, Vienna.

Wagner, F., Baldzuhn, J., Brakel, R., *et al.* (1994). H-mode of W7-AS Stellarator. In *Plasma Phys. Control. Fusion*, volume 36, page A61, International Atomic Energy Agency, Vienna.

Wagner, F., Becker, G., Behringer, K., *et al.* (1982). Regime of Improved Confinement and High Beta in Neutral-Beam-Heated Divertor Discharges of the ASDEX Tokamak. *Phys. Rev. Lett.* **49**, 1408.

Wagner, F., Fussmann, G., Grave, T., *et al.* (1984). Development of an Edge Transport Barrier at the H-Mode Transition of ASDEX. *Phys. Rev. Lett.* **53**, 1453.

Weynants, R. R., Taylor, R. J., Vandenplas, P. E., *et al.* (1990). H-mode Behavior Induced by Edge Polarization in TEXTOR. In *Proc.* 17th *Eur. Conf. on Contr. Fusion and Plas. Heating*, volume v.14B, page 287.

Wolfram, S. (1991). *Mathematica*. Addison-Wesley, Redwood City, Calif.